TECHNISCHE UNIVERSITÄT WIEN
Vienna | Austria

ILSB

Master Thesis:

Quantification of microdamage formation during fatigue testing of individual trabeculae

Julia-Theresa Fischer
Matrikel Nr.: 1026272

carried out and submitted at
Institute of Lightweight Design and Structural Biomechanics (ILSB)
Technical University of Vienna

under the supervision of:
Dipl.-Ing. Martin Frank, BSc
Univ.Prof. Dipl.-Ing. Dr.sc.nat. Philipp J. Thurner

June 19, 2018

Affidavit

I declare in lieu of oath, that I wrote this thesis and performed the associated research myself, using only literature cited in this volume. If text passages from sources are used, they are marked as such.

I confirm that this work is original and has not been submitted elsewhere for any examination, nor is it currently under consideration for a thesis elsewhere.

I confirm, that going to press of this thesis needs the conformation of the examination committee.

Julia-Theresa Fischer

Vienna, June, 2018

Danksagung

Ich möchte mich bei allen bedanken, die mir in der Zeit meiner Diplomarbeit hilfreich, konstruktiv, freundschaftlich und geduldig zur Seite gestanden sind.

Ein herzlicher Dank gilt meiner Familie. Vor allem meinen Eltern Gabriela und Alfred, die mich bereits mein ganzes Leben lang unterstützen und mir mit Liebe und Rat zur Seite stehen. Sie haben immer ihr bestes gegeben, um mir meinen Weg zu erleichtern. Ebenfalls meinem Bruder Alfred möchte ich hervorheben, der immer für mich da ist.

Für die Begleitung meiner Diplomarbeit möchte ich mich ganz besonders bei Dipl.-Ing. Martin Frank bedanken. Für seine Geduld, die vielen Stunden im Labor, die herzlichen und klärenden Gespräche und die aufbauenden Worte zur richtigen Zeit. Ich weiß das sehr zu schätzen.

Auch Univ.Prof. Dipl.-Ing. Dr.sc.nat. Philipp Thurner gilt mein Dank. Für anregende Ideen und die Unterstützung in der intensiven Endphase meiner Arbeit. Den anderen Kollegen und Kolleginnen des ILSB, die mir im Laufe meiner Diplomarbeit hilfreich und unterstützend zur Seite gestanden sind, möchte ich hiermit auch meinen Dank aussprechen.

Ein großes Danke auch an all meine Freunde, für bedingungslose Unterstützung und die vielen schönen, gemeinsamen Erinnerungen in den letzten Jahren. Ein besonderer Dank gilt dabei Jakob, der in den schönsten und auch in den schwierigesten Zeiten an meiner Seite war.

Danke!

Abstract

Osteoporosis is a widespread skeletal disease, which is a major problem of today's society. The current diagnosis and treatment of osteoporosis is based on the quantity of bone. Nevertheless, there is a growing awareness of the importance of the bone quality. Microdamage accumulation in bone may contribute to a loss in the quality of osteoporotic bone. The role of microdamage in fatigue fractures is widely unknown and the formation of microdamage in individual trabeculae under a defined uni-axial loading has not been performed so far. Therefore, this thesis investigated the quantification of microdamage formation in individual trabeculae under fatigue testing conditions in tension. A fatigue test protocol was developed and a stop criterion was defined to ensure microdamage formation without breaking the trabeculae. Several criteria were tested for this purpose. The decrease in elastic modulus, stress and strain amplitude and monitoring the whitening effect were excluded for various reasons. Nevertheless, with usage of a system with a higher resolution of the strain recording (temporal and local) it would be worthy to test these parameters further of their applicability. The number of cycles for which the samples were loaded and unloaded were chosen as stop criterion. Individual trabeculae were tested for 1500 (n=6), 2100 (n=6) and 3000 (n=7) cycles with a frequency of 1 Hz and an amplitude of 0.05 mm (whole sample). An adjusted preload was used to account for the variation in site of different sizes of trabeculae.

The samples were stained with chelating agent Alizarin Red S before testing and with Calcein afterwards to show the formation of microdamage. Confocal laser scanning microscopy (CLSM) was used to investigate the samples and to visualize microdamage. Linear cracks and diffuse damaged were detected in individual trabeculae after testing. By testing trabeculae for the mentioned different numbers of cycles the formation of microdamage was shown and the development of the different types of damages was studied. A 3-dimensional analysis of the samples was performed with the z-stack images of the CLSM, and a 2-dimensional analysis was executed to enable comparison to literature. It seems that with increasing cycles the number of diffuse damage increased more than the number of linear microcracks, but the differences are not significant for every set of cycles. To get more significant data a higher number of samples should be tested in the future. The developed test set-up and evaluation protocol can be used in future studies to determine e.g. differences in microdamage formation at the level of individual trabeculae between healthy bone and bone which is affected by osteoporosis. A major issue observed during this study was the varying definition of measuring diffuse damage and linear cracks and their quantification in the literature. A proposal is given in this thesis to unify the analysis method.

Contents

1 Introduction **1**

1.1 Motivation and Goal 1

1.2 Structure of Thesis 3

2 Biological Background **5**

2.1 Bone as a Tissue 5

2.2 Cortical Bone versus Trabecular Bone 7

2.3 Microdamage 9

2.3.1 Types of Microdamage 10

2.3.2 Detection and Repair Mechanisms 12

2.3.3 Biomechanical Consequences 14

3 Methodological Background **18**

3.1 Mechanical Fatigue Testing of Bone 18

3.2 Labelling of Microdamage 19

3.3 Confocal Laser Scanning Microscopy (CLSM) 21

4 Methods **23**

4.1 Sample Preparation 23

4.1.1 Dissection of Bone 23

4.1.2 Cutting Trabeculae 24

4.1.3 Size Measurement of Trabeculae 26

4.1.4 Embedding of Ends 26

4.1.5 Fluorescent Labelling 28

4.1.6 Application of the Speckle Pattern 32

4.2 Mechanical Testing 34

4.2.1 Setup and Modifications 34

4.2.2 Test Execution 40
4.3 CLSM Imaging 41
4.3.1 Preparation Steps for CLSM Imaging 41
4.3.2 CLSM Analysis 45
4.4 Data Analysis 46
4.4.1 Mechanical Data Analysis 46
4.4.2 Image Data Analysis 48
4.5 Statistical Analysis 52

5 Fatigue Test Design **53**
5.1 Parameters 53
5.2 Stop Criterion 55
5.2.1 Elastic Modulus 55
5.2.2 Amplitude 57
5.2.3 Whitening 59
5.2.4 Number of Cycles (NoC) 59

6 Results **61**
6.1 3-Dimensional Microdamage Analysis 64
6.2 2-Dimensional Microdamage Analysis 66

7 Discussion and Outlook **69**
7.1 Methods 69
7.2 Results 72
7.3 Outlook 76

8 Conclusion **77**

9 Appendix **78**

9.1 Protocol 78

9.2 Definition of ROI for Linear Cracks and Diffuse Damage 86

9.3 Results in Detail 87

9.3.1 Elastic Modulus 87

9.3.2 Stress Strain Amplitude 90

9.3.3 Stress-Strain-Data 93

9.3.4 CLSM Images 96

9.3.5 Maximum Intensity Projection Images 99

9.3.6 Additional parameters for 2-dimensional analysis 101

9.3.7 Display of Statistical Analysis 102

9.4 Template for Sample Holder 104

9.5 Histogram 105

1 Introduction

1.1 Motivation and Goal

One major problem of today's society is the demographic change in peoples age. People reach higher ages which is accompanied by diseases typically for these age-groups. Thefore, the interest to treat these long-term diseases increases. For example one out of four over 50 is affected of osteoporosis [1]. Osteoporosis is a systematic skeletal disease. According to the WHO criteria, osteoporosis is defined as a bone minear density (BMD) that lies 2.5 standard deviations or more below the average value for young healthy women [2]. A factor, which plays a role in the development of this disease is the decreasing bone quantity and quality with age. Osteoporosis or other diseases which lead to an decrease in bone quality can lead to fractures[1], which can be followed by immobility of patiens for longer periods of time. For elderly people immobility might lead to a fast decrease in muscle and bone mass. The loss of muscle and bone mass is followed by a higher human frailty [3]. Statistics show that around 50% of people over an age of 80 fall at least once a year. These falls can lead to injuries, such as hip fracture, leg- and arm-fractures. Up to 50% of elderly people, who get stationary treated die during the first year post-treatment (Robert Koch-Institut 2009). [1]

A goal of today's biomechanics research is to improve the diagnosis and treatment of osteoporosis and to better understand the factors which contribute to bone fracture. One major limitation is that current diagnosis and treatment of osteoporosis are based on bone quantity and not bone quality. The quality of bone depends on several factors, among them: bone geometry, trabecular microstructure, microdamage amount and distribution and density of osteocytes. The current diagnosis tools like dual energy x-ray absorptiometry (DEXA), fracture risk assessment tool (FRAX), ultrasound and computer tomography are mostly assessing bone mass and not bone quality. Bone mineral density (BMD) is often brought in connection with bone diseases. As already mentioned this is based on the WHO definition of osteoporosis when the so called T-score[2] is smaller than -2.5 which is an indicator of low BMD.

Current treatment of osteoporosis is based on increasing BMD. Bisphosphonates (BPs) are the actual first-line medications for the prevention and treatment of osteoporosis. Bisphosphonates effectively reduce the amount of osteoclast and thereby reducing the resorptive phase of bone remodelling [4]. Pazianas et al. (2014) also stated that BPs

[1] A fracture causes the continuity of bone tissues or bony cartilage to be disrupted or broken. A fracture can have different origin like stress or fatigue.

[2] The t-score gives the deviations from young healthy average BMD.

prevent further deterioration of the bone micro-architecture. However BPs also increase mineralization in bone and reduce the ability to absorb energy, which may lead to a accumulation of mircodamage [4]. This leads to the conclusion that the treatment with BPs does not decrease the amount of microdamage.

To improve preventive and therapeutic strategies for skeletal diseases, such as osteoporosis, a better understanding of the mechanical properties of bone and their influence on cell-mediated adaptation processes is necessary. The macroscopic mechanical properties of bone are determined by composition as well as nano-, micro- and structural organization [5].

A main topic dealing with these issues is microdamage in bone. As already mentioned the existence of microdamage has an influence on bone quality and likely also on fracture risk. Accumulation of microdamage weakens the bone matrix and in excessive amounts may even lead to stress fractures. The formation, detection and repair of such microdamage is therefore of large interest.

An interesting approach to the research topic of microdamage is the age-dependency of microdamage. Older individuals are more likely to develop bone disease like osteoporosis, which leads to an accumulation of microdamage. This microdamage weakens the bone. However, there is also a difference in the type of microdamage developed in older bone compared to younger bone.
Microdamage can be categorized in different types (see section: 2.3.1 Types of Microdamage). The two main types are linear microcracks and diffuse damage. Apparently the number of linear cracks is higher in older bone than in younger [6], [7], [8]. Diffuse damage does not show an age dependency [6].
As already mentioned osteoporosis gets mostly treated with BPs. BPs reduces the amount of osteoclasts, which are responsible for the dissolution and absorption of bone. Therefore the bone quantity increases, but conversely the damaged bone does not get remodelled as regularly. Seref-Ferlengez et al. (2014) presented that diffuse damage can be repaired directly in vivo, without the intervening step of bone remodeling [9]. This raises the question if osteoporotic bone builds more linear cracks due to the age- and disease-dependent change in bone matrix composition or if the different repair processes of linear and diffuse microdamage have an impact.

Most studies deal with microdamage formation in cortical bone. Nevertheless, most fragility fractures occur in regions where trabecular bone is dominant as these are regions where high stresses and strains occur [10]. As the structure is different in trabecular and cortical bone (see section 2.2 Cortical Bone versus Trabecular Bone) the development of microdamage may also be different. For example vertebral bodies are composed mainly of

trabecular bone. In 2000 1.4 million out of 9 million osteoporotic fractures were vertebral body fractures [11].
Due to the arguments presented above, it is of great interest to enlarge the knowledge of microdamage formation in trabecular bone [12]. Current studies deal with microdamage formation in networks of trabecular bone [13], [14], [15]. This thesis engages with fatigue testing on individual trabeculae. Testing of individual trabeculae has the advantage to investigate its behaviour under a defined loading state. When testing a network of trabeculae it is impossible to make statements about the load acting on individual trabeculae as it gets distributed within the network. The defined uniaxial loading state at the tests allows to see the direct effects of loading on the individual trabecula. The fatigue condition was chosen as it is similar to the physiological load in vivo. Fatigue is a failure process that was originally characterized in engineering materials, when relatively small loads, well below the failure strength, are applied repetitively and eventually small cracks form and grow.[6]

Therefore, the goal of this thesis was to test individual trabeculae under fatigue loading to generate microdamage. Further, the formation and development of the damage was to be detected. The trabeculae should be loaded until microdamage occurs, without fracturing the sample during testing. Hence, a test protocol had to be designed. Fitting parameters for testing individual trabeculae had to be evaluated and a stop criterion had to be determined. Further, the formation and behaviour of microdamage was investigated. To visualize microdamage labelling with fluorochomes of the trabeculae was performed. Therefore, a staining protocol and a fitting analysis method were developed.

The test protocol developed in this thesis enables a wide spectrum of possibilities for further tests. During this thesis bovine bones are tested. In further studies it would be of interest to also test human bones to see if the obtained observations can also be applied. The difference between old an young bone could be investigated with regard to the types of microdamage formed. Further investigations in the different behaviour of microdamage formation in osteoporotic and healthy bone would be a desirable goal.

1.2 Structure of Thesis

This thesis is structured in 9 chapters. First in the general introduction the motivation and goal of the thesis are defined and an overview of the next chapters are given.

Chapter 2 engages with the biological background required for this topic. The composition and characteristics of bone are discussed and the difference between cortical and

trabecular bone are shown. Also the concept of microdamage is introduced and discussed in detail.

In the following section a short introduction into the methodological part of this thesis is given. Providing the basic ideas necessary for this thesis. Such as fatigue tests, confocal laser scanning microscopy (CLSM) and microcrack labelling. This closes the background chapters.

Afterwards the methods used during this thesis are explained and discussed. The sample preparation is important for the success of the experiments. Therefore a major part of the thesis engages with this process. The setup for the mechanical testing is explained and settings are documented. The next step is the preparation of samples for CLSM imaging and the microscopical analysis of microdamage. Then, the gained images are evaluated and the necessary steps are explained. The last subsection in Methods is the documentation of the statistical analysis.

As the development of a fitting test design was a major part of this thesis the next section deals with this topic. The different parameters are discussed and the way to find an appropriate stop criterion is presented. This section also includes the interim results, which were necessary to define the stop criterion.

The results section deals with the analysis of the CLSM images. This section is splitted into a 2D and 3D mirodamage analysis as both were executed.

The discussion and outlook are subdivided. As a major part of the thesis was the development of a fitting test design. The limitations and advantages of this methods are discussed there. The second part of the discussion deals with the results of the data analysis and obtained results are critically discussed.

In the appendix the final test protocol can be found. It contains every step necessary to repeat the experiments and the analysis. It also contains additional results and images. And additional templates can be found there.

2 Biological Background

2.1 Bone as a Tissue

The human skeleton protects vital organs and is a reservoir for important minerals, growth factors and cytokines [16]. It is the framework of our body and helps to withstand load an stresses due to daily activities. As such the skeleton is always changing and adapting to these activities. Bone is a hierarchical structure based on a nano-composite [3]. It has a porous mineralized structure and is a complex anisotropic, heterogeneous material which serves as the main load-bearing structure in the body. It consists of a mineral phase mainly hydroxyapatite (Ca10(PO4)6(OH)2), an organic phase and water. The organic phase consists up to 90% of collagen type 1 and the other 10% split into non collagenous proteins (NCPs) and lipids. The tendency of bone to fracture is dependent on different bone quality factors like the presence of microcracks, collagen content and crosslinks and the quality of mineralized tissue which is measured in clinical terms with the bone mineral density (BMD). Each of this factors varies with age, gender, ethnic, disease and therapy. [18], [19]

In order to understand the mechanical properties of the martial bone, it is important to know the mechanical properties of its components at the various levels of the hierarchical structure and the relations between them. Figure 1 illustrates the hierarchical structure of bone. At the macroscopic level (several cm to 10 mm) bone can be divided into two types: cortical (also compact) and trabecular (also cancellous) bone. At the next level the microscopic structure of bone can be observed (10 mm - 500 μm). In cortical bone this comply with the Haversion system and the network of trabecular in cancellous bone. At the scale from 500 - 10 μm single trabeculae and osteons can be observed. At the nano-structural level fibrillar collagen and embedded minerals are visible and smaller than that the molecular structure of constituent elements (for details to the single components of bone see section: 2.2 Cortical Bone versus Trabecular Bone).

[3] Nanocomposites are solid materials that have multiple phase domains and at least one of these domains has a nano-scale structure[17]

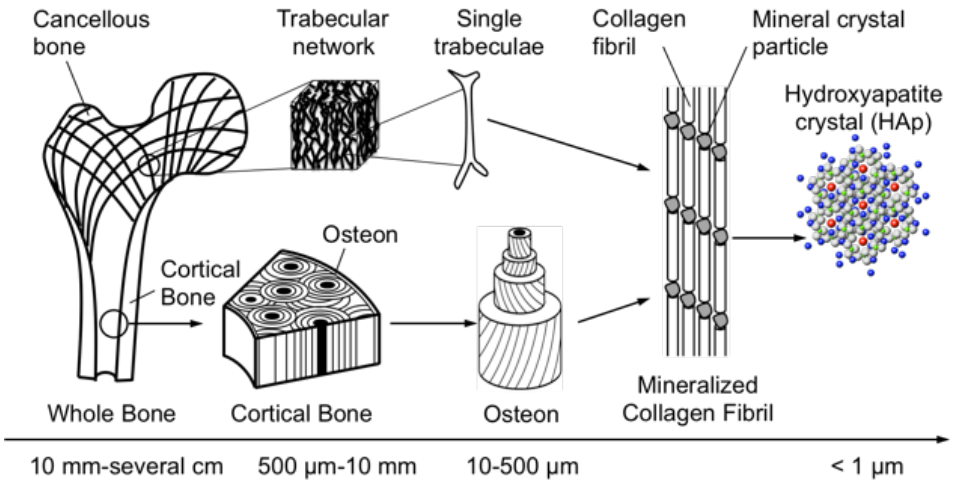

Figure 1: Hierarchical structure of bone [20]

Bone is remodelled the whole life time so that our skeleton can adapt perfectly to its effect of action. Remodeling is a process in which bone is renewed and adapted to its mechanical load and other biomachanical forces. Microdamge gets repaired and if necessary the structure of bone is modified. In the first years of life the remodelling process is done to 100% as the living organism is growing constantly in these ages. For adults the remodelling decreases to 10% [21]. The skeleton has a peak bone mass (PBM), which is the maximum bone mass a human will ever have during his life. PBM is reached approximately at age 30 depending on height, gender and diseases [3]. After reaching PBM the bone mass decreases slowly. Therefore, diseases of the skeleton like osteoporosis or fractures are more likely increasing with age.

All these processes are the same for the whole skeleton. But it can be distinguished between two categories of bones and their functions, the Long and the Flat bones. Long bones are located on the limbs. They support the weight of the body and enable movement of limbs. Flat bones are mostly present in the body core and serve as protection of inner organs like the skull and as load bearing structure like the vertebrae column. Long bones consists of a long hollow shaft and two head regions (see figure 2). The shaft is built of cortical bone. The head regions only consist of a thin layer of coritical bone (cortical shell) which surrounds the inner trabbecular bone [22]. Flat bones consist of a layer of trabecular bone lines on the sides with compact bone. So it can be noted that cortical bone is more dense such that it can withstand compressive forces. In comparison, trabecular bone can support shifts in weight distribution through its structure.

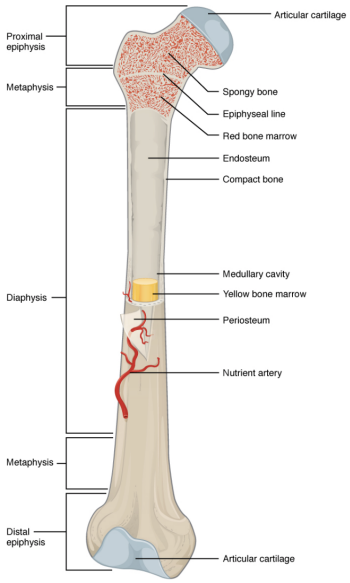

Figure 2: Anatomy of a long bone [22]

2.2 Cortical Bone versus Trabecular Bone

Cortical bone builds the outer layer of bones. It is mostly found in long bones and at the outer layer of bones. Around 80% of the human skeleton is made out of cortical bones [19]. It consist of progressively smaller structural elements, so called osteons. Cortical osteons are called the Haversian systems, a hollow cylindrical structures surrounding blood vessels [16]. They build the fundamental functional unit of cortical bone. Osteons are interfaced from the interstitial bone tissue by a thin layer, the cement line [23]. Osteons appear in cortical bones layered structures made of concentric lamellae (see figure 3). Inside the lamellar structures sit the osteocytes in a space called lacunae with an approximately size of 15x7x5 μm. [24], [23]

Cortical bone is a compact and dense tissue which has a high resistance against bending and torsion. The main functions are support of the whole body weight, to provide mechanical strength and protection, to provide levers for movement and participate in the metabolic cycle as it stores and to release minerals. [19]

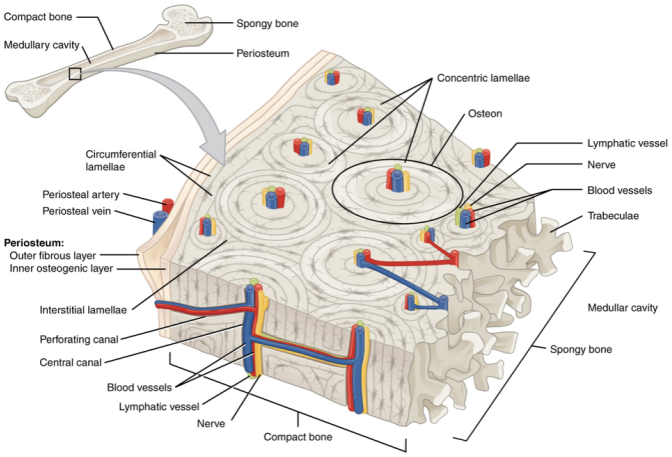

Figure 3: Crosssectional view of cortical bone [22]

Although the chemical composition of cortical and trabecular bone is the same they are macroscopically and microscopically different [19]. Trabecular bone is mostly situated in the ends of long bones and fills the space in irregular bones. Around 20% of the human skeleton is build up by trabecular bone. It is highly porous at the macroscopic level as it is formed by a complex network of rods and plates (bone trabeculae) (see figure 4). They transfer loads from joint faces to joint faces via the midshaft by avoiding stress concentrations [25]. As bone is always reorganizing, trabecular bone can change its orientation and optimize the load transfer. Therefore trabeculae form along lines of stress to provide strength. In this way they show favoured orientation for effective load transfer (see Wolff's law [26]). Thus, trabecular bone can be seen as a light weight structure. It minimizes the weight of bone and enables an easier movement of the bones for the muscles. In flat bones, the space between the single trabeculae is filled with red bone marrow, where hematopoiesis occurs. [22], [23]

Trabecular "osteons" are called packets. They have a semilunar shape and are composed of concentric lamellae [16]. Alike to cortical bone the individual lamellae consist of mineralized collagen fibrils, containing ellipsoid cavities, so called lacunae. They are typically 5–15 μm in cross section and 26 μm in length. Trabecular bone is less mineralized than cortical bone and has a higher water content (27% vs. 23%) [27].

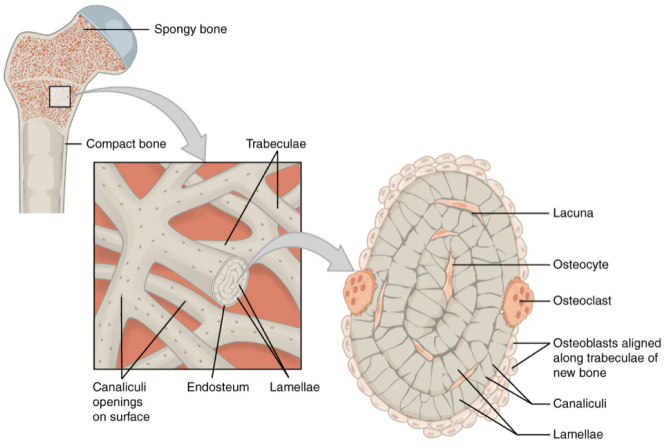

Figure 4: Schematic image of trabecular bone [22]

2.3 Microdamage

Biomechanical damage in bone cannot be avoided. During a lifetime bone can be exposed to physiological distress and diseases. Ageing and its effects have a huge impact on bone quality. All this weakens the mechanical properties of bone. Because of body weight and the action of muscles bone is exposed to high forces and might be damaged over time. As a result of these fatigue loads small cracks of different kinds can occur. These cracks are called microdamage. Healthy bone can deal through remodelling with this kind of damage and catastrophic fractures can be avoided. But accumulation of microcracks increases the fragility of bone and leads to a degradation of the mechanical properties. Such accumulations occur especially in diseased bone or bone which was under psychological distress over a longer period of time. Microcracks have to be visualised and detected for investigation. A possible approach is the creation of models, which simulate the whole process of microdamage formation with the assumption that the number of microdamage increases with time. Repair is then defined as a decrease in the amount of damage. But the bone quality is not taken into account, which shows a deficit of this method. In combination with finite element analysis an entire bone can be modelled to demonstate its loading patterns. These models also can predict the stable equilibrium between damage and reapir and also illustrate the consequences of an imbalance (like in osteoporosis). [28] Detection of microdamage in living individuals to calculate the risk of fractures is another issue. They cannot be seen with ordinary imaging tools in hospitals like x-rays and CTs, because of their small size. Thus, yet it is not possible to detect microdamage in vivo. The best established method to make microdamage visible is labelling with flourochromes. For details see section: 3.2 Labelling of Microdamage.

2.3.1 Types of Microdamage

There are different types of microdamage, as shown in figure 5. The most common are linear microcracks and diffuse damage [6]. Each of these types has his own distinct characteristic. Seref-Ferlengez et al. (2015) defined linear microcracks with a length around 50-100 μm and sharply defined boarders. They occur mostly in interstitial bone and in regions of compression or shear arears. They are a result of daily repetitive loading of the same area during cyclic movements as walking or running [6]. Schaffler et al. (1995) and collegues reported the number of linear microcracks as a function of age [8], [7]. This means that the higher the age of an individual the larger the number of linear microcracks gets. They also tend to be longer in the longitudinal axis of the bone as cracks tend to follow the microstructure of the bone.
Diffuse damage consists of clusters of small sublammellar sized cracks. This type of damage separates mineral aggregates from each other and from the surrounding organic matrix [6]. In contrast to linear microcracks diffuse damage seems to appear more often in tensile regions of the bone. The damage can occur very rapidly but also trough constant load over a long period. However, in difference to linear microcracks there was no age dependence observable [6].
Cross-hatching is a further type of microdamage. It is formed by multiple cracks of intermediate size [6]. Choi et al. (1992) stated that in trabecular bone also more complicated patterns of microdamage can be observed. This can be ascribed to the complex microstructure of trabeculae. [29]
Men seem to tend to have more diffuse damage than women. This is notable because women have in general a higher risk for developing osteoporosis and therefore have a higher fracture rate in age than men [30]. Beside their differences both types are equally important and seem to have the same probability distribution [31].

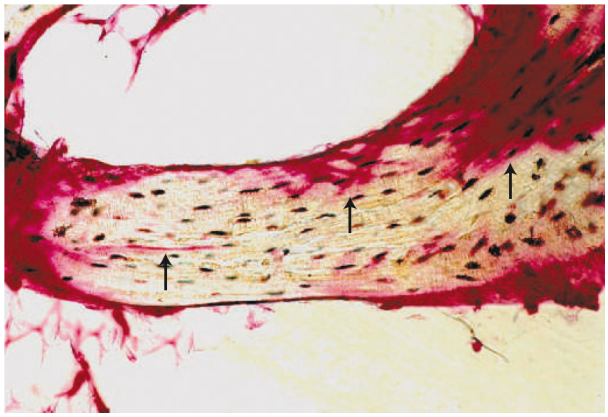

Figure 5: Examples for microdamage in compact bone.
From left to right: linear microcrack, cross-hatching and diffuse damage [32].

Fazzalari et al. stated in 1998 with their study that diffuse damage appears the same when viewed in three orthogonal planes (see figure 6) [33]. In contrast linear microcracks show a sheet-like extent in 2 planes. They appear either as straight, curved, or a combination of both [33]. This study is worth mentioning because it contributes to the understanding of microdamage behaviour. It was the first study investigating microdamage with confocal laser scanning microscopy (CLSM) and thereby working out the differences in the nature of different microdamage types. However, no study has replicated the findings of Fazzalari et al. since 1998 and therefore, their results should be treated critically. But beside this issue this study confirm the assumption that different types of microdamage exist and that CLSM is a proper tool to visualize them.

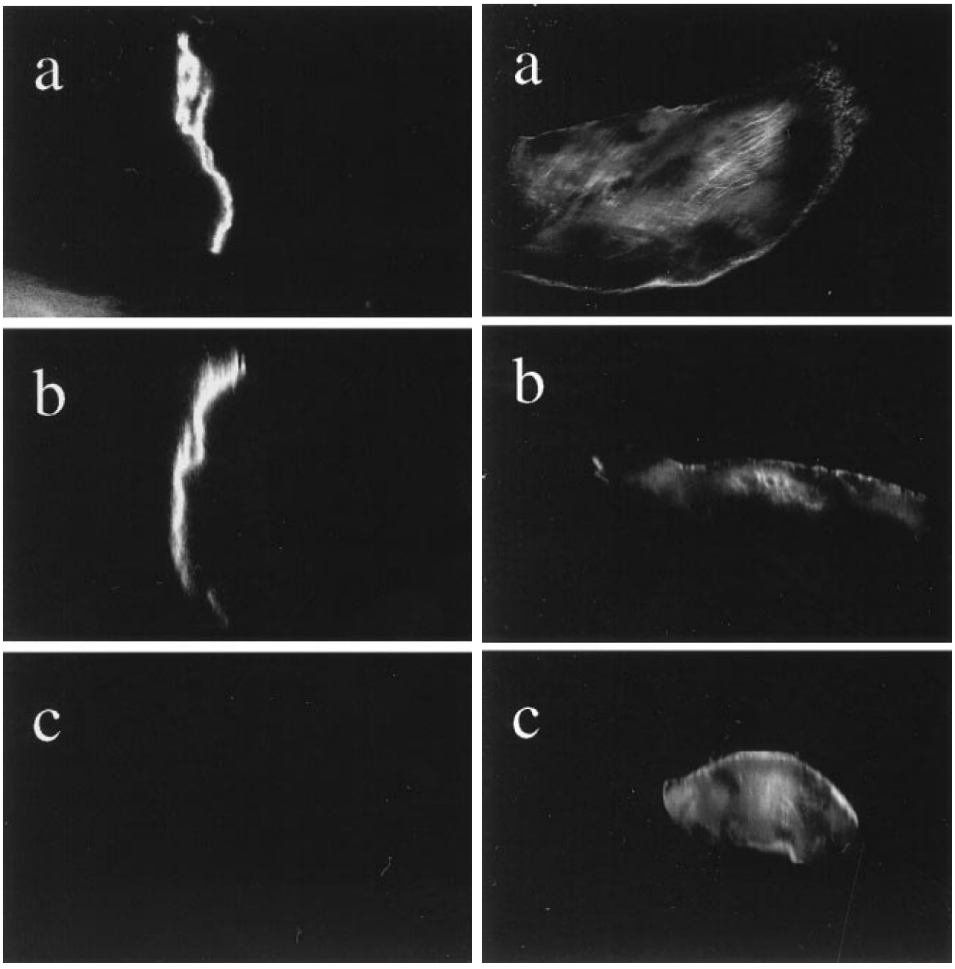

(a) Linear microcrack (b) Diffuse damage

Figure 6: Stained microdamge by Fazzalari et al. (1998) [33]
Viewed in 3 planes a) x-y-plane b) x-z-plane c) y-z-plane

2.3.2 Detection and Repair Mechanisms

To understand the principals and models of detection and repair of microdamage it is necessary to understand the basics of bone remodelling. As already mentioned bone is remodelled through lifetime all the time. Therefore, microdamage gets repaired through bone renewal. Sequentially, it is necessary to have a look at the structure of bone. The process of remodelling is driven by the actions of bone cells (osteoclats, osteoblasts, osteocytes). [19], [34]

Osteoclasts are large multinucleated cells which are responsible for the dissolution and absorption of bone [35]. They are formed out of cells of the hematopoiesis and around 1% of the bone surface is covered with osteoclasts. Osteoblasts are responsible for the synthesis and mineralization of bone matrix (osteoid) during both initial bone formation and later bone remodelling [36]. They are chain-shaped arranged on the bone surface. Osteboblast and Osteoclasts form together basic multicellular units (BMU) which are responsible for bone resorption and bone formation [37]. Figure 7 illustrates cells and the remodelling process in a BMU.

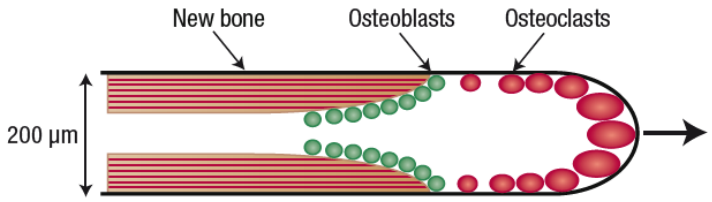

Figure 7: Bone repair mechanism.
Basic multicellular unit (BMU) eats away old and generate new bone [28].

Osteocytes are the primary cells of mature bone and the most common type of bone cells. They descend from osteoblasts and are formed by the incorporation of osteoblasts into the bone matrix and their change in structure during this process. Osteocytes build a network of channels, so called canaliculi to infuse the bone. In this way osteocytes are connected to each other and the bone surface. They build a widely spread communication and circulation network through which they send a signal to the osteoblats on the bone surface about microdamage, take care of the disposal of metabolic products and nutrient transport. They detect strains and microdamage and give in case of need the signal to start remodelling. [34]

But how are microcracks detected and what is the impulse for remodelling? A good starting point would be the change in mechanical properties due to areas where cracks

occur. At the tips of the cracks the stresses get high and along their sides normally stress decreases. So in total these changes in stress even out and it would be invisible to a BMU. But, as already mentioned osteocyctes are cemented into the bone and they built a network of cancaliculi through the bone through which they communicate. Some cells become apoptotic through microdamage [38] and the network gets disconnected. Taylor et al. (2007) showed, using fracture-mechanics theory, that cellular processes can be disrupted by shear motions that occur in crack regions. They showed that the number of damaged processes were dependent on the applied stress and crack size. Further they worked on a process to identify the triggers for osteoclast precurors to stimulate the formation of a BMU [28].

Some microdamage in bone can be a signposts for fractures. On the other hand others do not present danger at all. This depends on various factors like accumulation of damages, age, physical fitness, diseases and even gender. If such damage presents a potential harm for the skeleton also depends on the ability of the body to repair such structures and toughening the bone.

With increasing age the remodelling of bone gets less, the bone mass decreases and the risk for diseases like osteoporosis increases. These effects contribute to an imperfect bone remodelling and microdamage cannot be repaired effectively anymore. Osteoporosis is currently treated with Bisphosphonates (BPs). BPs are a group of anti-resorptive medications which reduce effectively the amount of osteoclast and thereby reducing the resorptive phase of bone remodelling [4]. There are diffrent types of BPs available and therefore, individual BPs inhibit bone resorption to various degrees due to differences in their physico-chemical structure.[6]. Mashiba et al. (2010) and Allen et al. (2006) reported that 40–50% suppression of remodelling from BPs treatment resulted in an 3 times increase in damage accumulation. These studies were executed on healthy young adult beagle dogs receiving BPs [39], [40]. Stepan et al. (2007) reproduced their findings for human iliac crest bones [41]. As BPs causes a change in the osteoclast-osteoblast-balance the remodelling of microdamage. The microdamage does not get repaired in the same frequency as in healthy bone.

Also the influence of the different types of microdamage on the remodelling process is of question. Herman et al. (2010) showed that diffuse damage in rat ulna did not cause apoptosis of osteocytes and therefore, did not evoke the remodelling process [42], [6]. Seref-Ferlengez et al. (2014) presented that diffuse damage can be repaired directly in vivo, without the intervening step of bone remodeling [9]. The question arises if diffuse damage has an impact on the bone quality at all and how do these self-healing processes work. It appears that the body has unique capabilities to deal with this type

of microdamage that does not involve traditional bone remodeling [6].

On the one hand, microdamage in bone can grow very fast, on the other hand, it can also expand over a long period of time. Hazenberg et al. (2006) showed that the growth rate can also stop when the crack meets an element of the microstructure like osteons. Therefore the micro- and ultrastructure in bone tributes a big part in the toughening effect.

2.3.3 Biomechanical Consequences

The change in nanostructure through age influences crack propagation and toughness (see figure 8). Diab et al. (2006) and Schaffler et al. (1995) postulated in theire studies an age dempendany in crack propagation, which leads to a change in mechanical properties dependent on age [8], [7]. The material property called fracture toughness (Kc) describes the capability of bone to withstand fracture. As bone is a composite material it can be stated that it achieves as whole structure higher thoughness than that expected of its constituents like collagen or hydroxylapatite [28]. However, the mechanism of toughening is not fully understood yet. Katsamenis et al. (2015) investigated the osteonal-, micro- and tissue-level mechanical behaviour of cortical bone tissue samples from young and elderly donors. Among others they performed fracture toughness experiments and showed that bone's fracture toughness and crack growth resistance at the tissue level are significantly correlated to damage susceptibility at the micro level and mechanical inhomogeneity between lamellae and interlamellar areas at the osteonal level. [43]

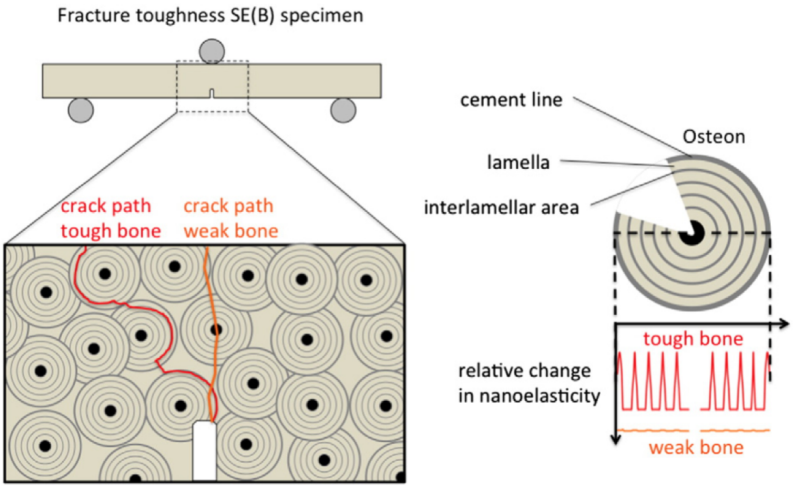

Figure 8: Schematic crack propagation in young and elderly samples. Inhomogeneity of the nanoelasticity leads to crack deflection and longer crack paths compared to aged bone where straighter, shorter cracks are present. [43]

In this context, microdamage can be seen positive (i.e. lowering stress concentrations) or also negative (lowering strength). Importantly, the accumulation of microdamge influences the structural integrity of bone on different levels and changes therefore its mechanical properties. Obviously bone can only deal with a certain amount of damage before the bone finally breaks. Seref-Ferlengez et al. (2015) postulated that the accumulation of microdamge in cyclic fatigue loading is not linear. 3 phases are distinguished by these authors (see figure 9). In phase 1 damage starts to occur and the elastic modulus drops relatively quick to a certain point. In the second phase the amount of microdamage stays constant and the elastic moduls stays therefore the same. During this phase the microcracks interact with the surrounding structure. The already existing cracks grow eventually but there is no noteworthy chance in stiffness or strength of the bone. Bone stays in this phase during fatigue testing most of the time. In phase three damage overwhelms and the microcracks grow. They consolidate and the modulus decays until the bone fails. [6]

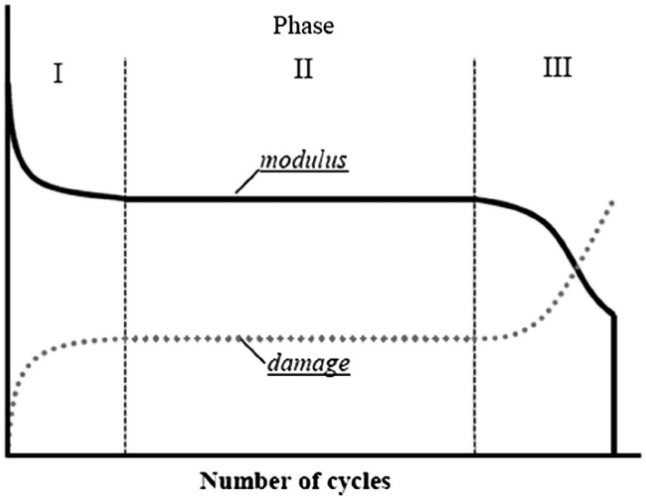

Figure 9: Model of elastic modulus loss under fatigue loading [6].

As mentioned before, it also has been shown experimentally that microdamage accumulation in fatigue can have a paradoxical beneficial role for energy dissipation in addition to its dominantly role of bone weakening [6]. This shows the complex nature of microdamage and its effects. Microdamage is a way to dissipate energy and therefore prevent bone from acute failure. Specifically, diffuse damage seems to be effective in terms of energy absorption. Diffuse damage creates lots of small interfaces in the bone matrix which appear to help with the energy absorption. As the formation of diffuse damage is influenced by factors like age, diseases and gender therefore, the amount of energy which can be dealt with varies. This lead to a change in mechanical effectiveness of the material bone.[6]

Also structural interfaces like minerals, collagen fibrils, lamellae, lacunae, cement lines and osteons work as a toughening mechanisms to prevent the growth of microdamage. These interfaces are connected by so called noncollagenous proteins (NCP) which absorb energy during microdamage [44].

Morgan et al. (2015) investigated the effect of different NCPs on skeletal mechanical properties [45]. There are some which are of interest in the context of bone toughening and microdamage formation. Therefore, Poundarik et al. (2012) investigated the involvement of the NCPs osteocalcin (OC) and osteopontin (OPN) in bone fracture [46]. OC and OPN are the most common NCPs in bone [45]. OPN imparts in bone an ability to resist crack growth and plays a role in the repair of bone matrix damage [46]. Poundarik et al. (2012) studied at mice the impact of dilatational bands in bone fractures and microdamage formation. Dilatational bands are distinct ellipsoidal voids, which are around 100 nm in size. They form through deformation of NCP complexes embedded within

the bone matrix. They showed that these bands colocalize with OC and OPN and form in between fused mineral aggregates [46]. They discussed the role of OC and OPN in microcracking and postulated that the dilatational bands at the nanometer scale of bone affects also damage at higher scales, like diffuse damage. The investigation of diffuse damage shows the formation of dilatational bands under high resolution instruments (e.g. high-resolution laser confocal-, atomic force-, and scanning electron-microscopy) [46]. The formation of dilatational bands occurs before any collagen fibril deformation or separation of mineralized fibril [46] and causes matrix failure in form of diffuse damage. Furthermore, Poundarik et al. (2012) found that NCPs OPN and OC are higher concentrated in regions of diffuse damaged areas containing dilatational bands. [45], [46]

This raises the question how the NCP level relates to osteoporosis and age. It is not entirely clear yet, but Grynpas et al. (1994) stated a age-depenency of the NCP level [47]. Interestingly also the dominate type of microdamage changes with age. As mentioned above linear cracks show an age-dependency and more linear cracks than diffuse damage are found in older bone in vivo and in vitro [7], [8]. Hence, it is clear, that microdamage and its relation to NCP level, age and bone composition needs to be further investigated under physiological meaningful conditions.

3 Methodological Background

3.1 Mechanical Fatigue Testing of Bone

Microdamage of bone has a direct influence on the fracture risk of bone. In healthy bone mircodamage gets remodelled to a certrain extent. Nevertheless, stress fractures can harm healthy bone and the role of exisitng microdamage is of interest. For example Hughes et al. (2016) investigate the influence of remodelling on the risk of stress failures [48]. Burr et al. (1997) also investigated stress fractures dependent from bone mass and microdamage [49]. But even more, if a muskoskeletal disease like osteoporosis occurs or through ageing the risk of fracture is even more present. Therefore, it is of great interest to study the formation and development of microdamage and their influence on the mechanical properties of bone. Numerous studies of microdamage formation in cortical bone have been conducted, but data in trabecular bone is lacking.

Mechanical testing of bone is a wide field of research. Through analysing different levels of its hierarchical structure at different length scales, information about the different mechanical behaviour of bone is gained [50], [3], [23]). Also bone is tested under different loadings (compression, tension, shear...) to gather as much information as possible [23]. Mechanical testing of individual trabeculae has some challenging aspects. Testing on the micrometer length scale and sample preparation requires high precession. There are already studies existing testing individual trabeculae not in tension under fatigue conditions. Frank et. al. (2017) develped a set-up to test trabeculae in tension in a close to physiological enviroment [51]. They were able to determine tissue-level properties and found that individual trabeculae can withstand much higher strains as previously reported (ruptered at a local strain of 19.7 ± 6.6 %) [51].
But most studies executing test on individual trabeculae in tension test till failure. However, the common test profile for producing microdamage is a fatigue setting. Cyclic loading and unloading imitates the physiological load of daily life and should ultimately lead to fatigue of bones. Cyclic loading produces microdamage that accumulates with each cycle and the damage increases as the intensity of testing increases. Intensity can be varied through change in the load magnitude and through the number of cycles to which the specimen is exposed. Additionally, the displacement and frequency contribute. The number of cyclical load required for propagation of the fracture decreases rapidly and further there is a strong negative correlation between load intensity and number of cycles needed for failure. [52]

For example, Wu et al. (2013) demonstrated in an in vivo experiment the formation of

microdamge in cortical rat ulna under cyclic loading tests and their remodelling [53]. For cortical bone many studies exist about the behaviour under different kinds of loads and fatigue. In addition to the formation of cracks, there are also numbers of studies about the propagation of microdamage in cortical bone [50], [3].

Similarily, for trabecular bone there are a number of studies about the behaviour of the trabecular network but hardly any study describes the behaviour of individual trabeculae. Nevertheless it is important to get an extensive understanding of this part of our sekeleton. Hence, it is the main component which resists cyclic movements like during walking or running. In comparison, it gets 25% as dense, 500% as ductile and 10% as stiff as cortical bone [21]. Some studies exist where the crack propagation in a networks of trabeculae is monitored. Bowman et al. (1998) did fatigue tests on trabecular network with the result that cyclic loading reduces stiffness up to 70% after 10^6 cycles [54].

Ashman et al. (1989) and Rohl et al. (1991) showed that the elastic behavior of trabecular bone in compression and tension are the same [55], [56]. In contrast, microdamage formation in bone is not equal in tension and compression [6]. Therefore, the loading type has to be taken into account in the analysis and interpretation of the test results. Beside frequency and amplitude also the load type is of interest. Shear, torsion or axial load have different influences in microdamage formation. Wu et al. (2013) tested trabecular networks in compression, shear, and multiaxial loading for microcrack propagation. They found that 50% of in vivo microcracks propagated under each loading type and that damage formation was positivly correlated to a decrease of compressive stiffness following both axial and shear loading. [57]

3.2 Labelling of Microdamage

Fatigue-induced microdamage plays an important role in bone as it contributes to stress and fragility fractures [58]. However, labeling of microdamage proves to be challenging. The difficulties arise due to the sample preparation process, in which the sample is manipulated and possibly causing microdamage. Also in older bone microdamage generated in vivo is present. Sequentially, this pre-existing microdamage must be distinguished from the one generated during testing, for the analysis. Microdamage can be seen as discontinuities in the calcium bone matrix, which can be visualized through chelating agents. These agents bind to calcium and thereby label the cracks [58]. Lee et al. (2000) introduced a sequential labelling technique of microdamage in bone using chelating agents [59]. They managed to develop a method to differentiate between already existing microcracks and test-introduced ones. Further they were able to label microcrack growth

through staining with different agents at different stages of the testing process.

O'Brien et al. (2002) adapted the results of Lee et al. (2000) to find the optimal sequence of application and optimal concentration of fluorochromes to ensure equally bright fluoresce of the different agents (see figure 10). O'Brien et al. (2002) used ion chromatography to measure the affinity of each chelating agent binding free Ca^{2+} ions. The used chelating agents were Alizarin Complexone (A), Calcein Blue (CB), Xylenol Orange (X) (A, CB, X: Aldrich Chemical Co., Milwaukee, WI, USA) and Calcein (C) (Sigma Chemical Co., St. Louis, MO, USA). Each chelating agent fluorescences at a different wavelength and makes visualization of microcrack growth possible. Agents were ranked in order of decreasing affinity for calcium. The optimal concentration was found through looking at the substitution of the agents and adapting the concentration. This process lead to the following staining protocol: A-X-C-CB with the a concentration of 5 x 10^{-4} M of A, X and C and 1x 10^{-4} M for CB. [60]

The samples were immersed in a petri dish containing the aqueous solution of a single chelating agent. This petri dish was then placed in a vacuum desiccator for 4 h to ensure maximum penetration of the agent. Afterwards the specimen was washed with de-ionised water. [60]

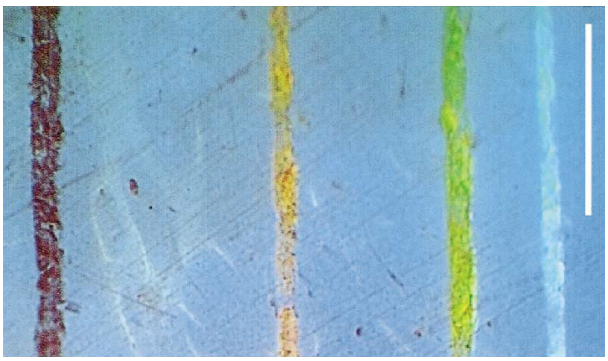

Figure 10: Sequence of chelating agents.
Efficient sequence of chelating agents, from left to right: Alizarin Complexone(0.0005 M), Xylenol Orange (0.0005 M), Calcein (0.0005 M) and Calcein Blue (0.0001 M) [60]

The labelling method for microcracks design by O'Brien et al (2002) was applied in a study on age related changes in human trabecular bone by Green et al. (2011). However, Green et al. adapted the protocol to their work and thereby used slightly different concentrations. For labelling the pre-existing microcracks they used 0.02% Alizarin Complexone and 0.005% Calcein for marking the induced cracks. Furthermore they performed staining for 8 h at 4 degree Celsius and at atmospheric pressure. [3]

These two studies were taken into account to provide the labelling protocol for this project (see section: 4.1.5 Fluorescent Labelling).

3.3 Confocal Laser Scanning Microscopy (CLSM)

The major application of Confocal Laser Scanning Microscopy (CLSM) is imaging of fixed living tissues labelled with fluorescent agents. Marvin Minsky patented 1957 the technique but he was limited by the existing technology by that time. Through technological improvements the method has been further developed over the years, becoming an important application in microscopy. Confocal microscopy combines fluorescence microscopy, laser light illumination and computer image processing [33].

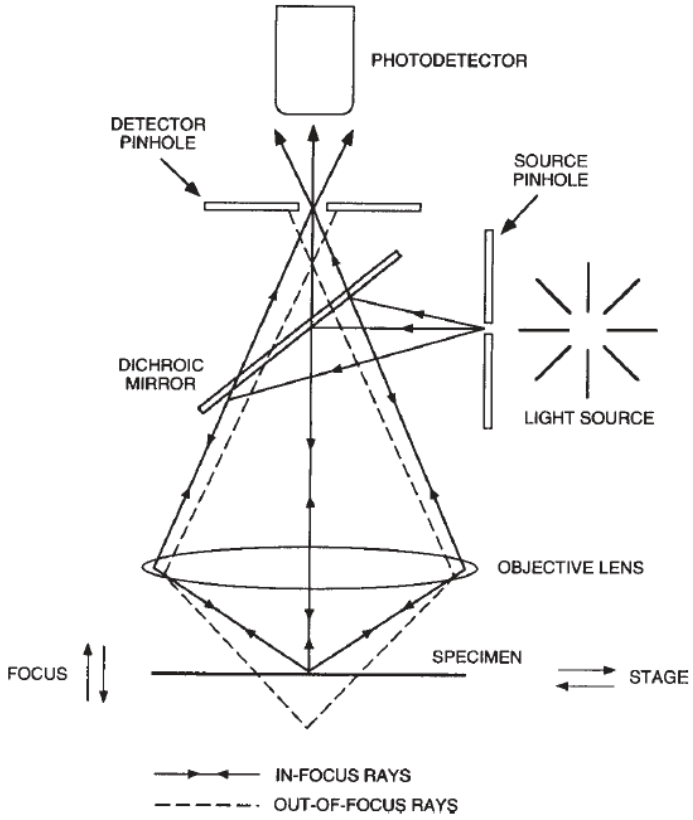

Figure 11: Light path of CLSM [61]

In figure 11 the light path of a typical CLSM is displayed. The light path is in general the same as in a conventional reflected-light microscope but two pinholes are placed in the path. One in front of the light source and one in front of the photodetector. The used light source is a laser. The pinhole at the light source, focus point on the sample and the pinhole in front of the detector are all confocal with one another. [61]

In CLSM a laser beam is focused at a defined depth of the sample. The sample gets scanned by the laser at different depths through the whole sample. In this way optical sections of the sample get combined to an image with high resolution in x-, y- and z-direction. [58] The advantage of CLSM, in comparison with normal light microscope, is that the fluorescence in the focal plane does not interfere with structures out of focus. Further, it is possible to image samples thicker than 2 μm with a high resolution and contrast. [61] Another advantage of CLSM is the possibility to create z-stacks and three-dimensional images. A z-stack is a series of images of one sample at different focus depths. To create such stacks the stage of the microscope is connected with a stepping motor which moves the stage while measuring. As the laser can be focused with high precession the areas which are out of focus can be "blacked-out", such that only a very thin plan of the sample is visualized [33]. The focus plane moves through the sample, taking an image each step. At the end all planes of the sample get merged with special programs obtaining a 3-dimensional image [61]. This method is ideal to visualize microcracks since the three dimensional geometry of the cracks along the sample is of interest.

Fazzalari et al. (1998) used CLSM to classify microdamage in bone in 3 dimensions. Microdamage was en bloc stained with basic fuchsin. They distinguished between microcracks, diffuse damage and cross-hatch and there location in bone (see figure 6). They showed the superiority of CLSM over the two-dimensional analyses, which is reported in previous literature. [33]

4 Methods

4.1 Sample Preparation

The used biological material for this project is trabecular bone from the 2nd phalanx of a 16 month old bull obtained from a local butcher (Fleischerei Hödl, Vienna). The sample preparation, mechanical testing and imaging requires the following steps:

- Dissection of bone
- Cutting trabeculae
- Size measurement of trabeculae
- Embedding of ends
- Fluorescent labelling (Part 1)
- Application of the speckle pattern
- Fatigue testing
- Fluorescent labelling (Part 2)
- Preparation for microscopic analysis
- CLSM Imaging

4.1.1 Dissection of Bone

Bovine bone from the 2nd phalanx is cleaned from soft tissue. The clean bone is then cut into smaller pieces with a bandsaw (Exakt, Germany). The thickness of the bone slices should be around 1-2 mm as this facilitates the successive steps. After cutting the slices the bone marrow is removed via a commercial oral shower, to be able to identify single trabeculae. Figure 12 illustrates a trabecular bone slice before and after bone marrow removal. Since preparation takes around half a day it is recommended to produce as many slices as possible in one session.

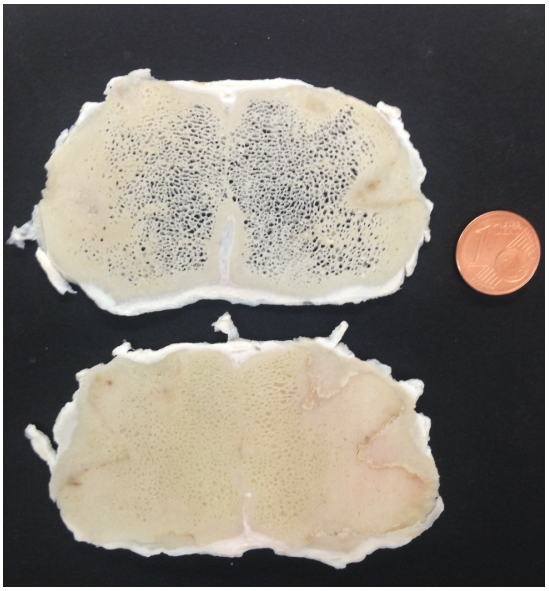

Figure 12: Influence of bone marrow on visibility of trabeculae
top: without bone marrow, bottom: with bone marrow

The cut slices are put into a petri dish with Hank's Buffered Salt Solution[4] with a pH value of 7.4. This is necessary to prevent the samples from drying out in between the preparation steps. However, if the slices or single trabeculae had to be stored for a longer period of time, e.g. over the weekend, then samples had to be wrapped in a cloth soaked with HBSS and stored in the freezer at -18 degrees.

4.1.2 Cutting Trabeculae

In this step the goal is to cut single trabeculae with enough bone mass at each end to enable embedding.

In figure 13 the ideal cutting pattern is marked. The orange arrow points at the desired trabeculae. The red box marks the milling line. As a result, the trabeculae is dissected from neighbouring parts, but still contains enough bone mass for embedding at the top and bottom part.

[4] Hank's Buffered Salt Solution (HBSS) is a buffer, used to maintain pH balance as well as to provide the samples with water and essential inorganic ions.

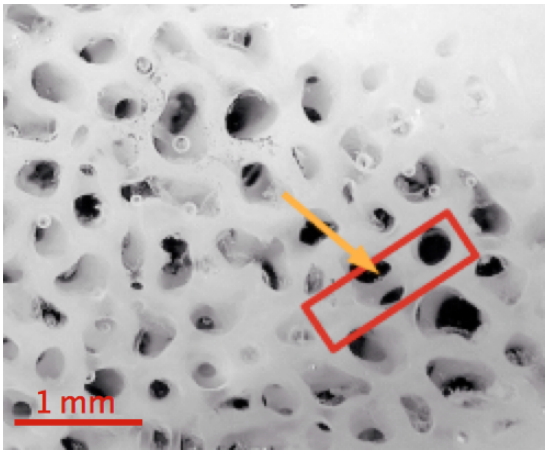

Figure 13: Cutting pattern

A Dremel 400 DIGITAL hand milling tool with a diamond dental drill[5][62] is used to cut out single trabeculae. While milling the bone is soaked in HBSS for the following two reasons. First, bone has to be protected from drying out. Second, the fluid prevents the bone from damage due to the heat arising by milling. During milling the spatial orientation of the trabeculae should be taken into account to make the embedding process easier. This requires some practice and technique which only can be learned over time and gathered experience. The bone slice is fixed with tweezers during milling, for stabilization of the sample. Further, the abrasion is removed by rinsing the sample with HBSS (with a pipette) from time to time. The setup can be seen in figure 14.

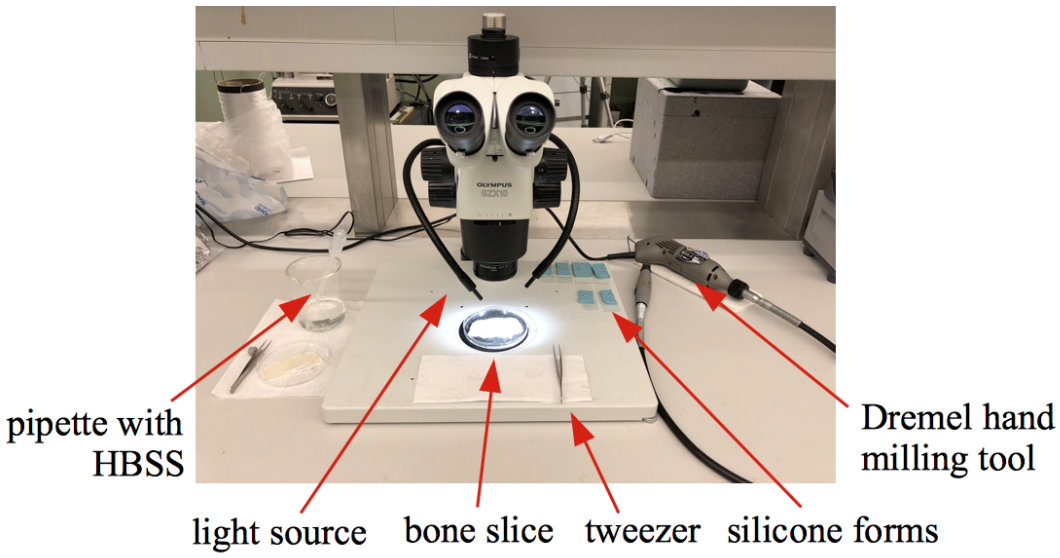

Figure 14: Setup for cutting samples

[5] Dental Drill by MF-Dental / cylinder pointed, ArtNr.: 885-010

4.1.3 Size Measurement of Trabeculae

After milling the geometry of individual trabeculae is measured with a micro computed tomography[6] (Micro CT). Due to long processing time and limited processing resources of the Micro CT not all samples could be measured this way. For this reason each sample was observed with a Zeiss Axio Imager light microscope and the the AxioCam MRc5 and the dimensions were recorded. For validation, the measurements obtained with the microscope were compared with the Micro CT data. It can be seen in table 1 that the deviation between the measurements is in the range of 1%. Sequentially, sample size was evaluated with the light microscope.

Sample		**Length [μm]**	**Width [μm]**	**Hight [μm]**
S1	**Micro CT**	712	150	189
	Microscope	722	160	200
S2	**Micro CT**	694	185	169
	Microscope	700	200	180
8a	**Micro CT**	527	178	208
	Microscope	530	180	210

Table 1: Comparison of measuring methods of sample geometry

4.1.4 Embedding of Ends

For tensile testing the sample has to be fixed in the sample holder of the testing device. Thus, both ends of the sample are embedded in epoxy resin. The embedding is one of the steps during the sample preparation which must be executed with high precision since errors during this step have a huge impact on the actual testing (see section: 4.2.2 Test Execution). A negative of the sample holder was produced with epoxy to manufacture the silicone forms (see figure 15). Silicone[7] with shorehardness of 22 is used, as the forms have to be flexible for embedding [63].

[6] Scanco Medical Micro-CT 100
[7] picodent twinsil® 22

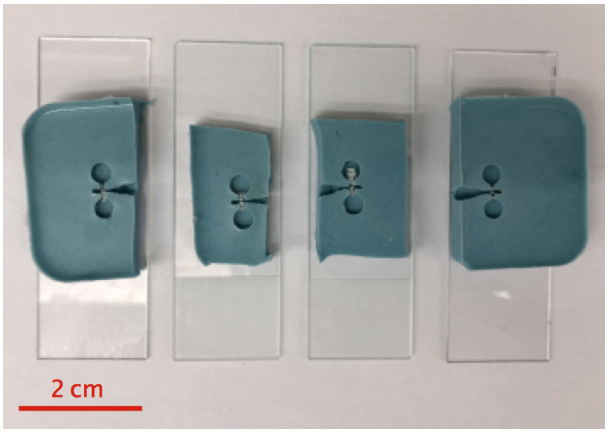

Figure 15: Silicone form with adjusted trabeculae

The trabeculae must be placed in the silicone forms in a way that the trabeculae is in axis and exactly in the correct depth. The notch in the sample holders is 2 mm in depth. The holders are constructed in a way that if the samples are embedded correctly the trabeculae is automatically in axis with the load axis (see template of the sample holders in appendix 9.4). Therefore the cut out bone structure should be embedded in a way that the trabeculae is situated 1 mm from the bottom of the silicone form. The Zeiss Axio Imager light microscope is used to ensure correct positioning of the trabeculae in the z-position. As the microscope stage can be controlled in the z-position, the relative distance between the surface of the trabecuale and the bottom of the form can be measured by focusing on both spots.

The bone remnants at both ends of the trabeculae should be embedded between two epoxy resin glue drops. A "UHU plus Endfest 2-K-Epoxidharzkleber" was used for this purpose. During the project an issue with bad quality of the recorded video of the tensile tests occurred as the contrast was too poor due to reflections. As a consequence the epoxy has been stained with black color[8] in the new protocol to minimize reflections during the measurement process. As such the video quality was easily improved. Another improvement, which was made during the project, was to put the epoxy in the vacuum desiccator for about 1 minute before using it for embedding. This procedure removes air from the epoxy and improves it's rigidity.

After applying the epoxy resin in the silicone forms the alignment of the trabeculae can be checked again with the Zeiss Axio Imager light microscope since sometimes the trabeculae moves unknowingly through slight movements during the epoxy application. It should also be checked that the epoxy covers enough bone mass at the ends while still not getting

[8] universal color paste in deep black (RAL 9005)

in touch with the actual trabeculae. This is essential since this would influence the results of the performed tensile test. Thus, this region is protected with plasticine (see figure 16).

The glue takes 12 hours (according to the manufacturer's specification) to dry out completely without any significant shrinking [64]. During the project it was noted that 16 hours for drying were more effective. Since during these 16 hours the samples are drying it is necessary to hydrate the samples again afterwards as soon as possible.

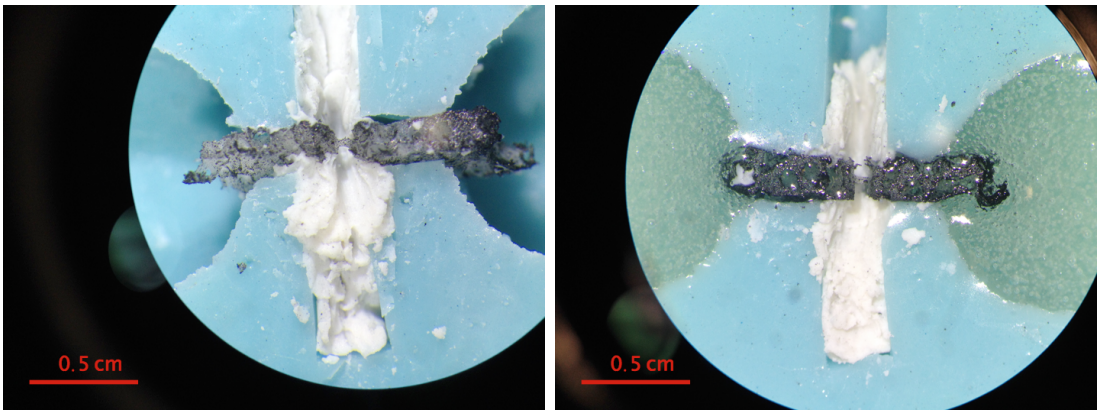

(a) Samples got protected by plasteline to avoid epoxy on the trabeculae

(b) Epoxy application

Figure 16: Embedding of samples

After 16 hours of drying at room temperature the samples are taken out of the forms. It is important to ensure that the samples are not bent or deformed during this step. Remnants of the plasteline should not remain on the bone and must be removed very carefully.

It must be noted that the silicone forms loose their ideal shape after using them for more than 3 times. Therefore, they have to be replaced regularly.

4.1.5 Fluorescent Labelling

For this project the fluorescent labelling protocol of O'Brien et al. (2002) was used and ideas for adaptation were taken from Green J. et all. (2011) (see section: 3.2 Labelling of Microdamage).

The used chelating agents are:

- Alizarin Red S[9] (A) [65]
- Calcein Blue[10] (CB) [66]
- Xylenol Orange[11] (X) [67]
- Calcein[12] (C) [68]

The solutions of the chelating agents are produced after the following protocol:

Alizarin Red S: 5 x 10^{-4} M
Molecular weight: 342.26 g/mol
0.1711 g of the powder is weight out to 1 liter distilled water.

Xylenol Orange: 5 x 10^{-4} M
Molecular weight: 716.62 g/mol
0.3584 g of the powder is weight out to 1 liter distilled water.

Calcein: 5 x 10^{-4} M
Molecular weight: 622.53 g/mol
Solubility: 50 mg/mL, 1 M NaOH
0.312 g of the powder is weight out to 1 liter distilled water.

Calcein Blue: 5 x 10^{-4} M
Molecular weight: 321.28 g/mol
Solubility: 50 mg/mL, 1 M NaOH
0.1606 g of the powder is weight out to 1 liter distilled water.

The solution of powder and distilled water is put on a magnetic stirrer for 15 minutes to dissolve properly. The mixed solutions and the powder are stored in glass bottles in the fridge wrapped in tinfoil.

The chelating agents were tested at the beginning of the project to explore their staining capabilities. First each chelating agent was tested on its own and afterwards the sequential labelling was tested. Everyone except Calcein Blue (CB) did work fine. CB tested alone was not as bright as the other fluorochromes and in sequential labelling it did not appear at all (see 4.1.5 Calcein Blue Test).

[9] Sigma-Aldrich, Saint Louis, MO, USA, Product number: A5533
[10] Sigma-Aldrich, Saint Louis, MO, USA, Product number: M1255
[11] Sigma-Aldrich, Saint Louis, MO, USA, Product number: 52097
[12] Sigma-Aldrich, Saint Louis, MO, USA, Product number: C0875

Also the reaction time of 4 hours in the vacuum desiccator was compared to 8 hours at 4 degree Celsius. In both conditions the fluorochromes bound adequate to the bone matrix. To spare time the first method was further used.

The basic idea was to stain the samples before mechanical testing, and once or twice during testing to visualize the appearance of microdamage and one final time after testing to show the progression of microdamage. During the progress of the project it was noticed that with the used test set-up it is not possible to stain the samples during testing. Therefore it was decided to stain the samples twice. First, before testing with 5 x 10^{-4} M Alizarin Red S to visualize pre-existing damages and second, after testing with 5 x 10^{-4} M Calcein to stain generated microdamage.
For the staining process itself the samples are put into a Petri dish or another small cup which is filled with the chelating agent. The Petri dish is covered with tinfoil and put into the vacuum desiccator for 4 hours. Afterwards samples are washed 3 times with distilled water. For further steps the samples have to be stored in HBSS again since distilled water might resolve bone minerals and this would have a negative impact on the accuracy of this project.

Calcein Blue Test

Staining with CB did not work properly with the mixing ratio postulated by O'Brien et al. (2002). Therefore different ratios were tested to find the best fitting one. O'Brien recommend a 1 x 10^{-4} M solution. For every other chelating agents the ratio is 5 x 10^{-4} M [60]. So a higher concentration was tested. Also the solubility of the fluorochrome powder was an issue for Calcein Blue. After 15 minutes on the magnet stirrer the powder did not dissolve properly. In the product specification sheets of the chelating agent it was mentioned that it is soluble in 1 M sodium hydroxide (NaOH). However, O'Brien et al. (2002) did not mention using NaOH. As NaOH and water change to a strong alkaline solution which can harm bone it was not preferred to use as much NaOH as mentioned in the specification sheet. With this in mind, four different CB solutions got tested on cortical bovine bone of a 16 month old bull in which a line was scratched with a scalpel :

- 1 x 10^{-4} M Calcein Blue without NaOH
- 1 x 10^{-4} M Calcein Blue with 0.2 g NaOH
- 5 x 10^{-4} M Calcein Blue without NaOH
- 5 x 10^{-4} M Calcein Blue with 0.2 g NaOH

As noticeable in the following figures (17, 18) the fluorochomes are much brighter in the samples which got labelled with solutions containing NaOH. Moreover, the higher concentrated solution without NaOH showed an intenser labelling of cracks.

After comparing the images it was decided to use the 5 x 10^{-4} M solution without NaOH. The fluorochomes did indeed bind better to the bone matrix when mixed with NaOH but as it is not foreseeable what impact NaOH would have on the samples it is more desirable to avoid its use.

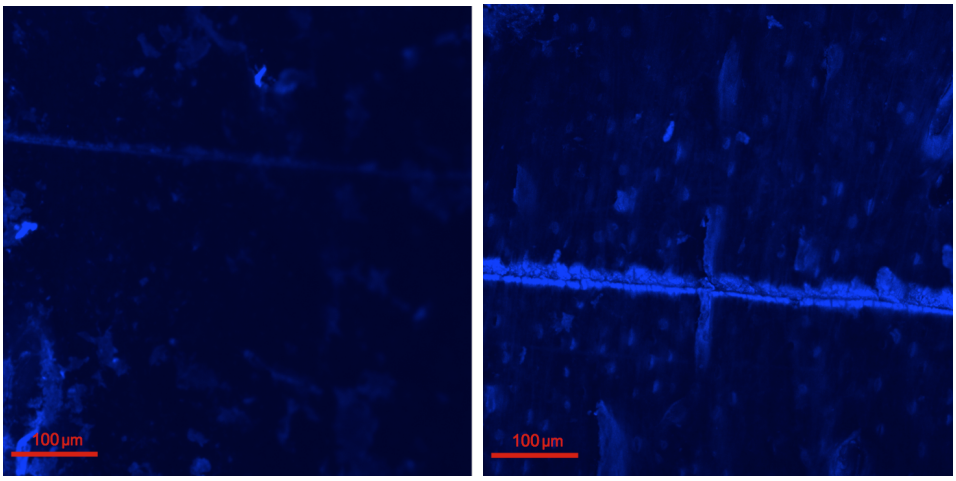

(a) without NaOH (b) with NaOH

Figure 17: 1 x 10^{-4} M Calcein Blue

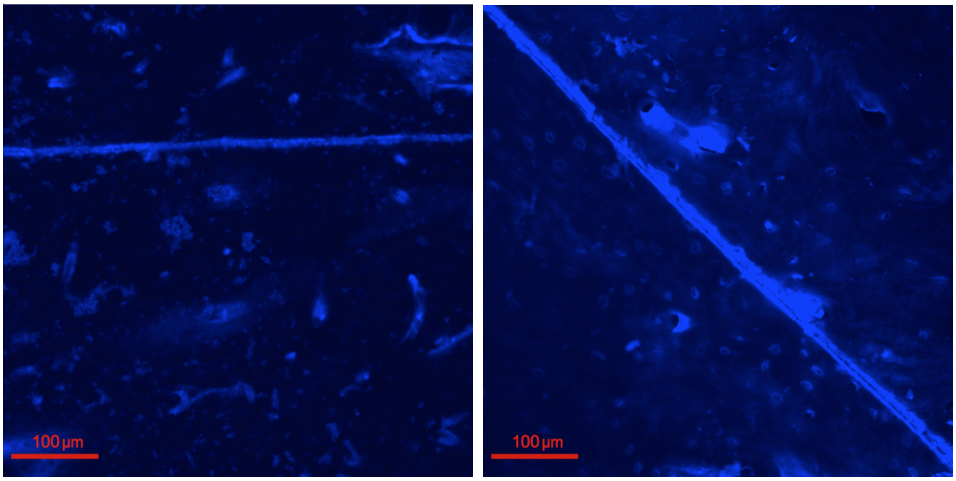

(a) without NaOH (b) with NaOH

Figure 18: 5 x 10^{-4} M Calcein Blue

4.1.6 Application of the Speckle Pattern

The strain measurement was performed with an optical system. The deformation is recorded with a camera during the tensile test. Thus, a speckle pattern has to be applied onto the sample surface to analyze length changes [69].

The pattern consists of many small dots spread over the whole sample. The dots should be as small as possible and the distribution of them should be homogeneous over the whole sample. To achieve this kind of pattern the samples are not sprayed directly, but from the side instead, such that only the scattered small particles reach the probe surface.

Four sprays were compared for this step:

1. Dupli-Color Aqua High Quality Lackspray black [70]
2. Graphit 33 Spray from CRC Industries [71]
3. Dupli-Color Lackspray Aerosol-Art RAL 9010 Reinweiß matt [70]
4. Dupli-Color Lackspray Aerosol-Art Chrom-Effekt [70]

All sprays are soluble by water, but the one based on graphit has a much higher solubility. In previous studies the best results were achieved with the Graphit 33 Spray from CRC Industries as the gained dots are really fine and the whole pattern can be removed after testing to see the bone structure again [71].

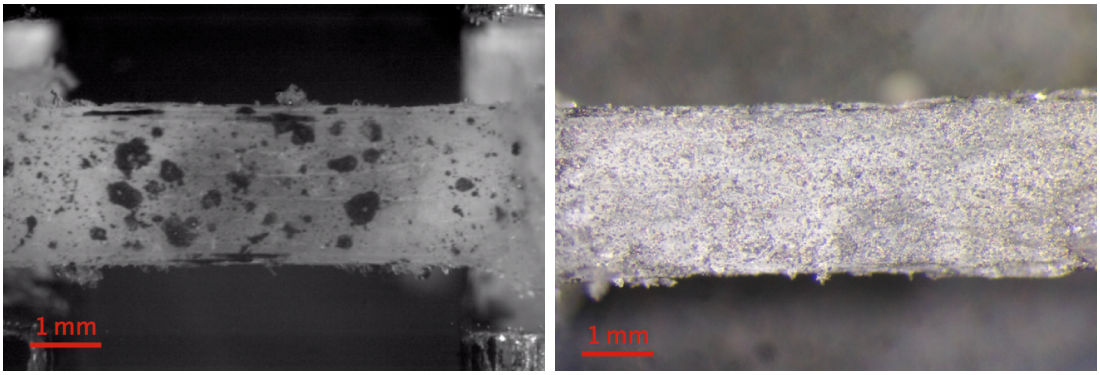

(a) Dupli-Color Aqua High Quality Lackspray [70] (b) Graphit 33 Spray from CRC Industries [71]

Figure 19: Comparison of spray 1 and 2
These images were taken during a previous project at ILSB. Spray 1 and 2 are tested on cortical bovine bone. With Spray 2 a finer speckle pattern can be achieved but due to its high solubility in water it is not practicable for this project.

But as the samples in this study are tested for several hours the speckle pattern vanished after some time due to the high solubility in water of the graphit spray. Therefore the Dupli-Color Aqua High Quality Lackspray from Motip Dupli [70] was used for further tests. The dots gained are slightly bigger but the quality is good enough to gain values for the strain determination (see figure 19). Also different spray heads ([72]) were tried out to change the dot size. It turned out that the best results can be gained with the standard spray head.

During the project another issue occurred concerning the contrast between the color of the spray and the bone. As the samples got stained with Alizarin Red S the bone color changed from white to purple resulting in a reduced contrast to the dots for strain tracking (see figure 20a). Therefore different colors of the Dupli-Color spray (chrom and white matt) were tested. The chrom spray performed poorly but the white spray achieved good results.

Good results of the speckle pattern, as displayed in figure 20b, are obtained by spraying 4 times for 3 seconds with a 2 minute break between each round to give the particles time to settle. It must be noted that with this method the result varies substantially across operators because of manually operated steps like pushing the spray button or the angle of spraying. These factors can make quite a difference in the end result.

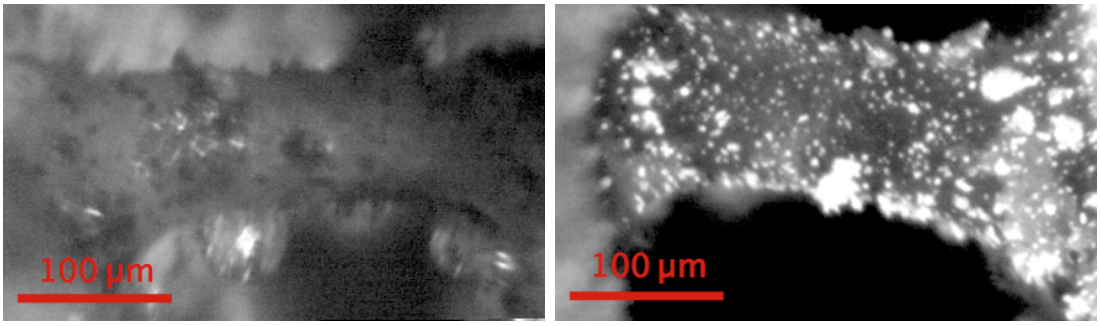

(a) Dupli-Color Aqua High Quality Lackspray [70]

(b) Dupli-Color Lackspray Aerosol-Art RAL 9010

Figure 20: Comparison of spray 1 and 4

There was also an attempt to see the whitening effect[13] during testing as indicator for induced microdamage. Therefore, a small region in the middle of trabeculae (where the damages are expected) was masked to protect it from the speckle pattern (see figure 21.

[13] Whitening is an effect which occurs due to reflection of incident light at an accumulation of microscopic cracks [73]. It is possible to detect the begin of plastic deformations in bones through this effect [74].

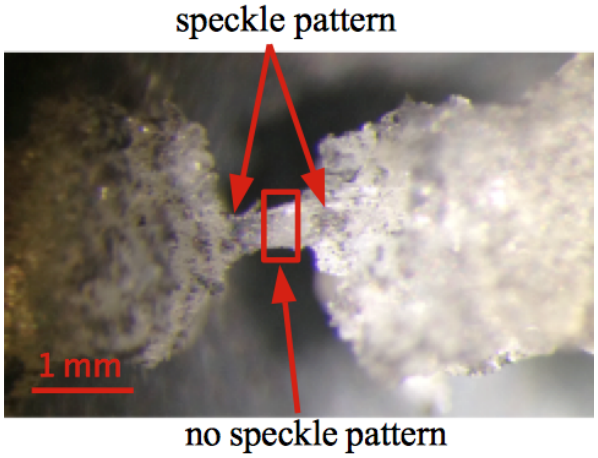

Figure 21: Schematic display of speckle pattern application
Note: The sample taken here for illustration of the pattern is not stained yet. Therefore black spay is used.

The step of applying the speckle pattern was not carried out through the whole project as in the end there was no need to determine the strain on the samples anymore (see section: 6 Results).

4.2 Mechanical Testing

The samples to be investigated were to be tested under fatigue loading with a sinusoidal profile. A detailed description of the test design can be found in section 5: Fatigue Test Design.

4.2.1 Setup and Modifications

Tests were performed with a servo-electric load frame SEL mini-001, Thelkin (see figure 22) [75]. The system includes a load unit with a cross-head-mounted actuator and a test controller with the channels of control for force and displacement in axial direction. To reach the goal of this thesis the displacement control was used as this effected higher stability compared to force-control.

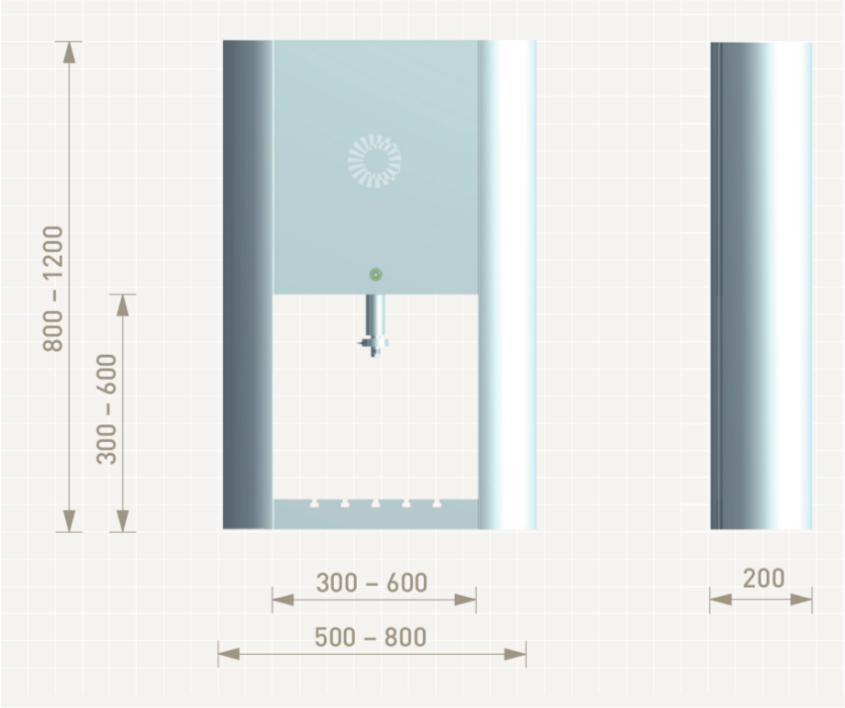

Figure 22: SEL mini-001servo-electric load frame with dimensions in mm [75]

The following table 2 shows the basic information about the SEL mini-001 load frame:

Specification	**SEL**
Nominal Force [N]	+/- 50 /+/- 100
Frequency [Hz]	50
Travel [mm]	+/- 25
Travel resolution [μm]	0.2
T-slot dimension	10
Working area [N]	+/- 100
Resolution [%]	+/- 0.1

Table 2: SEL mini-001 specifications [75]

To perform the tension tests on the prepared samples some improvements of the device were made. As such, two security stops are added to the SEL mini-001 device to prevent the loading cell (10 N) from damage. For example, through an erroneous triggering, like a limit overshoot or an overload can happen and the loading cell would drop down. Such erroneous triggers can appear through wrongly set parameters.

To fix the upper part of the sample to the mechanical testing device a sample holder is mounted via a grub screw to the load cell. The bottom part of the sample holder is placed in a water bath to enable tests in HBSS. The sample holders were redesigned and

replaced during this project. The initially used sample holders were designed by Dorothee Marx during her master thesis [73]. These holders are able to rotate perpendicular to the load axis. This was an attempt to enable a self adjustment of the samples. For cortical samples this was a suitable solution. But it turned out that it is more preferable to have the fixated sample holders for trabecular samples. Further, the new sample holders contained flaps over the notches for the samples to prevent a forwards tilt of the samples prior to applying the preload (see figure 23). Additionally, the new holders were anodized to black matt color to reduce reflections during video recordings.

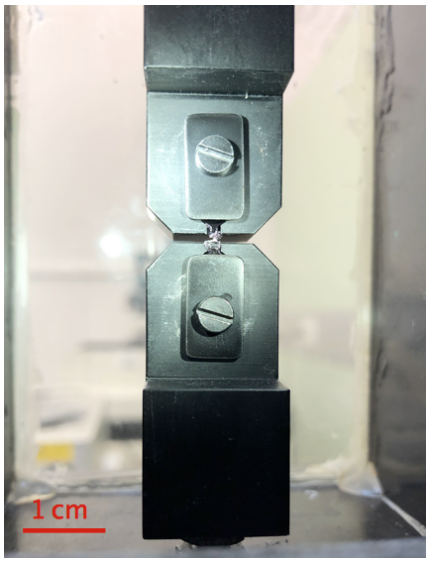

Figure 23: Re-designed sample holders

The improved sample holders made the measurement more precise as a forwards tilt was prevented and therefore, the gained measurement values scatter less. But to gain this result it is also requires to avoid any inaccuracies in the embedding and adjusting of the sample in the holders as the samples have to be exactly in line with the loading axis.
The water bath is anchored in t-slots in the base plate of the load frame. It is necessary to position the lower sample holder exactly under the upper one and parallel to the load frame front. The water bath was also designed in a previous project and got extended by an additional base plate [73]. Before adding this new base plate the sample holder itself was anchored in the t-slots. Therefore it had to be orientated every time the set-up was changed between different users and the adjustment took a considerable amount of time. With the additional base plate and the new sample holders the time for this step could be reduced from 1 hour to 10 minutes. Figure 24 illustrates the whole test set-up, marking all important components.

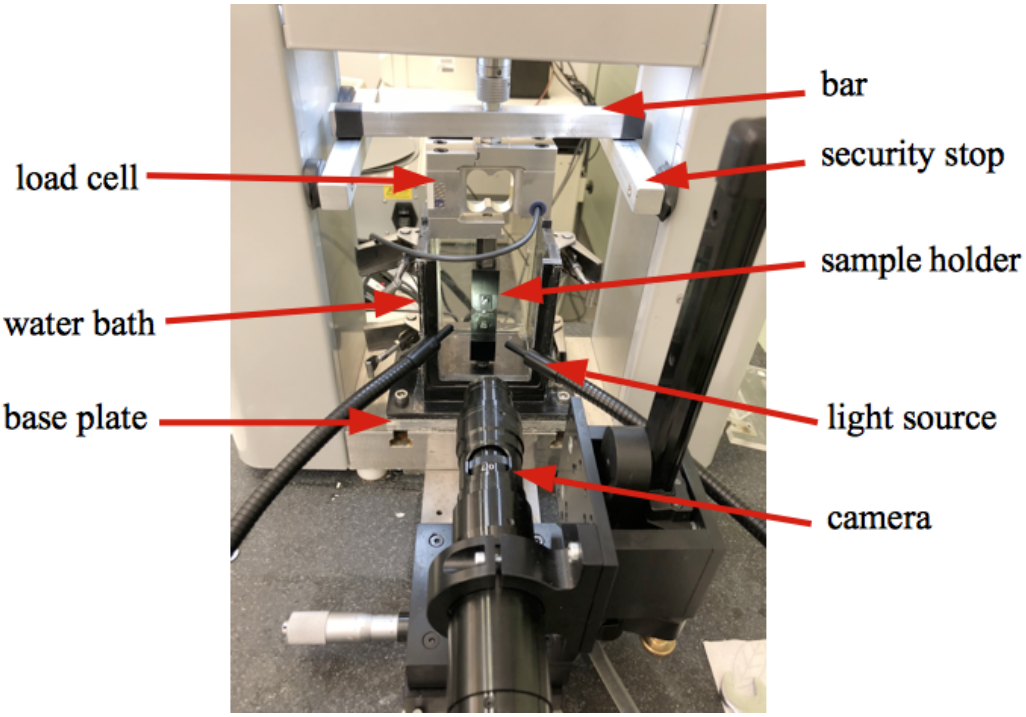

Figure 24: Test setup

For strain measurement and recording of sample movement a camera (UI-3250CP-M-GL, IDS GmbH) is used. A cold light source is used to illuminate the sample, which works with discrete current (DC) to reduce brightness variations (on the order of 50 Hz for AC current).

For the fatigue test a sinusoidal profile is used (see figure 25).

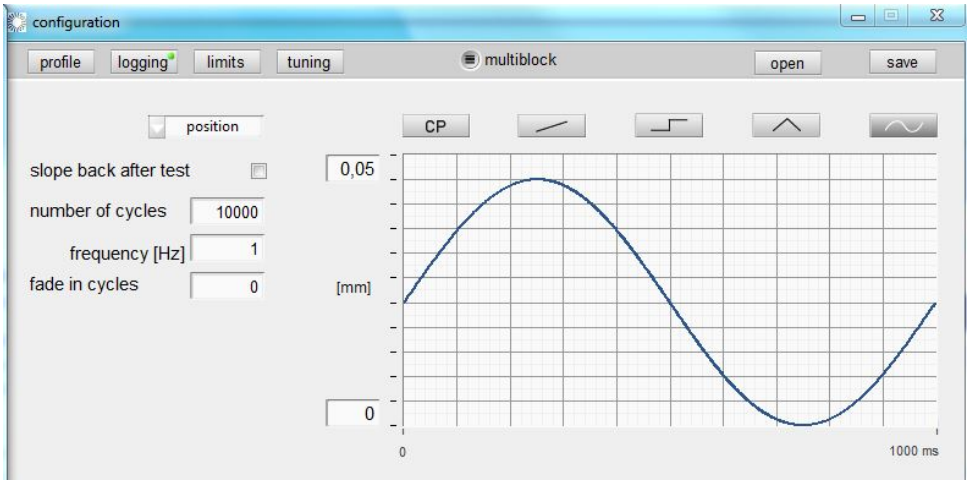

Figure 25: Sinusoidal profile for fatigue testing at 1 Hz with an amplitude of 25 μm.

The settings shown in table 3 were used initially:

Specification	**Value**
Channel of control	position
Frequency [Hz]	10
Number Of Blocks	1
Offset	0
Min./Max. Load [N]	-10/+10
Min./Max. Position [mm]	-3/+3
Tuning Kpp	0.6
Tuning Kpv	1
Tuning Tiv [ms]	30

Table 3: Test specifications

As can be seen in figure 25a the initial values for the 3 control engineering settings (Tuning Kpp[14], Kpv[15] and Tiv[16] used for previous tests (shown in table 3) do not fit for the sinusoidal profile. The dark blue line shows the default profile and the light blue line the way the SEL mini-001 actual covers.

Therefore these settings were changed to the ones shown in the following table 4:

Specification	**Value**
Tuning Kpp	1.5
Tuning Kpv	1.5
Tuning Tiv [ms]	12

Table 4: New control engineering settings

In figure 26b the improved profile with the new control engineering settings is shown. There is still an offset between actual and desired profile (see figures 26). But no better results could be achieved by further variation of Kpp, Kpv and Tiv and in the analysed data of tested samples it was proven that the samples were loaded in a sinusoidal manner.

[14] Kpp = proportionality gain of position contoller
[15] Kpv=proportionality gain of velocity controller
[16] Tiv = integration time of velocity control loop

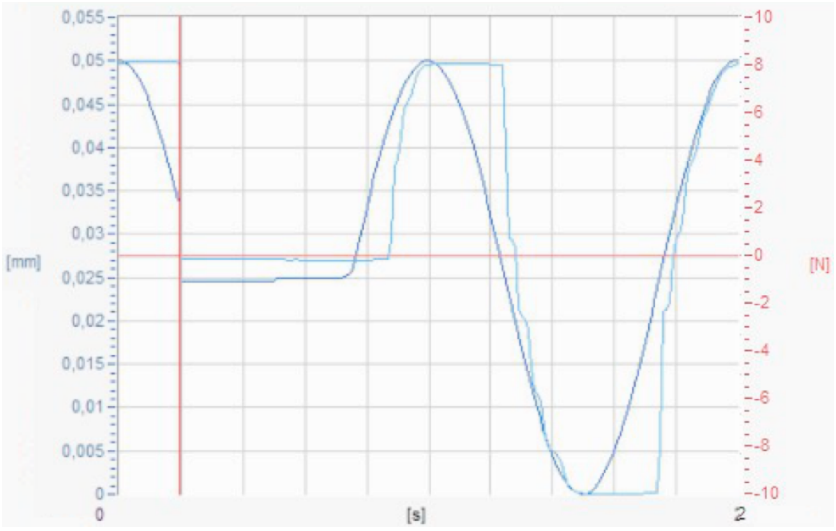

(a) Profile with original settings

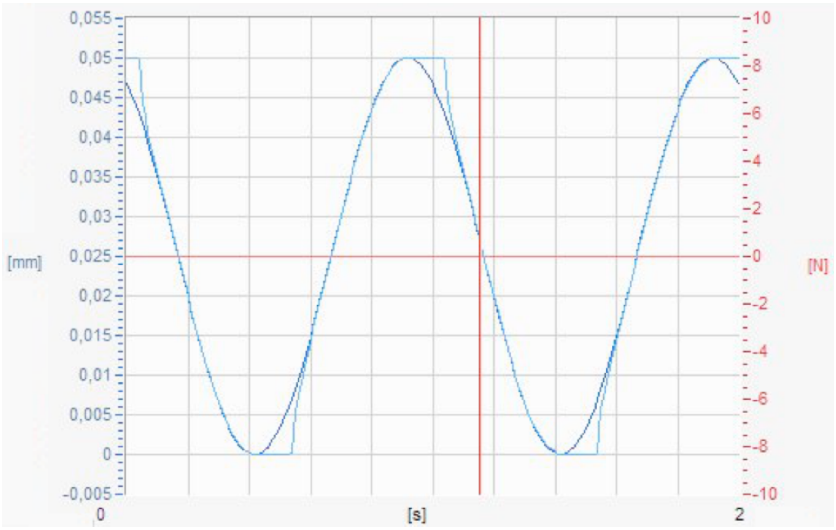

(b) Profile with adapted settings

Figure 26: Original and adapted profile
These curves (input in dark blue, output in light blue) show the difference between original figure 26a and adapted control engineering settings figure 26b. It is visible that the offset between desired and actual profile is much smaller in figure 26b.

In figure 27 the first circle of the profile is shown. This miss-loading during the very first cycle could not be resolved but no noticeable impact on the testing was recognised. However, it is mentioned here for the sake of completeness.

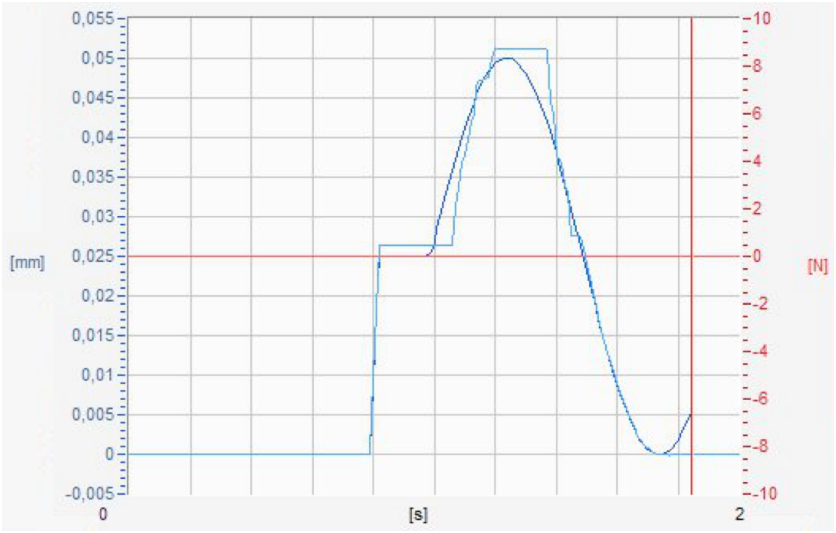

Figure 27: Offset at test start

4.2.2 Test Execution

The SEL mini-001 machine is switched on and the software is started. During the use of the device it turned out that there is a high possibility of failing during the first two measurements, which could lead to a damage of the load cell. For this reason it is advised to perform the first two measurements without the load cell.
For adjustment of the set-up a sample made out of epoxy resin is used. The camera is set in the correct position and to the highest magnification. The control and camera read out (μEye Cockpit) is started in monochrome mode. The setting "Calc Frame" is set to 10 and the JPEG Quality to 100. The profile which was used for the epoxy resin sample is linear. The test and camera record is started. After 5 N are reached the test is stopped. Then, the recorded video is watched to check if there are any shifts of the sample normal to the movement direction. If so the set-up must be newly orientated. This step must be repeated until there are no shifts visible.

Before testing, samples have to be hydrated for at least 2 hours. Then, the first sample is put into the sample holder, the water bath is closed and filled with room tempered HBSS. The profile is changed from the linear to the sinusoidal profile (see figure 25) and it is checked if the SEL mini-001 settings are correct (as described in section: 4.2.1 Setup and Modifications). Then, the pre-load is applied and the first cycle set can be started. This is repeated till the total intended amount of cycles is reached. For each measurement a video and a data file with the position/load information is gained[17]. The videos are used

[17] As side-note it should be mentioned that during this project it was also tried to record the video and SEL mini-001 data with a higher frame rate. Nevertheless the interface between the camera

to check the behaviour of the sample during testing and to determine the strains of the trabeculae. At first a video sequence was recorded for every set. However, a considerable amount of video data was gained, requiring lots of disk space (e.g. one video in size of a few GB). Also the video buffer of the camera is limited to 4 GB. Therefore, the procedure was changed to only record one video at the beginning, one during the middle of the test and one during the last cycle set.

To change the samples it is advised to empty the water chamber and open it as this makes the process easier and the probability of damaging the sample is reduced.
After each measurement session the chamber should be cleaned. It is recommended to wash the bath with distilled water to avoid algal formation.

4.3 CLSM Imaging

4.3.1 Preparation Steps for CLSM Imaging

To analyse the samples with the CLSM (3.3) some preparations are necessary.
First of all the samples have to be stained for the second time, to visualize test induced microdamage. The chelating agent Calcein is applied for 4 hours in the vacuum desiccator (see section: 4.1.5 Fluorescent Labelling). The samples were analysed with 10x, 20x and 100x magnification. As the 100x objective is an oil immersed one it is necessary to minimize the distance between trabeculae and objective and also to embed the samples. In the first attempt the samples were cut free from the epoxy droplets at each end to set the trabecula free. In this way the distance to the objective could be reduced since the epoxy droplets are around 1 mm higher than the actual trabeculae. The cut-free trabeculae then were fixed with super-glue to an object slide. But it was observed that the surface of the trabecula is too rough to gain images with sufficient quality. The surface scattered the light of the CLSM to a large extent such that damage visualisation was not feasible. Additionally, the risk of damaging the trabeculae during cutting off the droplets was high.

Therefore, the following procedure was developed in which the surface of the trabeculae could be levelled and polished.
The whole sample is embedded and fixed with epoxy resin glue (UHU plus Endfest 2-K-Epoxidharzkleber) to an object slide as shown in figure 28.

and the program μEye Cockpit had some issues which could not be solved during this project - even with help of the Thelkin support team. A frame drop occurred as soon as the frame rate was set higher than 10 Hz.

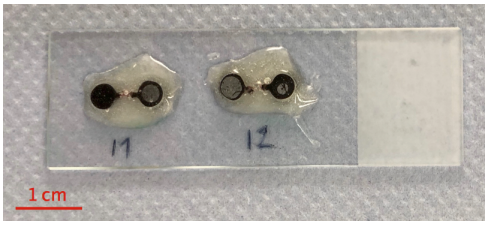

Figure 28: Samples fixed with epoxy resin to an object slide

After drying for 16 hours the samples can be fixed on the ultramiller (Leica SP2600 [76]). The following settings in table 5are used for milling the redundant epoxy resin:

Specification	**Value**
Feed (Premiller) [μm]	4
Feed (Finishing miller) [μm]	1-2
Retract [n]	50
Cut [mm/s]	1-2
Return [mm/s]	40
Speed [rpm]	1200

Table 5: Leica Ultramilling settings

The premiller is used to remove the first few millimetres until the trabeculae are visible. This has to be checked under the microscope. After reaching the trabeculae the premiller can be changed to the finishing miller. From this point on after every 5 μm of depth abrasion the sample is checked under the microscope to see, if microdamage is already visible. The Zeiss Axio Imager light microscope is used with the filter for Alexa Four 488 which induces Calcein fluorescence. This procedure works well for the first check of microdamage creation. However, for images with good resolution and to generate z-stacks the CLSM is needed. After stopping of milling the finishing miller is cleaned with acetone.

Investigation of the samples under the light microscope showed parallel grooves as shown in figure 29a. The expected image should be free of such grooves as the finishing miller is a very precise tool. Changes in the settings of the ultramiller (speed, feed) were made but no improvement could be reached. Another idea was to clean the surface with acetone to check if the epoxy was too soft as it smudged during milling. But as it can be seen in figure 29b this also made no difference.

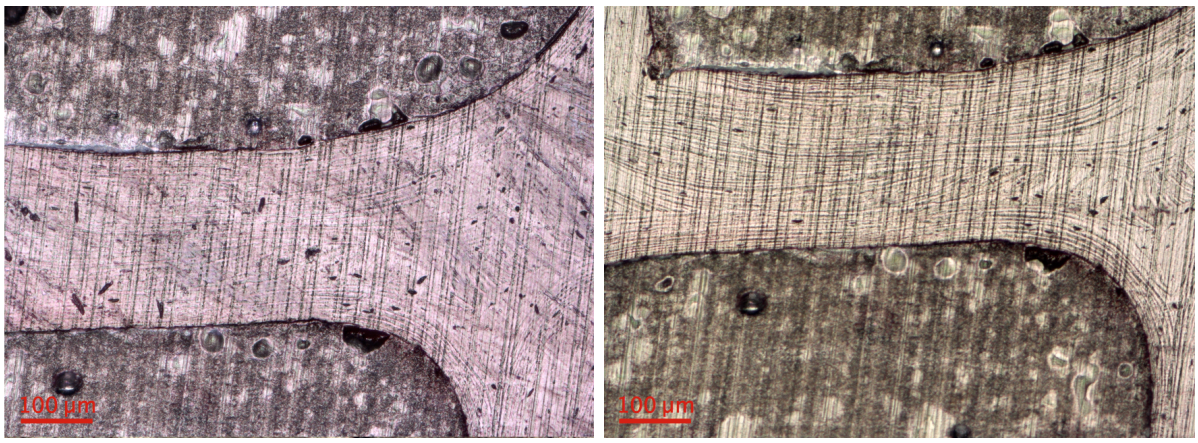

(a) Sample after finishing miller (b) Sample after cleaning with acetone

Figure 29: Grooves in sample after ultramilling

The samples were analysed with the CLSM but the surface still scattered significantly the light as can be seen in figure 32a. Therefore, the samples were polished by hand after milling (see figure 30). This protocol is already established for cortical bone. The first polishing steps are performed with sandpaper of different grits (1000 and 2400). With each particle size the sample was ground for 3 minutes. After finishing with one sandpaper the sample is cleaned with distilled water to remove residues of the grit. This avoids larger particles of the predecessor to still be present in the following step.
The next steps of the polishing process are performed with Buehler MetaDi monocrystalline diamond suspensions of 3 μm, 1 μm and 0.25 μm with textile polishing cloths. Every sample is polished for 3 minutes with each particle size. Between the different suspensions the samples were cleaned in a Sonorex Super ultrasonic bath for 3 minutes.

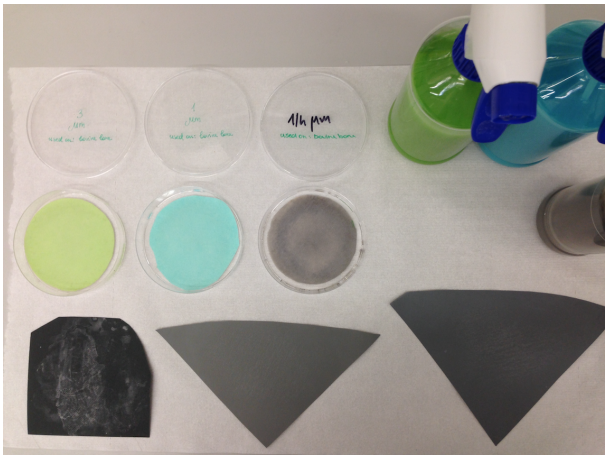

Figure 30: Steps of bone polishing
Polishing equipment: Diamond suspensions with textile polishing cloths (3 μm, 1 μm and 0.25 μm (from left to right)) and sandpaper in grits of 1000 and 2400 (from left to right).

As it can be seen in figure 31 a significant improvement of the surface quality can be reached with this procedure.

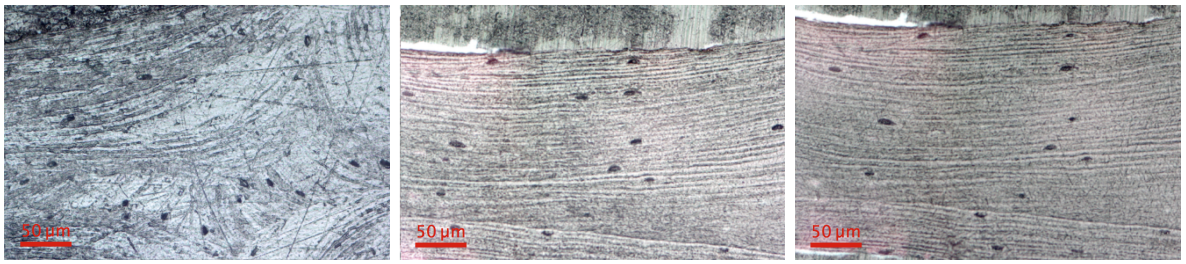

(a) 3 μm diamond suspension (b) 1 μm diamond suspension (c) 0.25 μm diamond suspension

Figure 31: Surface quality after polishing with diamond suspensions (20x magnification)

The improvement of the CLSM image quality gained from this step can be seen in figure 32b. The labelled damage is clearly visible and no disturbing scattered fluorescent light is detected.

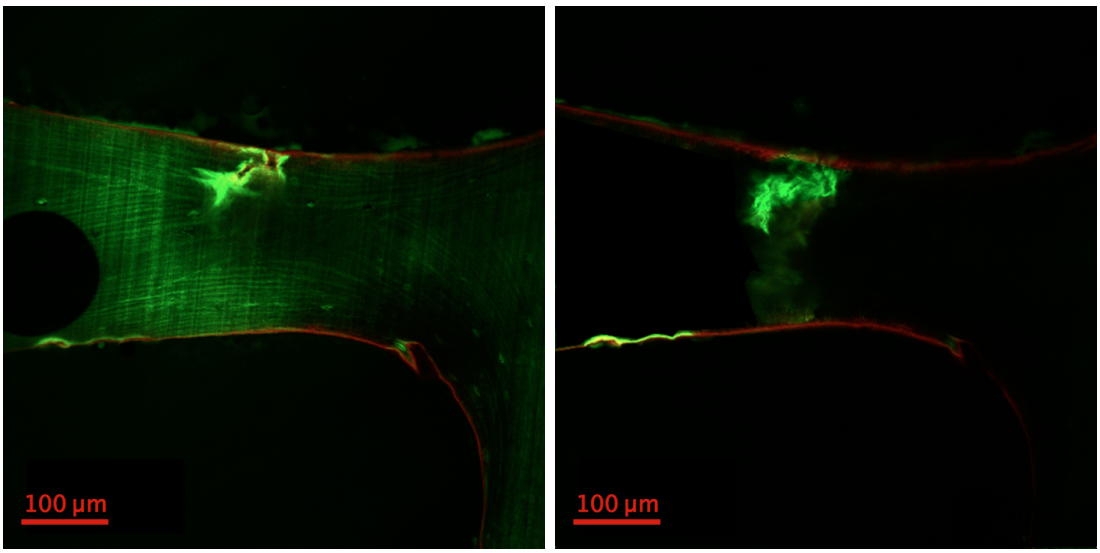

(a) Sample before polishing (b) Sample after polishing

Figure 32: Sample images with CLSM with 20x magnification before and after polishing

4.3.2 CLSM Analysis

A Zeiss Axiolab microscope was used with a laser and the Zeiss ZEN Black software. The samples were analysed with 10x and 20x magnification to get an overview about the microcracks and the orientation of the sample. The 100x objective was used to analyse the microcracks in more detail and to distinguish damage and cracks from lacunae and other micro-structures of bone. The 100x objective is oil immersed and therefore the samples need to be covered by a coverslip[18] to protect them from oil. Therefore, a mounting medium[19] was used. A tiny drop was put onto the sample and a piece of the cover slip was put onto it. Clear nail polish was used for fixation of the cover slip .

[18] Roth 18x18mm Art Nr. 0657 are used and broken into smaller pieces as the samples were much smaller

[19] Sigma-Aldrich Fluoromount^{TM} Aqueous Mounting Medium

The following objectives and settings in table 6 were used for CLSM image acquisition:

10x objective	EC Plan-Neofluar 10x/0.30 M27
20x objective	EC Plan-Neofluar 20x/0.50 M27 objective
100x objective	Plan-Apochromat 100x/1.40 Oil objective
Scan Mode	Stack
Zoom	0.5-1
Pixel dwell	1.27 μm
Laser 1	555 nm
Intensity Laser 1	800%
Laser 2	488 nm
Intensity Laser 2	800%
Filter Ch1	BP 420-550
Filter Ch2	LP 560
Pinhole	70 μm
Digital gain	1

Table 6: CLSM Settings

The images were taken with 80% laser intensity and a pinhole of 70 μm. For some samples the laser power was changed in the range from 70-100%. For every sample a z-stack scan was executed.

4.4 Data Analysis

4.4.1 Mechanical Data Analysis

The goal was to check if a decrease in the elastic modulus can be detected in order to establish a stop criterion for the mechanical fatigue test.
For continious tests of trabeculae the analysis already exists. The used scripts got adapted to fatigue tests. For analysis of the data a Python script established by Martin Frank (ILSB) is used. The video analysis is done with the software ImageJ[20][77] and the PlugIn StackReg provided by the ILSB. The video is converted into an image sequence and possible rigid body translation is eliminated by the PlugIn. Then, the first picture and last picture according to the video material are chosen to check valid particle tracking. As shown in figure 33 pairs of dots were selected in the top and the bottom region of the trabecula. Using the recorded videos, the distance between these pairs was computed in the first frame and the average is determined as mean initial length l_0. The lines in the top and bottom region represent the average position of the particles in the upper and lower

[20] ImageJ is an open source Java image processing program

region of the trabecula. Sequentially, this point tracking was performed in all frames to determine the movements of the dots. Through the used point tracking algorithm (trackpy v.0.3.2, [78]) the trajectories of individual particles through the image sequence were determined. This movement caused an elongation of the trabecula and a length change Δl can be defined.

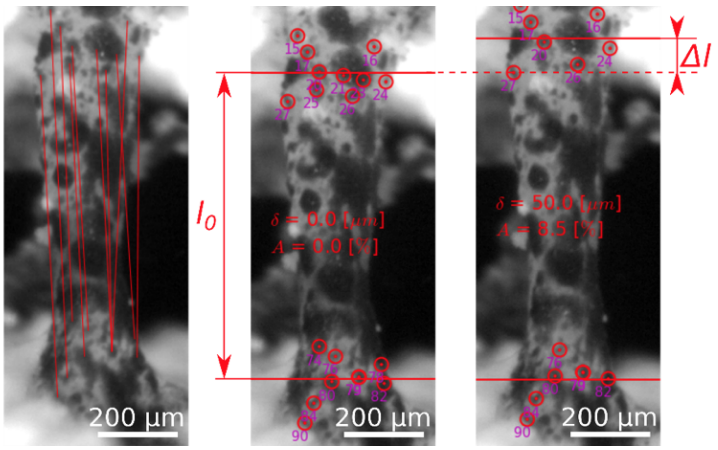

Figure 33: Determination of deformation with digital image correlation
Left: Length between vertical pairs of dots in first frame / Middle: Frame at preload with initial average length l_0 / Left: Frame at fracture, illustrating the change in length Δl

This algorithm uses subpixel resolution, since the centroid of each point is used for tracking. According to Savin et al. (2005) the median uncertainty in particle location was 0.40 μm [79].

The change in length Δl of corresponding vertical pairs of dots was calculated and averaged to determine the mean change in length over time. Since wet samples were tested and these especially exhibit considerably large strains true stress-strain behaviour was evaluated. True strain was calculated [80].

$$\varepsilon_T = \ln(1+\varepsilon_E)$$

$$\text{with } \varepsilon_E = \Delta l \ / \ l_0$$

Load and displacement signals were manually synchronized.

For force and stress determination the size of the individual trabeculae has to be determined (see section: 4.1.3 Size Measurement of Trabeculae). Ture stress was calculated according to [80].

$$\sigma_T = \sigma_E * \ln(1+\varepsilon_E)$$

$$\text{with } \sigma_E = F_{exp} \,/\, \mathrm{A}_{median}$$

F_{exp} is the recorded force from the load cell and A_{median} the cross-sectional area of the trabecula in longitudinal direction.

In the linear region, the constitutive behaviour is given by Hooke's law:

$$\sigma_T = \mathrm{E} * \varepsilon_E$$

E is representing the elastic modulus, which is calculated from the slope of a linear regression [81]. The R^2 value was evaluated as a function of the used data. Increasing the data window (e.g. number of used frames in the linear region), results in a larger R^2 value. Increasing the number of used frames in the non-linear region results in a lower R^2 value. The yield point was therefore determined by the index of the frame showing the maximum R^2 value. This time point is then used to determine yield stress and strain (σ_y, ε_y).

The analysis is executed twice for one sample. One time at a set of data at the beginning of the test (around cycles 0-100) and one time for a set at the end (for example 2500-3000).
After analysing 10 samples in which microdamage could be detected and no decrease in the elastic modulus could be seen this analysing step was not further performed. The detailed results can be seen in section 5.2 Stop criterion and appendix 9.3.1.

4.4.2 Image Data Analysis

For analysing microdamage the software ImageJ[21][77] was used. Z-stacks of every sample are available and therefore, a volumetric analysis is possible. The results about mechanical tests with microdamage evaluation of trabecular bone in the literature is mostly reported in 2D. Since it was desired to compare the results obtained with the literature a 2D analysis were also realised. Images that were taken at 20x magnification were used for the analysis. Part of the analysis was to categorize the images with respect to microdamage. Therefore, the z-stacks are manually processed for 3D analysis and the number of linear cracks per sample is counted. For 2D two representative slices were taken out of the z-stack. Linear cracks and diffuse damage were recognised during this project.

[21] ImageJ is an open source Java image processing program

3-Dimensional Analysis

The z-stacks were imported into ImageJ and converted into grayscale[22]. Since 3 channels (red, green, blue) are imported the images have to be split[23]. As the green channel represents all microcracks (see section: 6 Results) only this one is of interest and all others can be closed. Using the polygon selection tool the region of interest (ROI) is determined for the first image in the sequence and added to the ROI Manager[24]. Figure 34 demonstrates the determination of the ROI. The same was done for the last image in the sequence. After that the ROI is interpolated[25] the area is measured (strg+m) and saved. The ROI is set as demonstrated in figure 34.

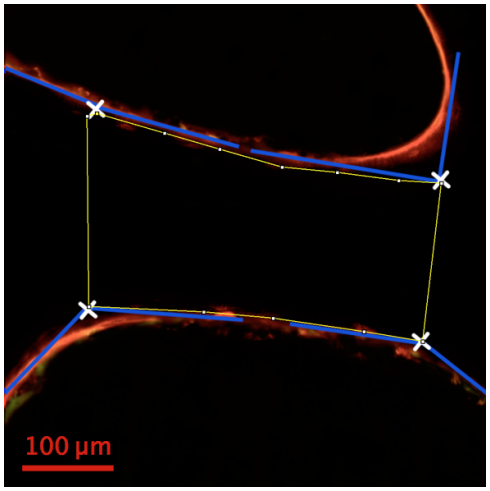

Figure 34: Definition of Region Of Interest (ROI)
The blue lines are the tangents on the trabecular wall at the curvature. The white cross marks the point of intersection. The yellow line is the ROI set with the ImageJ polygon tool.

Then the histogram macro is used to determine the amount of microdamage (for the macro see appendix(9.5) [26]. The results are exported into a excel sheet and a threshold is determined for the analysis of the gray values. After trying different thresholds on a number of images it was decided to use the Triangle threshold method [27](see figure 35).

22 File - Import - Image sequence... - Convert to 8-bit Grayscale
23 Image - Stacks - Tools - Deinterleave
24 Choose ROI with polygon tool - Analyse - Tool - ROI Manager - Add[t]
25 ROI Manager - Moore - Interpolate ROI (Save ROI)
26 Plugins - Macro - Run - Histogram.txt
27 Image - Adjust - Threshold - Triangle/Stack histogram

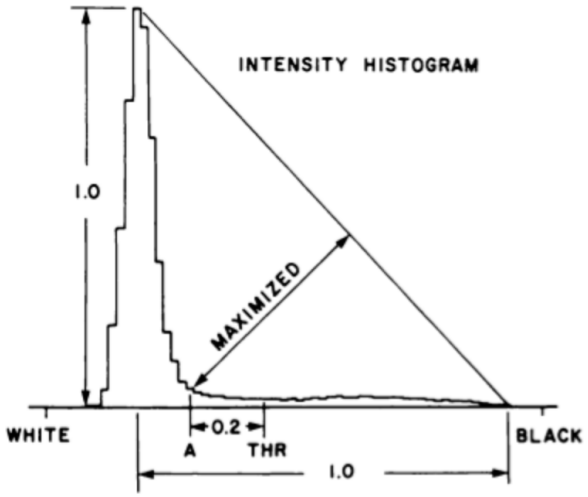

Figure 35: Triangle Threshold
The threshold was selected by normalizing the height and dynamic range of the intensity histogram, locating point A as shown and then adding a fixed offset.[82].

Afterwards the histogram data is analysed with the given threshold and the counter sum gives the pixel number of damaged area. This can be converted to μm^2. As the height of one z-stack is known from the microscope analysis the damaged volume can be calculated. If only one type of microdamage occurs in a sample the volumetric analysis is finished here as the whole damaged volume can be assigned to one type. In contrast, in samples that contain linear cracks and diffuse damage the damaged volume (V_{tot}) is assigned to the different types. This is done by segmenting a new ROI for the linear cracks since these are easier to mark out than diffuse damage. Linear cracks are assumed as elliptical. Therefore the ROI is set as an ellipse around the linear crack (see appendix 9.2 figure 46). Again, the Histogram Marco is executed and the counts for the linear cracks are summarised after thresholding. Thus, the damaged volume (V_{lin}) which is assigned to linear cracks is known. The diffuse damaged volume (V_{diff}) is gained by subtraction the counts of linear damaged volume with the count of the total damaged region. The volume of the trabecula (V_{trab}) was determined through measuring the volume of the ROI and the known z-stack hight (see section: 4.4.2 Image Data Analysis).

Therefore following parameters are known shown in table 7:

Specification	**Name**	**Calculation**
Lin.Cr. [#]	Number of Linear Microcracks	ImageJ
Diff. [#]	Number diffuse damaged areas	ImageJ
V_{trab} [μm^3]	Volume of trabecula	ImageJ
V_{tot} [μm^3]	Volume of total damaged area	ImageJ
V_{lin} [μm^3]	Volume of linear cracks	ImageJ
V_{diff} [μm^3]	Volume of diffuse damage	ImageJ
Dam.Den [%]	Total damaged area density	V_{tot} / V_{trab}
Lin.Cr.Den [%]	Linear Crack Density	V_{lin} / V_{trab}
Diff.Den [%]	Diffuse Damage Density	V_{diff} / V_{trab}

Table 7: Parameters for 3-dimensional analysis

2-Dimensional Analysis

Additionally, an analysis of single slices of the samples is performed, to compare gained data with values from literature. Therefore, two representative images of a sample are taken from the z-stack. Each of these images is analysed separately. The ROI is set as demonstrated in figure 34. The histogram macro is executed for the single image and thresholding is done as described for the volumetric analysis. Except that the ROI only must be defined for one single image (no interpolation necessary). Afterwards the linear cracks are measured with the "elliptical selection" tool. For purposes of comparison the length was measured in length and width with the "straight line" tool. For the elliptical selection the histogram was again executed to gain the counts for the linear cracks. Again, these counts are subtracted from the total amount of damage to gain the area of diffuse damage. This procedure was executed for two representable images of the z-stack to get more data. The following parameters were extracted:

Specification	**Name**	**Calculation**
A_{trab} [μm^2]	Area of Trabeculae (ROI)	ImageJ
Lin.Cr. [#]	Number of Linear Microcracks	ImageJ
Diff. [#]	Number diffuse damaged areas	ImageJ
Lin.Cr.X.Length [μm]	Length of linear microcrack Nr.X	ImageJ
Lin.Cr.X.Width [μm]	With of linear microcrack Nr.X	ImageJ
Lin.Cr.X.Area [μm^2]	Area of linear microcrack Nr.X	ImageJ
Lin.Cr.S.Den [$\mu m/\mu m^2$]	Linear Crack Surface Density	Lin.Cr.(Xi).Length / Area
Lin.Cr.Den.2D [%]	Linear Crack Density 2D	Lin.Cr.(Xi).Area / Area
Diff.Den.X.Area [μm^2]	Area of Diffuse Damage	ImageJ
Diff.Den.2D [%]	Diffuse Damage Surface Density 2D	Diff.S.Den / Area
Dam.Den.2D [%]	Total damaged area density 2D	Diff.Den.Area / Area

Table 8: Parameters for 2-dimensional analysis
Xi: Sum over all linear cracks if more than more occurs

4.5 Statistical Analysis

For statistical analysis IBM SPSS was used. For each sample the elastic modulus and stress- and strain-amplitude was measured at the begin and the end of testing and the goal was to evaluate if there is a significant difference between start and end. For interpretation of the microdamage generated during testing the damaged areas were compared and evaluated for any significant differences. This was done by testing data for normal distribution with a Shapiro-Wilk-Test. If data sets were normally distributed also variance homogeneity was tested. In principle, for data which fulfil this demands a t-test can be executed. To test for an possible decrease in elastic modulus and stress- and strain-amplitude a t-test for paired samples had to be executed since one sample was tested at two points (first set, last set). For analysing microdamage from CLSM images a t-test for paired samples was performed. Data that did not fulfil criteria for t-test have to be tested with nonparametric tests. For elastic modulus and stress- and strain-amplitude a Wilcoxon-Test was performed to test for a significant difference. As the measurement for these parameters was only tested at two times during the process no ANOVA with repeated measures could be performed. For analysing the damage of trabeculae a Kruskal-Wallis-Test for N variables and Mann-Whitney-U-Test for two variables was used. Kruskal-Wallis-Test was used to see if there is a significant difference in the development of linear cracks and diffuse damage over the the different numbers of cycles. Mann-Whitney-U-Test was used to check for significant difference between the types of microdamage. As sample sizes are small and also for comparison reason the nonparametric test was executed for all samples. For further interpretation of the statistical analysis also the effect size was calculated for samples with significant results. A significance threshold of $p = 0.05$ was used.

5 Fatigue Test Design

A major aim of this thesis was to design and establish a fatigue test for cyclic tensile loading of individual trabeculae to induce various levels of microdamage. Since samples should not break due to fatigue a stop criterion had to be determined. In the following the development of the test-design is described. 20 samples were produced and the parameters and stop criterion for the fatigue tests were established.

5.1 Parameters

Reasonable parameters for testing had to be determined. As there are no references for fatigue testing of single trabeculae, settings from the literature, which come close, were chosen. A sinusoidal profile was used but the appropriate amplitude, frequency and number of cycles had to be found. For example Moore et al. (2004) determined a frequency of 2 Hz for 100 cycles [13] for a trabecular network. Waldorff et al. 2007 set a regime of 1000 cycles at 0.5 Hz [14]. Herman et al. (2010) tested rat ulna in vivo for 1500, 300 and 4500 cycles [42] with a frequency of 2 Hz. In this project a displacement controlled solution was chosen (see section: 4.2.1 Setup and Modifications).

Amplitude

Amplitude values between 0.01 mm and 0.4 mm were tested. The idea was to vary the amplitude depending on the dimensions of the sample. Therefore, a step wise increase of 0.005 mm of the amplitude after every 100 cycles was performed. For smaller samples the process was stopped earlier than for larger samples. This protocol led to long testing times and microdamage formation could not be guaranteed. Therefore, during testing the issue of different sample dimensions could be better solved by applying different pre-loads, depending on the sample size. During this process an amplitude of 0.05 mm turned out to be best fitting for most trabeculae due to trail and error. With this amplitude the samples were not fractured during testing and the best results were gained.

Frequency

Initially the frequency was set low (0.1 Hz) as it was not sure how the samples would react to the given setting and it was the goal to do not break them. Hence, frequencies between 0.1 Hz and 3 Hz were tested. According to literature a frequency of 1 Hz was used. Lower frequencies were closer to a static loading and unloading. Higher frequencies than 1 Hz seemed to harm the samples quicker than expected.

Number of cycles (NoC)

In the first testing regime, the tension on the samples dropped to zero after about 100 cycles, since the epoxy (in which the samples were embedded) relaxed over time. Hence, after every 100 cycles the test had to be aborted, a new pre-load had to be applied and the test was restarted. This lead to extraordinary long testing times. This issue was solved by putting the epoxy resin in the vacuum desiccator before using it to embed the samples (see section: 4.1.4 Embedding). With this, it was possible to expand the range to 800 cycles and the test had only be restarted 2 to 4 times instead of 15 to 30 times. A number of cycles had to be found which ensures microdamage formation to test the mechanical properties of bone and find a fitting stop criterion (see next section 5.2) The following total amounts of cycles were tested in order to find suitable numbers: 300, 600, 1000, 1500, 1700, 2100, 3000, 4000. The influence of the number of cycles, and the interaction with other settings (amplitude, frequency), on microdamage induction was used to determine the amounts of cycles that would be best usable. In the lower ranges no mircodamage was induced. At 1500 cycles the first microcracks could be recognised. At 4000 cycles most samples broke during testing. Therefore, it was decided to test samples for 3000 cycles, which was a promising amount to ensure microdamage generation (see 6 Results). In the following also a number of samples were tested for 2100 cycles (value approximately between already stated values) to see progression of microdamage.

Further, it was necessary to test if samples were loaded uni-axially since the testing protocol was newly developed and also due to changes in the set-up (sample holders, new adjustment method). Therefore, one sample was tested with the same conditions described above but with the attempt to load until fatigue failure. The fracture line was expected to be located at the middle of the trabeculae as the highest stresses were expected there (because of the curved shape). After testing sample F3 for 5051 cycles the sample broke as expected (see figure 36). Therefore, correct loading was confirmed. Additionally, stress strain curves were determined and showed a clear sinusoidal shape, as expected from the set displacement (see appendix 9.3).

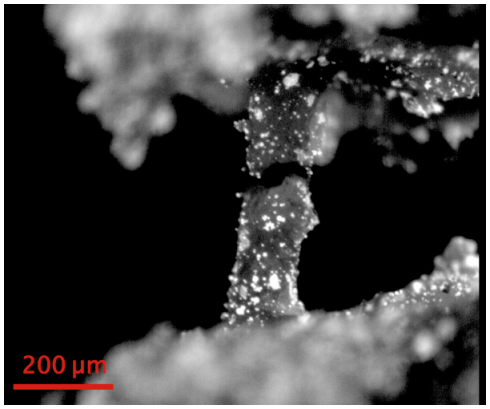

Figure 36: Sample F3 - Loading Check
Sample F3 was loaded until fatigue failure. The fracture line is located in the middle of the trabeculae as expected.

5.2 Stop Criterion

A stop criterion for testing had to be determined to ensure that a desired amount of damage formation occurs in the majority of the samples, without fracturing. Since bone is a heterogeneous, anisotropic material it is obvious that the criterion can not work without error. Different attempts were made as described below.

5.2.1 Elastic Modulus

Initially, the idea was to test until the elastic modulus (E-modulus) decreases accordingly to the model by Seref-Ferlengez et al. (2015) discussed in the introduction. As illustrated in figure 9 the elastic modulus starts to decrease right before the bone fails. As a real-time analysis during testing is not possible with the used set-up it was considered to analyse the data in regular intervals to check if a decrease of the elastic modulus could be noticed. The stop criterion for the tests should therefore be determined as a percentage of decrease of the elastic modulus.

8 samples were tested for 3000 cycles. CLSM analysis proved that microcracks were generated. Stress and strain in the parallel region of trabeculae during testing were measured for the first set and the last set before aborting the test at cycle 3000. Sequentially, mean elastic modulus for loading and unloading was evaluated for these cycles. In figure 37 the elastic modulus for sample B2 in the first and last set is shown. For other samples see appendix 9.3.1.

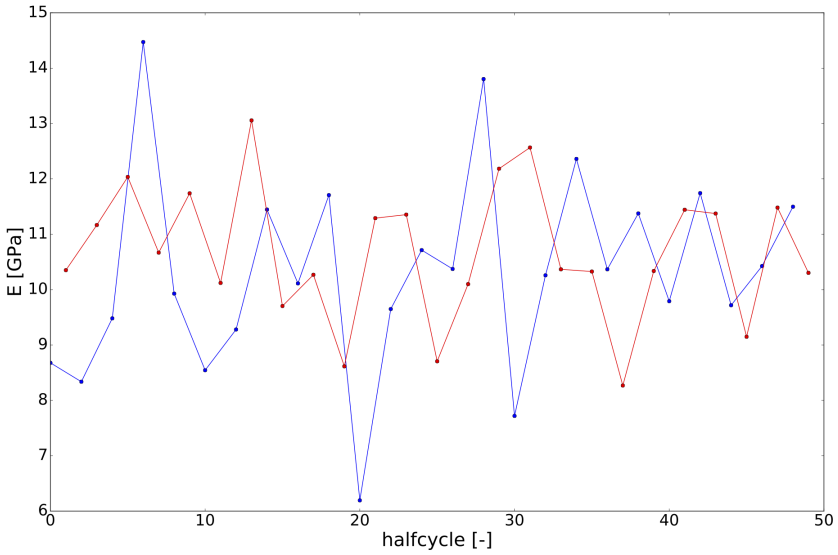

(a) First set

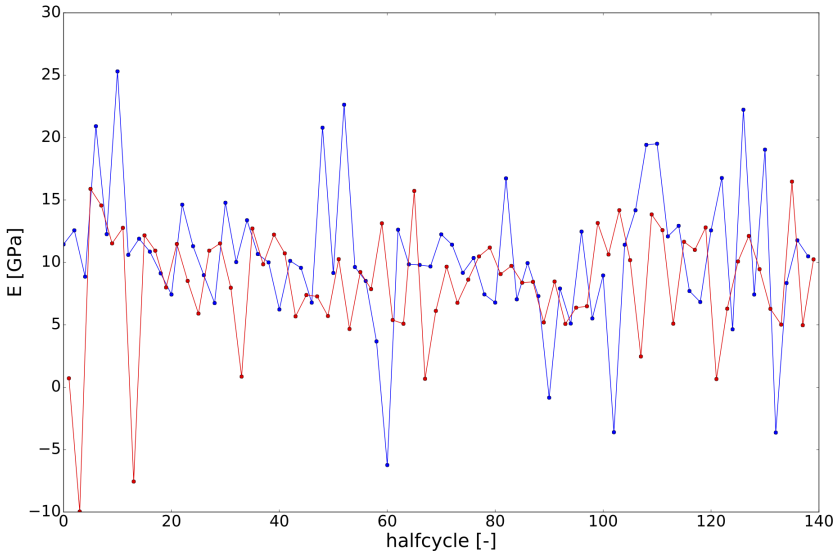

(b) Last set

Figure 37: Elastic modulus sample B2
Red lines illustrate the unloading and the blue line the loading part of a set.

The values for the elastic modulus of the first testing set were compared with the values of the last testing set. This was done separately for the loading and the unloading part of the cycle. In table 9 mean elastic modulus for loading and unloading for the first set and the last set are given.

2 out of 8 samples showed a significant decrease in the elastic modulus (E3: $p \leq 0.005$, F3: $p \leq 0.001$) for the unloading and loading phase. 3 showed a significant increase (B7: $p \leq 0.005$, G1: $p = 0.018$, I1: $p = 0.009$) for the loading phase and 2 for the unloading phase (B7: $p \leq 0.005$, G1: $p = 0.018$). Sample I1 showed no significant difference for the

unloading part (p=0.878). Sample B2 showed no significant difference at all (p=0.221 load, p=0.093 unload). For 2 samples the gained data was not representable as the values are too high (D1, G7). For the samples which showed a significant decrease in elastic modulus the effect size was also calculated (d=0.4).

Based on this results, the method of monitoring the elastic modulus was excluded as a stop criterion.

		load		unload	
Sample	**Set**	**E_mean [GPa]**	**STD**	**E_mean [GPa]**	**STD**
B2	Start	10.32	1.77	10.68	1.20
	End	10.46	5.65	8.42	4.69
B7	Start	11.76	1.54	14.72	1.18
	End	20.51	4.60	32.17	10.14
D1*	Start	41.39	12.58	42.60	16.12
	End	51.26	55.51	73.16	18.03
E3	Start	14.33	2.19	13.94	2.03
	End	9.69	1.17	9.94	1.82
F3	Start	14.84	0.50	15.99	0.72
	End	14.65	0.36	15.26	0.39
G1	Start	15.08	1.27	19.00	1.28
	End	22.67	3.11	25.56	3.20
G7*	Start	35.72	8.72	26.66	7.04
	End	22.59	1.17	32.02	11.37
I1	Start	7.96	0.43	8.28	0.72
	End	8.73	0.43	8.40	0.28

Table 9: Elastic modulus
For every sample the elastic modulus from the first set (Start) got compared to the last recorded set (End). This was done for loading and unloading. In this table the mean values for elastic modulus are given. Values for samples marked with * are not reliable and were thus excluded from further analysis.

5.2.2 Amplitude

As it turned out that the decrease of the elastic modulus could not be recognised although microdamage was visually detectable. As a consequence the stop criterion had to be changed and the strain and stress amplitudes were investigated.

Data of the same 8 samples were evaluated for their stress and strain amplitude. As for the elastic modulus the values of stain and stress amplitudes got compared from the first set to the last set. 2 samples were excluded from the evaluation based on too high values of elastic modulus (D1, G7). 5 samples showed a significant increase in stress

amplitude ($p \leq 0.001$ for B2, B7, F3, G1, I1) and one a significant decrease ($p \leq 0.001$, E3). 3 showed a significant increase in strain amplitude ($p \leq 0.001$, B2, E3, G1) and 3 a significant decrease ($p \leq 0.001$, B7, F3, I1). The effect size for stress amplitude is $d=0.587$ and for strain amplitude $d=0.834$ on average. In figure 38 the stress and strain amplitudes are illustrated for a representative sample. For other samples and stress-strain data see appendix 9.3.2, 9.3.3.

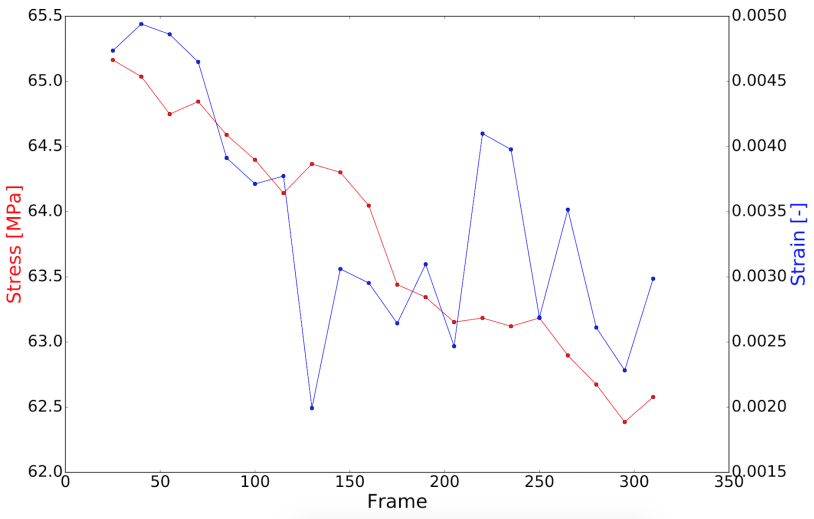

(a) First set

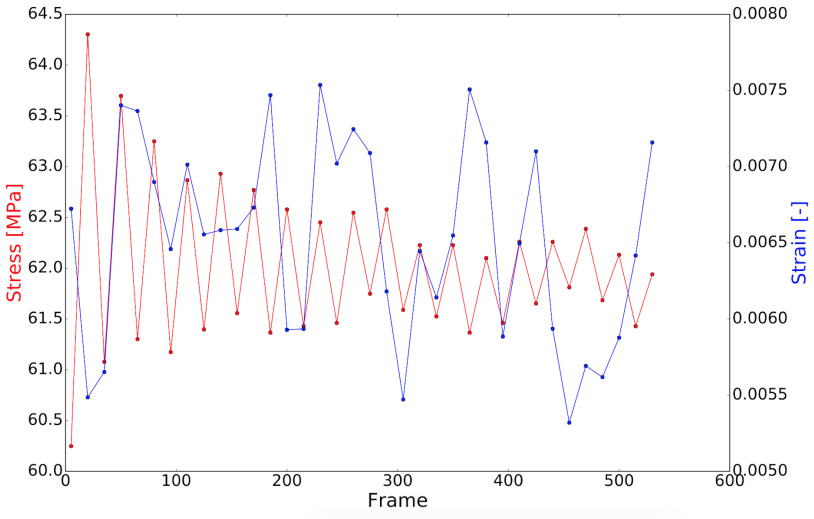

(b) Last set

Figure 38: Stress and strain amplitude for sample E3
Red dotted lines illustrate the strain amplitudes and the blue dotted line the strain.

In table 10 the gained mean values for stress and strain amplitude are given:

Sample	Set	Stress [MPa]	STD	Strain [-]	STD
B2	1	48.08	0.45	0.004	0.001
	4	103.70	0.60	0.007	0.002
B7	1	86.71	0.38	0.006	0.001
	4	89.76	0.35	0.004	0.001
D1*	1	84.14	0.28	0.002	0.003
	4	80.75	0.14	0.001	0.001
E3	1	63.78	0.88	0.003	0.001
	4	62.02	0.79	0.007	0.001
F3	1	119.17	1.57	0.008	0.001
	4	122.72	1.21	0.008	0.001
G1	1	40.58	3.68	0.003	0.001
	4	69.65	0.63	0.003	0.001
G7*	1	60.24	1.02	0.001	0.001
	3	65.53	0.40	0.003	0.001
I1	1	49.56	0.16	0.006	0.008
	4	54.73	0.15	0.006	0.001

Table 10: Means of stress and strain amplitudes
For every sample the stress and strain amplitude from the first set (Start) got compared to the last recorded set (End). In this table the mean values within the start and end set for stress and strain amplitude are shown. Values for samples marked with * are not reliable and were thus excluded from further analysis.

5.2.3 Whitening

Another attempt was to determine a visual stop criterion, the whitening effect. It is possible to detect microdamage formation trough whitening in bone [74]. Whitening was only noticeable for 3 samples during this whole project. The effect appeared just right before samples broke. As it was not intended that the samples fail and since it was not possible to stop testing quickly enough after whitening occurrence this visual criterion was also omitted.

5.2.4 Number of Cycles (NoC)

The number of cycles (NoC) was suggested as stop criterion, however, it had to be dealt with different dimensions of trabeculae. As such, the preload was used to deal with differences in size of tested trabeculae. For this purpose trabeculae of approximately the same dimension were chosen during sample preparation. Further, samples were categorized. A trabeculae was characterized as "large" if it was more than 1.5 x 10^7 μm^3 in volume

(Average of volume of used trabeculae). A preload of 1 N for was applied for large and of 0.8 N for small trabeculae. After every 1000 cycles the load was increased by 0.1 N in both cases. This settings allowed to use NoC as stopping criterion. To show the progress in microdamage formation 2 additional sets were determined. 1500 cycles to show the beginning of microdamage formation and 2100 as an intermediate step. This lead to the settings displayed in the following table 11:

Parameter	**Value**	**Context**
Amplitude [mm]	0.05	
Frequency [Hz]	1	
Preload [N]	1 - 1.3*	$V_{trab} > 1.5$ x 10^7 μm^3
	0.8 - 1.1*	$V_{trab} < 1.5$ x 10^7 μm^3
NoC	1500	no to little damage
	2100	starting microdamage
	3000	ensured mircodamage

Table 11: Final test parameters
* value for small and large trabeculae, were increased for 0.1 N after every 1000 cycle

6 Results

Using the aforementioned protocol 21 samples were tested. 8 samples were loaded for 3000 cycles, 6 for 2100 cycles and 7 for 1500 cycles. Images in detail are shown in the appendix 9.3. Two samples could not be included into the evaluation (Sample S9 for 1500 cycles, Sample B2 for 3000 cycles) because of issues with the sample preparation after testing. These samples are excluded from the following displays and analysis.

4 samples were tested separately to check for pre-existing damage in bone. This damage could occur due to loads in vivo or the preparation steps described above. In figure 39 one of these samples is shown. As can be recognized, Alizarin Red S only settled on the contours as there are is no damage in the bone matrix visible. Still every further sample was also tested for pre-existing microdamage during this project. All samples were stained with Alizarin Red S. These 4 samples were used as reference.

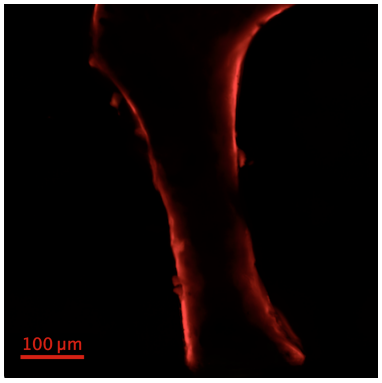

Figure 39: Fluorochrom labelling of sample N1
Sample N1 was not tested but it run through all preparation steps. After staining with Alizarin Red S no damage is visible. Only contours of bone are labelled.

Figure 40 shows representative microcrack staining at 1500 (a), 2100 (b) and 3000 (c) cycles.

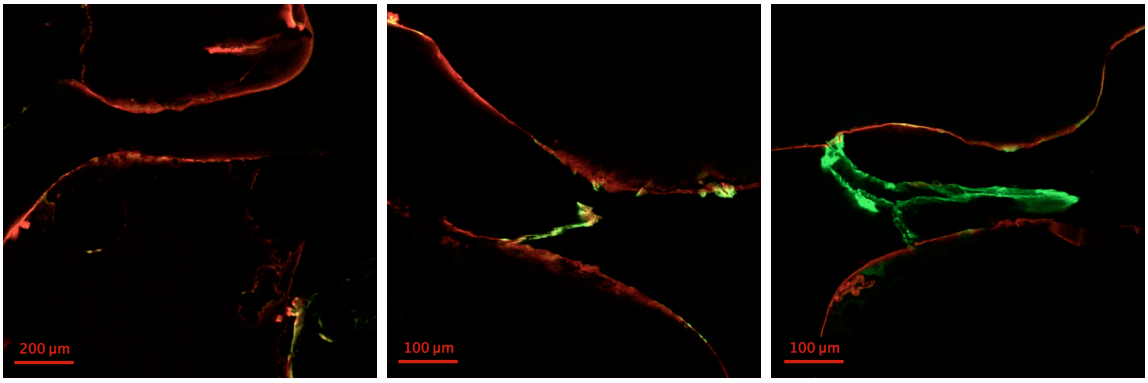

(a) 1500 cycles (b) 2100 cycles (c) 3000 cycles

Figure 40: Trend of mircodamage formation in 2D. Pre-Staining of initial microcracks with Alizarin Red S (red) and staining after tests with Calcein (green).
a) Sample F2 (1500 cycles) shows no damage b) Sample J2 (2100 cycles) shows one linear microcrack c) Sample I1 shows advanced microdamage

Samples tested for 1500 cycles showed very little to no microdamage in image analysis. 4 samples showed no microdamage at all, 2 starting damage and 1 was not evaluable (n.e.).

6 samples were tested for 2100 cycles. 2 of them showed no microdamage, whereas in 4 of them linear microcracks and diffuse damage were visible.

Out of the 8 samples tested for 3000 cycles 1 was not evaluable, whereas 7 showed linear cracks and diffuse damage.

A linear crack is defined within this project as damage which is in average 100 μm in length and 9 μm in width. Damage which is wider than 30μm was counted as diffuse damage.

In figure 41 a whole z-stack for a trabeculae showing linear cracks and diffuse damage is shown.

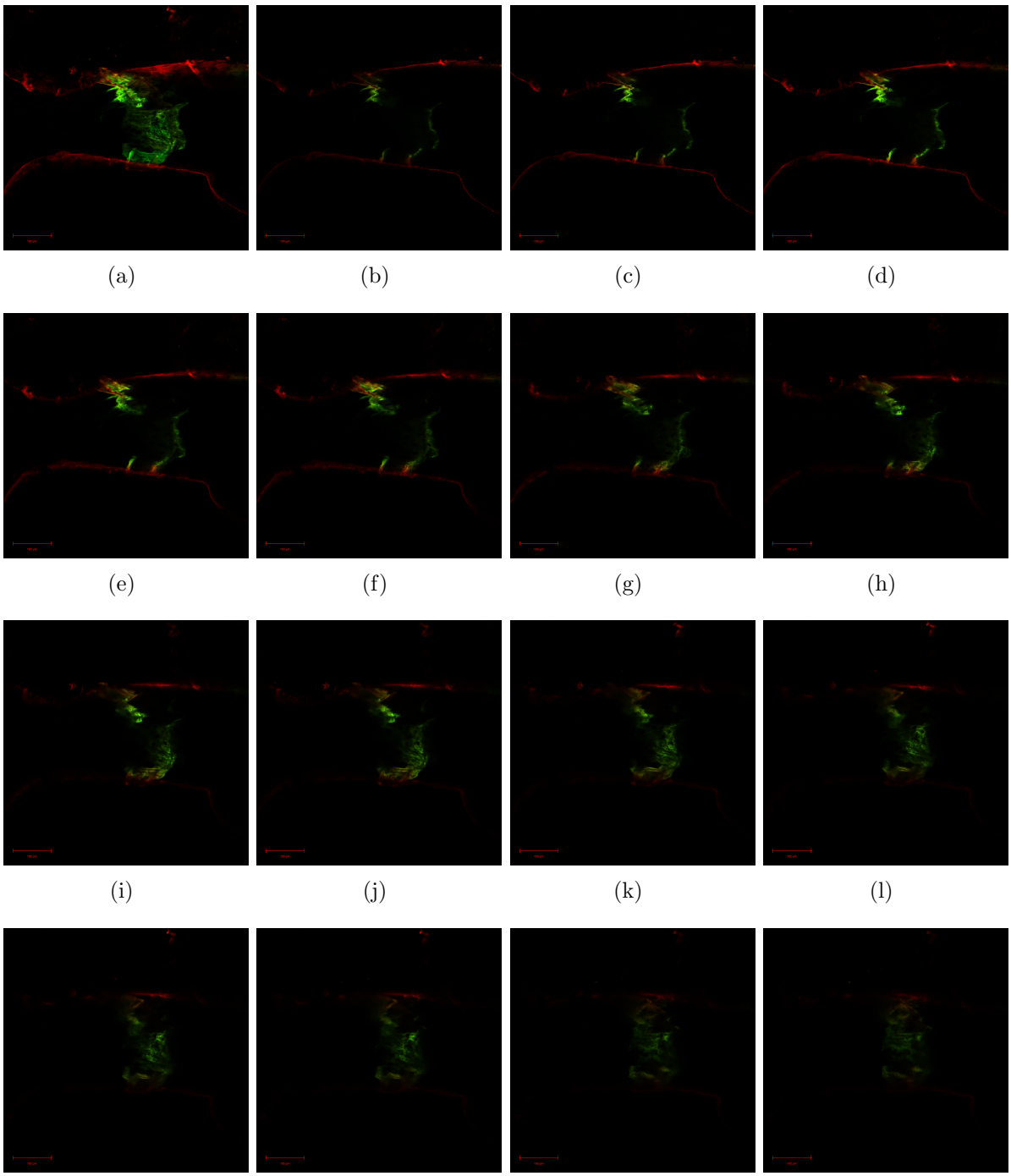

Figure 41: Trend of mircodamage formation in 3D.
Pre-staining of initial microcracks with Alizarin Red S (red) and staining after tests with Calcein (green). Sample H3 at 20x magnification (a) Maximum intensity projection (b)-(t) z-stack to demonstrate microdamage progression through sample with slice thickness of 5 μm

6.1 3-Dimensional Microdamage Analysis

The following parameters were determined in the volumetric analysis (as defined in section 4.4.2 Image Data Analysis (table 12)): The number of linear microcracks and diffuse damaged areas (Lin.Cr., Diff.), the volume of trabeculae (V_{trab}), Volume of total damaged area (V_{tot}), Volume of linear cracks (V_{lin}), Volume of diffuse damage (V_{diff}) and the densities of total damaged area (Dam.Den), linear cracks (Lin.Cr.Den) and diffuse damaged areas (Diff.Den). See also section: 4.4.2 Image Data Analysis.
4 non tested samples were also analysed using the same principal but as all values are equal zero (since no damage) the reference group is excluded from the following displays.

For 1500 cycles 4 samples were undamaged after testing, whereas microdamage was formed in 2 samples. In each of those 1 linear microcrack and 1 area of diffuse damage was observed. Further, the dimensions of the microcracks and of diffuse damage are small compared with averaged values. One sample (S9) could not be evaluated. In the case of 2100 cycles 2 samples showed no damage and in 4 samples microdamage was produced. The number of linear cracks is higher than the number of areas showing diffuse damage, although one sample does not show linear cracks at all. All samples tested for 3000 cycles showed microdamage. In 2 samples linear microcracks are visible. In every other sample only diffuse damage was prominent.

The amount of overall damage seems to increases with the number of cycles (see figure 42). The number of linear microcracks appear to rise from 1500 to 2100 cycles and decrease for 3000 cycles, but in fact no significant difference can be found (Lin.Cr.Den=0.507). Diffuse damage seems to increase continuously from 1500 to 3000 cycles (see figure 42). However this differences is also not significant (Diff.Den p=0.076). Although a trend can be derived. The damaged volume is between 0% and 1.37%. The diffuse damage density is higher than the one for linear cracks at all stages but it is only significant different for 3000 cycles ($p \leq 0.001$). Although most differences are not significant a trend can be seen for some results (for $p < 0.1$). For details of the p-values see tables 21, 22 and 23 in the appendix: 9.3.7 .

	Lin.Cr.[#]	Diff.[#]	V_{trab} [μm^3]	V_{tot} [μm^3]	V_{lin} [μm^3]	V_{diff} [μm^3]	Dam.Den [%]	Lin.Cr.Den [%]	Diff.Den [%]
1500 cycles									
S1	1	1	1.81 x 10^7	4.97 x 10^5	3.60*10^4	4.61 x 10^5	2.74	0.20	2.54
S2	1	1	2.47 x 10^7	1.12 x 10^5	1.06 x 10^4	1.12 x 10^5	0.46	0.0001	0.45
8a	0	0	1.57 x 10^7	0	0	0	0	0	0
8b	0	0	1.27 x 10^7	0	0	0	0	0	0
F2	0	0	1.42 x 10^7	0	0	0	0	0	0
S3	0	0	1.84 x 10^7	0	0	0	0	0	0
Mean							0.49	0.03	0.50
SEM							0.30	0.03	0.38
2100 cycles									
G7	0	1	2.24 x 10^7	9.41 x 10^2	0	941.49	0.0001	0	0.0001
H3	2	1	2.48 x 10^7	2.81 x 10^5	7.83 x 10^3	2.73 x 10^5	1.13	0.03	1.10
J2	1	1	2.27 x 10^7	1.92 x 10^5	6.54 x 10^4	1.27 x 10^5	0.85	0.29	0.56
J4	2	1	1.35 x 10^7	2.33 x 10^5	4.87 x 10^4	1.83 x 10^5	1.71	0.36	1.36
F1	0	0	1.19 x 10^7	0	0	0	0	0	0
G6	0	0	3.36 x 10^7	0	0	0	0	0	0
Mean							0.62	0.11	0.50
SEM							0.30	0.07	0.25
3000 cycles									
G2	1	1	1.57 x 10^7	2.94 x 10^5	3.34 x 10^4	2.61 * 10^5	1.87	0.21	1.66
J3	0	1	1.03 x 10^7	1.18 x 10^5	0	1.18 x 10^5	1.14	0	1.14
I1	0	1	2.18 x 10^7	4.56 x 10^4	0	4.56 x 10^4	0.21	0	0.21
G8	0	1	2.44 x 10^7	6.85 x 10^4	0	6.85 x 10^4	0.28	0	0.28
G1	0	2	2.32 x 10^7	5.20 x 10^5	0	5.21 x 10^5	2.25	0	2.25
E3	0	1	4.78 x 10^6	1.20 x 10^5	0	1.21 x 10^5	2.52	0	2.52
D1	2	1	1.92 x 10^7	3.01 x 10^5	1.16 x 10^3	2.99 x 10^5	1.56	0.01	1.56
Mean							1.41	0.03	1.37
SEM							0.41	0.01	0.37

Table 12: Damage determination of individual trabeculae - 3D

Measured and calculated parameters for all three measuring sets. 4 non tested samples were also analysed after the same principle but as all values are equal zero (since no damage) the reference group is excluded from this display.

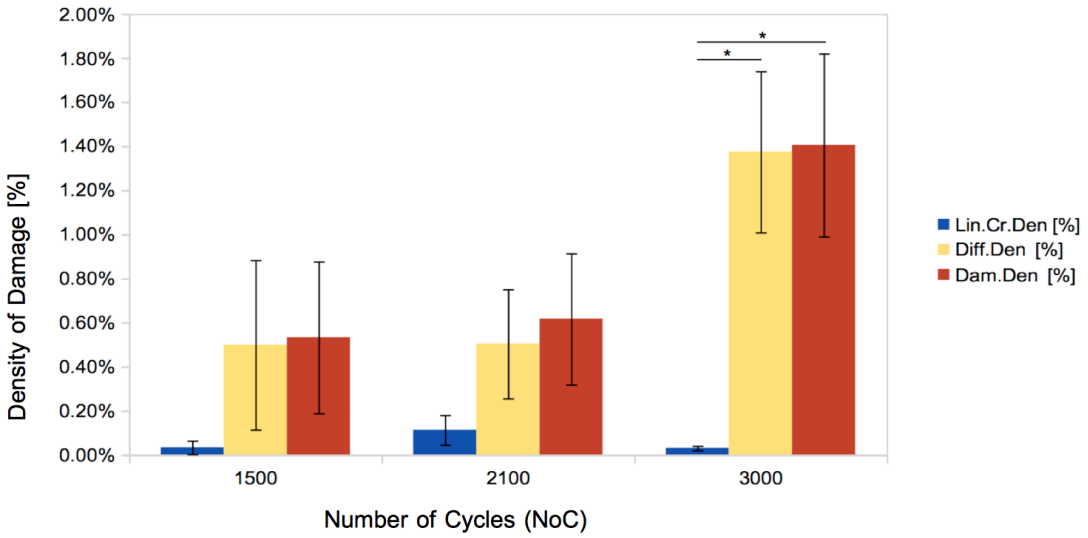

Figure 42: Damage density - 3D, dependent on number of cycles tested
Ratio of damaged areas for total damaged area density (Dam.Den), Linear Crack Density (Lin.Cr.Den) and Diffuse Damaged Density (Diff.Den) for 1500, 2100 and 3000 cycles. Bars represent the mean, whiskers the standard error of the mean. *p<0.05.

6.2 2-Dimensional Microdamage Analysis

The following parameters were determined in the volumetric analysis (as defined in section 4.4.2 Image Data Analysis (table 13)): 2 representative slices of each sample were chosen for the 2-dimensional analysis. One slice is the first slice in which the microdamage of the sample is clearly visible and the second one is chosen randomly from the rest of the z-stack. The following parameters of linear microcracks were determined: The length and width of linear cracks (Lin.Cr.X.Length, Lin.Cr.X.Width) and the area of linear microcracks (Lin.Cr.X.Area). Diffuse damage was determined as area (Diff.Den.X.Area) with a polygon approach (see section: 4.4.2 Image Data Analysis). From that the Linear Crack surface density (Lin.Cr.S.Den), Linear Crack Density in 2D (Lin.Cr.Den.2D) and Diffuse Damage (Surface) Density (Diff.Den.2D) were calculated. See also section: 4.4.2 Image Data Analysis.

As previously done in the 3D evaluation 4 non tested samples were analysed using the same procedure. As all values are equal zero (since no damage was induced) the reference group is again excluded from the following displays. In table 13 the most important parameters are shown. Additional ones can be found in the appendix 9.3.6.

		A_{trab} [μm^2]	Lin.Cr.S.Den[$\mu m/\mu m^2$]	Lin.Cr.Den.2D [%]	Diff.Den.2D [%]	Dam.Den.2D [%]
1500 cycles	Slice					
S1	1	1.20 x 10^5	8.56 x 10^3	0.71	0.83	1.54
	2	1.21 x 10^5	5.37 x 10^3	0.45	2.07	2.52
S2	1	7.93 x 10^4	8.53 x 10^3	0.74	2.65	3.39
	2	7.93 x 10^4	8.54 x 10^3	0.74	3.53	4.27
8a	1	0	0	0	0	0
	2	0	0	0	0	0
8b	1	0	0	0	0	0
	2	0	0	0	0	0
F2	1	0	0	0	0	0
	2	0	0	0	0	0
S3	1	0	0	0	0	0
	2	0	0	0	0	0
Mean				0.22	0.76	0.98
SEM				0.13	0.48	0.59
2100 cycles						
G7	1	1.15 x 10^5	0	0	0.55	0.55
	2	9.83 x 10^4	0	0	1.06	1.06
H3	1	1.23 x 10^5	3.95 x 10^3	0.51	0	0.51
	2	1.20 x 10^5	1.31 x 10^4	1.38	0	1.38
J2	1	1.20 x 10^5	1.06 x 10^4	0.92	0.25	1.17
	2	1.26 x 10^5	1.44 x 10^4	1.31	2.84	4.15
J4	1	7.93 x 10^4	7.37 x 10^3	1.40	3.07	4.47
	2	7.93 x 10^4	1.28 x 10^4	2.35	4.75	7.10
F1	1	0	0	0	0	0
	2	0	0	0	0	0
G6	1	0	0	0	0	0
	2	0	0	0	0	0
Mean				0.66	1.04	1.70
SEM				0.33	0.66	0.94
3000 cycles						
G2	1	7.74 x 10^4	1.68 x 10^3	0.53	9.95	10.47
	2	8.17 x 10^4	1.84 x 10^3	0.84	0.31	1.16
J3	1	8.34 x 10^4	0	0	5.16	5.16
	2	8.83 x 10^4	0	0	4.19	4.19
I1	1	8.00 x 10^4	0	0	5.00	5.00
	2	8.00 x 10^4	0	0	6.13	6.13
G8	1	8.00 x 10^4	0	0	3.34	3.34
	2	109671.64	0	0	2.31	2.31
G1	1	8.71 x 10^4	0	0	4.97	4.97
	2	9.57 x 10^4	0	0	4.57	4.57
E3	1	6.19 x 10^4	0	0	4.04	4.04
	2	6.33 x 10^4	0	0	3.71	3.71
D1	1	1.04 x 10^5	0	0	7.38	7.38
	2	1.28 x 10^5	1.21 x 10^3	0.67	1.01	1.68
Mean				0.15	4.43	4.58
SEM				0.11	0.93	0.90

Table 13: Damage determination of individual trabeculae - 2D
Measured and calculated parameters for all three measuring sets. For every sample 2 representative slices of the z.stack were analysed. 4 non tested samples were also analysed using the same procedure but as all values are equal zero (since no damage was induced) the reference group is excluded from this display.

The trend of microdamage formation was similar to the one of volumetric analysis (see figure 43). The total amount of damage increases significant with the number of cycles ($p \leq 0.001$). By looking closer in the data it was found that the significant difference is between cycle set 2100 and 3000 ($p = 0.05$). The same applies for diffuse damage ($p \leq 0.001$).

The area damaged by linear microcracks rises first and seems to decrease again after 2100 cycles but the difference is not significant (Lin.Cr.Den.2D p=0.092). The densities of damages appear to be higher than for the volumetric analysis but they are only significantly different for diffuse damage and total amount of damage at cycle set 3000 (Lin.Cr.Den.(2D) p=0.971, Diff.Den(2D) p=0.003, Dam.Den(2D) p≤0.001). For details of the p-values see tables 21, 22 and 23 in the appendix: 9.3.7 .

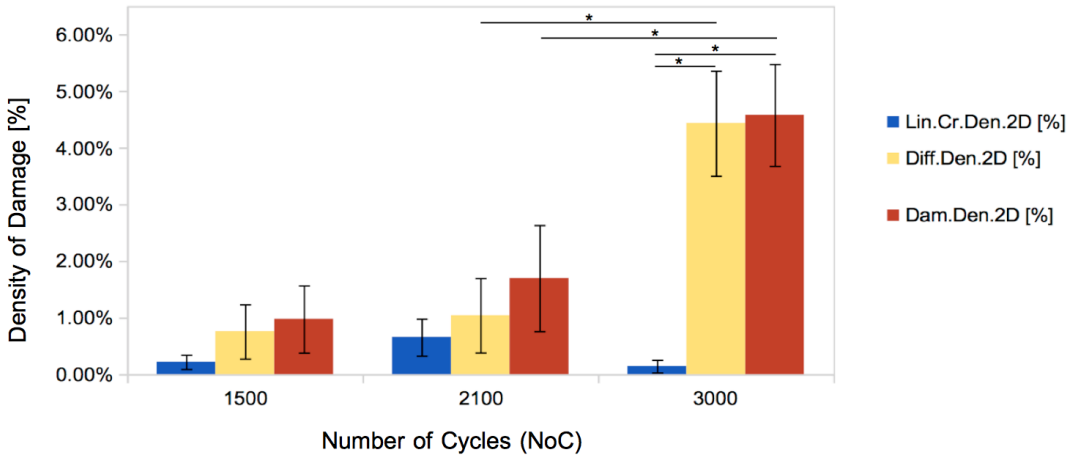

Figure 43: Damage density - 2D dependent on number of cycles tested
Ratio of damaged areas for total damaged area density 2D (Dam.Den.2D), Linear Crack Density 2D (Lin.Cr.Den.2D) and Diffuse Damaged Density 2D (Diff.Den.2D) for 1500, 2100 and 3000 cycles. 4 non tested samples also got analysed after the same principal but as all values are equal zero (since no damage) the reference group is excluded from this display. Bars represent the mean, whiskers the standard error of the mean.
*p<0.05

7 Discussion and Outlook

This thesis successfully established a novel mechanical testing protocol for microdamage induction in individual trabeculae. Further, a staining protocol was established to determine microdamage formation at two sequential time points. This will be discussed in the following section (7.1). Using the developed testing regime, tested individual trabeculae showed an increase in microdamage with an increasing amount of tested cycles. The results of microdamage characterization and its dependence on loading cycles will be discussed in section 7.2.

7.1 Methods

The developed methods of sample preparation and testing were successfully rolled out. Nevertheless, some aspects have to be mentioned and will be discussed in the following section.

The sample preparation is a very sensible process which requires a lot of practice and experience. Therefore, it is very time-consuming to learn and additionally the result depends on the skills of the preparateur. The technique of the executing person must be optimized before usable data can be generated during testing. The step of cutting the trabeculae out of the bone slices and the embedding are the most sensible steps. Since trabeculae are highly individual and the trabecular is heterogeneous these steps cannot be automatised through mechanical devices. The individual response to the orientation and structure of the trabeculae is necessary. Another issue is the uncertainty if during this elaborate process of sample preparation the samples are damaged before actual testing. The bone milling, embedding and transfer of samples between steps have all a risk of generating damage in the bone matrix through uncontrollable, unknowingly imposed loads. Therefore, 4 samples were stained with the chelating agent Alizarin Red S after the preparation was finished. Generated microdamage can thus be visualized. None of these 4 samples showed any damage (see figure 39). Nevertheless, it has to be mentioned that during the whole project 30 samples broke due to the preparation steps. It is assumed that there are 2 possible outcomes. Either samples get damaged during one of the steps and break anyway or they run through the steps without damage at all. As such, the loads which can harm the samples during the preparation are uncontrollable as they are involuntarily applied. Therefore, it is likely that they are large enough to break fragile samples as trabeculae immediately.

Further the analysis of these 4 samples showed, that there was no pre-existing damage in

the bone from loads experienced in vivo. The used bone was from a 16 months young bull. As the used bone is from a young individual it is plausible that no pre-existing damages are seen. For older or diseased bone the situation would be different [8]. Further an issue with Alizarin Red S was noticed during this project which might have consequences for testing older or diseased bones. Samples were stained with Alizarin Red S before testing and with Calcein after testing. Alizarin Red S fluorescent labels the surface of the trabeculae and eventual pre-existing damages in red, whereas Calcein labels only the microdamage formed during testing in green. It was noticed that for some damage in the bone matrix Alizarin Red S bound to these as well. Therefore, some damages fluoresce partly red (see figure 44).

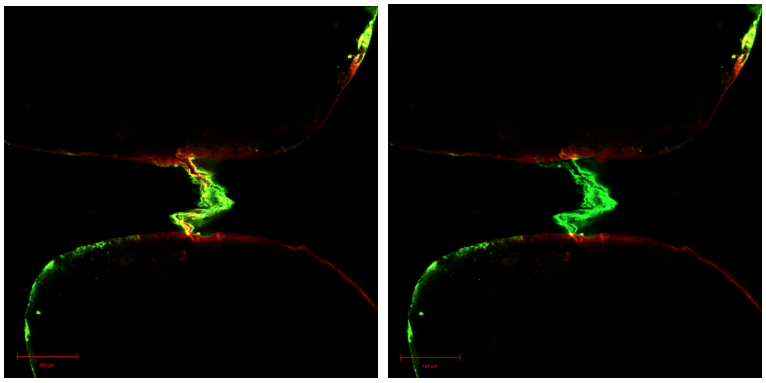

(a) Original image (b) Colour-corrected image

Figure 44: Original vs. colour-corrected image
a)Sample J3 showed in 20x magnification microdamage fluorescing green and an area fluorescing red. It appears that at this area the sample was predamaged and a macro crack formed during testing. This could not be confirmed as no crack was visible. b) Colour-corrected Image

The first thought would be that these cracks were pre-existing ones and expanded during testing. But the fact that we had 4 reference samples which showed no damages contradicts this assumption. By investigating all images it was noticed that all these areas (labelled green and red) belonged to severe damages (large cracks). This was also recognized for samples which broke during testing. Alizarin Red S bound to the fracture surface (see figure 45).

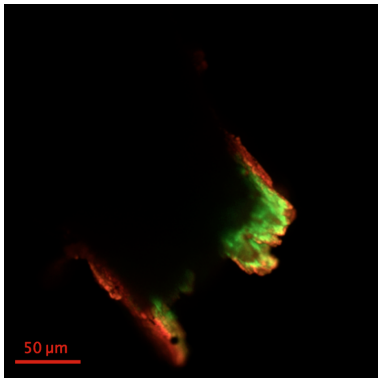

Figure 45: Issue with Alizarin Red S
Sample S7 broke during testing. It was stained with Alizarin Red S before testing and with Calcein afterwards. It is recognised that at the breaking-line the sample also fluorescents red.

It is assumed that through the long testing time in HBSS the agent may get partly dissolved again and has time to bind to forming cracks. This can be an issue in testing old or diseased bone under these conditions. The protocol developed by O'Brien et al. (2002) for sequential labelling was not developed for testing samples over several hours. Therefore, the effect observed during the original study was not an issue. In future projects when old or diseased bone is tested with the protocol this effect must be investigated further. One attempt would be to test the different chelating agents in the set-up to check if every one of them shows this behaviour. Since for the samples tested during this project the possibility of pre-existing damages could be ruled out the CLSM images were color corrected (as seen in figure 44b).

Another issue was the relaxation of epoxy resin which was used to embed the samples. The relaxation of the glue caused a drop of the load on the sample during testing to zero after 100 cycles. Therefore, the test had to be restated several times. This issue could be solved through putting the epoxy into vacuum for 1 minute to remove the air. This improved its rigidity and around 800 cycles could be performed without restarting. Nevertheless, relaxation occurred which is still an improvable task in further projects.

For the set-up following improvements could be considered for future projects: The sample holders have to be slightly bigger than the samples itself to make it possible to place the epoxy ends of the sample in them without bending them. Therefore, compression test and shear loadings cannot be performed with this setup. This could be changed for example with a modified sample holder or another way to place the samples in it. Further, the camera-SEL interface exhibited some issues. A frame rate higher than 10 Hz was followed by a frame drop during recording. Therefore, the time-resolution of the videos was limited

and the elastic modulus could not be used as stop criterion. Further improvements could change this.

7.2 Results

The results of this thesis clearly show that there is an increase of microdamage density with increasing load cycles (in 2D and 3D analysis). In particular, diffuse damage is apparently the major type of microdamage, whereas linear microcracks evolve predominantly at medium (2000) cycles and decrease at high load cycles (3000).

An issue which has to be discussed at the beginning is the definition of "linear crack" and "diffuse damage". Taylor et al. (1998) made an effort to establish a 3-dimensional measuring technique for linear cracks in bone [83]. They assumed cracks as elliptical and made a proposal to unify crack measures. Most other papers measured damage in 2D. For example Burr et al. (1989), (1990), Mori et al. (1997), Lee et al. (1998) and others measured linear cracks from tip to tip [50], [84] [85]. But in these studies the width of cracks was not always taken into account. Although linear cracks are said to have sharp borders their shape is not always perfectly linear. For instance, Fazzalari et al. (1998) mentioned straight and curved or mixed-shaped cracks [33]. These shapes were also experienced during this project. Therefore, it would be of interest, if in the previous mentioned papers only perfect linear cracks were investigated. Since it is not reasonable to measure curved linear cracks with the tip-to-tip method. As most papers make no statements about the shape of the cracks the influence of this cannot be answered. For this project, linear cracks were measured from tip-to-tip, if they were indeed linear and with a number of short lines following the run of the crack if they were curved. This seems to be a valid attempt and should be considered for following studies. Also the methode of how diffuse areas are measured is not explained in detail in the literature. Vashishth et al.(2000) specified a diffused damaged area and gave the values of damaged area as percent of the whole bone surface area. Nevertheless, the determination of the area of diffuse damage is also not clearly defined [15].
In the current study, an effort was made to clarify the definition of a linear crack and diffuse damage. The authors of different papers were contacted and it took some endeavour to design a fitting method, which allowed an analysis of data with a suitable comparison to other values of the literature. Therefore, it is demanded to settle on one reproducible microdamage determination method. A proposal is made with the approach developed during this thesis. A benefit of the method used during this thesis is, that it can be applied to 2D and 3D data. The method appears to be a solid way of evaluating the microdamaged area and volume. Further, this should be an appeal to other authors to

be aware of the fact, that imprecise documentation of the method used to evaluate the damaged areas make meaningful comparison between studies nearly impossible. It seems that most people working in the field of microdamage rely on their experience as it is often the case with histological methods. But as it is shown during this study there are relatively simple ways to define the areas affected by linear cracks and diffuse damage and a consistent method would be a great benefit in future studies.

The average linear microcrack in this project was 93 μm long and 9 μm in width. This length is in the range of values found in the literature (Wenzel et al. (1996) 80 μm, Mori (1997) 71 μm for young and 90 μm for old bone, Moore et al. (2004) 50 μm [84]) [31] [13]). But as mentioned before no further information about the measuring technique of linear cracks is given and a comparison must therefore be treated with caution.
Vashishth et al. (2000) determined 15% diffuse damaged area for males and 10% for female vertebral bone (trabecular network, physiological load). Nevertheless, again the determination of the area of diffuse damage is also not clearly mentioned either [15]. In this project 4.43% diffuse damaged area was measured on average (2D, 3000 cycles). In 3D analysis and for lower cycles (1500, 2000 cycles) the percentage is lower. A possible explanation of the lower values in the current study, compared to Vashishth et al (2000), could be that in this study single trabeculae were tested instead of a network of trabecular bone. Values of diffuse damaged area are not further compared to other studies as the definition of area is not well documented [15].

Comparing the results of this project the trend of mircodamage formation in 2D is the same as in 3D. The overall number of damage increases with the test duration. The more cycles are performed the more damage occurred. For the total amount of damage a significant difference for the different sets of cycles could be found in 2D analysis ($p \leq 0.001$) but not for 3D ($p=0.09$). For diffuse damaged areas the same applies (2D: $p \leq 0.001$, 3D: $p=0.076$). For linear cracks neither in the 2D analysis nor in 3D a significant difference could be found (2D: $p = 0.092$, 3D: $p = 0.507$). By having a closer look at total damaged area and diffuse damage it is noticeable that the significant difference occurs between 2100 and 3000 cycles (Dam.Den.2D: $p \leq 0.005$, Diff.Den.2D: $p \leq 0.001$). But by looking at figure 42 and figure 43 a trend of diffuse damage increased steady can be seen whereas the number of linear cracks was highest for 2100 cycles and seems to decrease for 3000 cycles. One explanation would be that for longer fatigue load the linear cracks merge and appear as diffuse damage as they have time to expand. Possible reasons for non-significant differences between 1000 and 2100 cycles are likely the rather small sample sizes and the fact that individual trabeculae are tested. For comparison, in trabecular networks more cracks are found and counted. In this study only damage in the defined

ROI are taken into account (which is the trabecular shaft). As the p-values are smaller than 0.1 it can be speculated that there is still a trend of microdamage formation also in the 3D analysis. This trend could be confirmed in further tests with a higher sample number. During this study 20 samples (1500: n=6, 2100: n=6, 3000: n=7) were tested but to gain more significant values more than 10 samples should be tested for each set of cycles. Also the stop criterion could make an tribute to the non significant differences as the number of cycles as it is not the most precise criterion. The individual size of trabeculae is taken into account by the adaptation of the preload, but the appearance of trabeculae are very heterogeneous and therefore the quality of this criterion has to be seen critically. Also for age and osteoporotic bone the chosen numbers of cycles could be too high. With further adaptation in the setup the decrease in elastic modulus may still be a valid option for stopping the test and more significant data could be generated. For further discussion see section 7.3 Outlook.

By comparing the number of linear cracks to diffuse damage areas a significant difference can be found for the sets of 3000 cycles in 2D and 3D (2D: $p \leq 0.001$, 3D: $p \leq 0.001$). For 2100 and 1500 the p-value was larger than 0.06. Again, a trend can be seen. It is plausible that for the highest cycle number the difference is significant as the most damage is generated. Diab et al. (2006) determined an age-dependent formation of linear cracks in human bone and thus concluded that they occur more often in old bone than in young bone [7]. Also Schaffler et al. (1995) postulated the age dependence of linear cracks [8]. In this study young bone from a 16 month old bull was used. As bovine trabecular bone has a similar structure to human bone it was expected to count more diffuse damaged areas than linear cracks. Also, the tests during this study are performed under tensile conditions. This can contribute to the fact that more diffuse damage is found. Seref-Ferlengez et al. (2015) found that linear cracks are forming preffered under compression [6].

In a direct comparison between 2D and 3D data there was only a significant difference at 3000 cycles for total damaged area and diffuse damaged area (Dam.Den: $p=0.003$, Diff.Den: $p \leq 0.001$). But as the number of tested samples is small. Therefore, the effect size was tested and d-values smaller than 0.1 were gained which indicate that the p-values do not have a large impact. Also by looking at the absolute numbers it is recognised that more linear cracks are counted in 2D data. This leads to an larger issue observed during this project. The categorization of damage is not as clear. In 2D only a segment of the whole damage is seen. The nature of microdamage is diverse and this is even more visible in 3D. For example a crack which appears in one plane as linear might develop through the trabeculae to a diffuse damage (observed during this project). Therefore it makes

sense that more linear cracks are counted in 2D than in 3D. This is a clear indication that results from 2D analysis has to be treated critically. Fazzalari et al. (1998) introduced the method to investigate the three-dimensional nature of microdamage in cancellous bone. They showed the advantages of a volumetric analysis compared to a 2-dimensional analysis. The behaviour of damage formation throughout the bone can be helpful to understand their influence and role in fractures. But the results of Fazzalari et al. (1998) about the nature of diffuse damage are contradictory to the ones gained during this project. Fazzalari et al. (1998) showed that diffuse damage appears the same when viewed in thee orthogonal planes [33]. This leads to the discussion if CLSM is a sufficient enough tool for investigation of microdamages. The resolution of CLSM is in the order 0.1-0.4 μm in x- and y-direction. But in z-direction the resolution is usually in order of 0.5-1.4 μm depending on the used objective. Also the samples have to be prepared for CLSM imaging which takes a lot of effort. Further trabeculae have no plane surface which leads to light scatter of the laser beam on the sample. Therefore, the samples have to be milled and volume of the trabeculae gets lost during this step. However, it must be noted that not damaged volume gets milled away as the sample gets regularly checked (see section: 4.3.1 Preparation Steps for CLSM Imaging). But although, the surface of the samples were evened out the resolution of the CLSM is not consistent when imaging through the z-plane. Therefore the study of Fazzalari et al. (1998) has to be questioned [33].

In addition, most studies on microdamage are done for cortical bone. Therefore, the number of comparable studies for trabecular bone is limited. This number decreases for tests on individual trabeculae hence most studies are done for trabecular networks. Therefore, a direct comparison to values from literature is hardly possible and a compromise was necessary to deal with references. A main value found in the literature is crack density (Cr.Den [# / mm^2]). Comparing the Cr.Den [# / mm^2] to values of this project is not possible. Due to the fact that in other studies networks of trabeculae were tested a much higher count of linear cracks was reported [84], [14].

Another limitation must be taken into account for comparison to other studies as a tensile load was used in the current project. In contrast, most other studies performed compression tests (For example see: Goff et al. (2015) [12]. Waldorff et al. (2007)[14]). Goff et al. (2015) performed cyclic compression tests on trabecular networks of human vertebral cancellous bone and analysed microdamage in 3D. One of their findings was that a few large regions of microdamage (which accounted for 70% of all microdamage) caused by cyclic loading lead to reductions in Young's modulus and that microdamage accumulation in fatigue is likely dominated by heterogeneity in tissue material properties rather

than stress concentrations caused by micro-scale geometry [12]. According to their results most microdamage was 30 μm away from the trabecular surface. These findings correlate with observations made during this thesis. When having a look at he maximum intensity projections (see appendix 9.3.5) it can be recognised that for 3000 cycles microdamage is mostly concentrated on a few large regions. Also most microdamage was found inside the trabeculae and not on the surface of it. For most samples around 20 to 30 μm had to be milled away to detect microdamage.

As the number of studies investigating microdamage in 3 dimensions is small it is also feasible to have a look at 2D data for comparison. 2D analysis of this project can be compared to literature but the defined parameters have to be taken with a grain of salt. The crack surface density (Lin.Cr.S.Den) measured in most studies based on 2D analysis is not sufficient. This value only takes the length of linear cracks into account (Lin.Cr.S.Den=Lin.Cr.Length / Area) and not the whole damaged area like (Lin.Cr.Den.2D=Lin.Cr.Area / Area). In some studies only this value is reported and therefore diffuse damage is not evaluated. An effort was made to compare values of this thesis to Waldorff et al. (2007) [14]. However, it was decided not to take Lin.Cr.S.Den into account.

7.3 Outlook

With regard to the idea postulated in the introduction of this thesis about the model of Seref-Ferlengez et al. (2015) the decrease of elastic modulus could be reproduced to a certain point [6]. We see a significant decrease in the elastic modulus and stress/strain amplitude for some samples. Nevertheless, it must be noted that only less than half of the samples which showed microdamage also showed a decrease in the modulus and amplitude. As the effect size for these samples is reasonable (d = 0.4) it could be worthy to have a closer look at this issue. Having a higher resolution during data recording (SEL-Camera-Interface) could lead to a higher success rate. A better resolution of the camera and recoding system with a higher frame rate per second would mean that more reference points of the speckle pattern can be found and a better time resolution could be gained. Therefore, the fit of the linear regression, used for Young's modulus determination, would be more accurate and the results more precise. Thus, it may also be possible determine a stop criterion based on the decrease in elastic modulus.
During this study young, healthy bovine trabeculae were tested. But for testing osteoporotic human bone the defined NoC stop criterion could not be as sufficient. These bones are likely much more fragile and brittle and may break earlier. Therefore the decrease in elastic modulus may be a better fitting criterion. Also for samples which ruptured

during testing (for example sample F3) the failure happened without any signs visible in the video recordings (whitening etc.). Therefore it could be envisaged to reduce the amplitude and frequency slightly (e.g. 0.03 mm and 0.8 Hz) and test for longer periods (NoC: 5000). This would prolong the testing time to a minimum of 6 hours per sample. The cost-benefit ratio has to be taken into account but possibly the point before the samples break could be found easier.

8 Conclusion

In this thesis a novel test-up was successfully developed to determine microdamage formation in individual trabeculae in tension. Increasing amounts of cycles resulted in more formation of diffuse damage, compared to linear microcracks. Further, data analysis of microcracks was performed in 2D and 3D, pointing out the limitations of 2D analysis. In order to be able to compare different studies, it is strongly recommended to use a unified evaluation protocol in 3D. The developed test set-up and evaluation protocol can be used in future studies to determine e.g. differences in microdamage formation between healthy and osteoportic donors at the level of individual trabeculae. But the option to use the elastic modulus as stop criterion should still be taken into account.

9 Appendix

9.1 Protocol

This protocol contains the methods for the production and preparation of single trabecular bone samples and the hard facts of testing them under cyclic fatigue conditions to induce mircodamages and visualise them. Fore details see section: 4 Methods.

- Dissection of bone
- Cutting trabeculae
- Size measurement of trabeculae
- Embedding
- Fluorescent labelling (Part 1)
- Application of the speckle pattern
- Testing
- Fluorescent labelling (Part 2)
- Preparation for microscopic analysis
- CLSM Imaging

Dissection Of Bone

- Bone is cleaned from soft tissue
- Then it is cut into smaller pieces with a band-saw
- Bone marrow is removed with a commercial oral shower in water bath

Cutting Trabeculae

- Single trabeculae are cut out under a light microscope with a Dremel 400 DIGITAL hand milling tool and a diamond dental drill (Dental Drill by MF-Dental / cylinder pointed, ArtNr.: 885-010)

- Enough bone mass must be present at the top and bottom region of the sample for embedding
- Tweezers are used to fix the bone slice during milling for easier handling
- A pipette with HBSS helps to clear bone remnants for better vision during milling

Size Measurement Of Trabeculae

- Length, hight and width are measured
- The Micro CT can be used
- Alternatively, the Zeiss Axio Imager light microscope and the the AxioCam MRc5 can be used

Embedding

- Samples have to be embedded in order to place them within the sample holder of the tensile testing device
- silicone forms are produced (see figure 15) with a sample negative made out of epoxy. Silicone "picodent twinsil® 22" with a shore hardness of 22 is used, as the forms have to be flexible for embedding [63].
- Trabeculae have to be placed in the silicone forms as shown in figure 15. It is necessary that the trabeculae is aligned in axis.
- Thus, the Zeiss Axio Imager light microscope is used. With the z-position function of the microscope it can be checked that the trabeculae is placed in the correct high.
- It is necessary to ensure that the epoxy resin does not get in contact with the trabeculae since this would influence the results of the test. This is assured by protecting this region with plasticine.
- The bone remnants at both ends of the trabeculae are embedded between two epoxy resin glue drops. A "UHU plus Endfest 2-K-Epoxidharzkleber" is used for this step. After mixing the epoxy glue a drop of Universal-color paste in deep black (RAL 9005) is added and mixed in, to reduce the reflections during video recording.

- The epoxy is put into the in the vacuum desiccator for about 1 min to remove air and improve its rigidity.
- Then, a drop of the epoxy is placed at each end into the form. Under the microscope it is verified that no epoxy reached the trabecular shaft.
- After 16 hours of drying at room temperature the samples are taken out of the forms. It is important to ensure that the samples are not bent or deformed. Remnants of the plasticine must be removed very carefully from the trabecular shaft.
- It was noticed that the silicone forms loose there ideal shape after using them more than 3 time. So they have to be replaced regularly.

Storage of bone and samples

- Bone and single trabeculae have to be stored in between preparation steps as the protocol takes more than one day to carry out.
- Bone slices are wrapped in a cloth soaked with HBSS and samples get dipped into HBSS and put into a small container and stored in the freezer at -18 degrees.

Fluorescent Labelling

- Used chelating agents: 5 x 10^{-4} M Alizarin Red S[28] (A) and 5 x 10^{-4} M Calcein[29] (C) [68], [65]
- For each agent the powder (0.1711 g (A) and for 0.312 g (C))gets weighted into 1 liter distilled water and put on a magnet stirrer for 15 minutes.
- The mixed solutions and the powder are stored in glass bottles in the fridge wrapped in tinfoil.
- Samples get stained with A after preparatation and before testing. And with Calcein after testing.
- Therefore, the samples are put into a Petri dish or another small cup which get filled with the chelating agents.
- The Petri dish gets covered with tinfoil and is put into the vacuum desiccator for 4 hours.

[28] Sigma-Aldrich, Saint Louis, MO, USA, Product number: A5533
[29] Sigma-Aldrich, Saint Louis, MO, USA, Product number: C0875

- Afterwards samples are washed 3 times with distilled water.
- For further steps the samples need to be stored in HBSS

Fatigue Test Of Singe Trabeculae

SEL mini-001 setup 14

Specification	**Value**
Channel of control	position
Frequency [Hz]	10
Number Of Blocks	1
Offset	0
Min./Max. Load [N]	-10/+10
Min./Max. Position [mm]	-3/+3
Tuning Kpp	1.5
Tuning Kpv	1.5
Tuning Tiv [ms]	12

Table 14: Test specifications

Settings:

Parameter	**Value**	**Context**
Profile	Sinusoidal	
Amplitude [mm]	0.05	
Frequency [Hz]	1	
Preload [N]	1 - 1.3*	$V_{trab} > 1.5$ x 10^7 μm^3
	0.8 - 1.1*	$V_{trab} < 1.5$ x 10^7 μm^3
NoC	1500	no to little damage
	2100	starting microdamage
	3000	ensured mircodamage

Table 15: Final test parameters
* value for small and large trabeculae, were increased for 0.1 N after every 1000 cycle

CLSM Imaging

- Fist samples got stained for the second time with Calcein (see above).
- Afterwards, samples get embedded and fixed with epoxy resin glue (UHU plus Endfest 2-K-Epoxidharzkleber) to an object slide and dry for 16 hours.

- .Then they get fixed on the slide of the ultramiller Leica SP2600 [76] and with the following settings the redundant epoxy resin get milled:

Specification	**Value**
Feed (Premiller) [μm]	4
Feed (Finishing miller) [μm]	1-2
Retract [n]	50
Cut [mm/s]	1-2
Return [mm/s]	40
Speed [rpm]	1200

Table 16: Leica Ultramilling settings

- Under the microscop it is checked if the trabeculae is alreday visible. If so, the pre-miller get changed to the finishing miller.
- After every 5μm sample is checked under the microscope if microdamage is already visible. The Zeiss Axio Imager light microscope is used with the filter for Alexa Four 488 which induces Calcein fluorescence.
- After stopping of milling the finishing miller is cleaned with acetone.
- Samples get polished (First sandpaper in different grits (1000 and 2400), afterwards with Buehler MetaDi monocrystalline diamond suspensions of 3 μm, 1 μm and 0.25 μm with textile polishing cloths. Between the different suspensions the samples were cleaned in a Sonorex Super ultrasonic bath for 3 minutes).
- Then CLSM analysis is stated:
- Samples get imaged at 10x, 20x and 100x magnification (100x objective is oil immersed. Therefore samples got further prepared with mounting medium[30] and coverslip. The cover slip is fixed with clear nail polish.)
- The following settings were used for images acquisition 6:

[30] Sigma-Aldrich Fluoromount^{TM} Aqueous Mounting Medium

10x objective	EC Plan-Neofluar 10x/0.30 M27
20x objective	EC Plan-Neofluar 20x/0.50 M27 objective
100x objective	Plan-Apochromat 100x/1.40 Oil objective
Scan Mode	Stack
Zoom	0.5-1
Pixel dwell	1.27 μm
Laser 1	555 nm
Intensity Laser 1	800%
Laser 2	488 nm
Intensity Laser 2	800%
Filter Ch1	BP 420-550
Filter Ch2	LP 560
Pinhole	70 μm
Digital gain	1

Table 17: CLSM settings

Image Analysis

Software ImageJ[31][77] is used.

3-Dimensional Analysis

- The z-stacks are imported into ImageJ and converted into grayscale: File - Import - Image sequence... - Convert to 8-bit Grayscale
- Images get deinterleaved: Image - Stacks - Tools - Deinterleave
- Red and Blue channel get closed.
- With the polygon selection tool the region of interest (ROI) is determined for the first image in the sequence and added to the ROI Manager: Choose ROI with polygon tool - Analyse - Tool - ROI Manager - Add[t].
- The same was done for the last image in the sequence. After that the ROI is interpolated: ROI Manager - Moore - Interpolate ROI (Save ROI)
- The area is measured (strg+m) and saved.
- Then the Histogram macro is used which can be found in the Appendix: Plugins - Macro - Run - Histogram.txt.

[31] ImageJ is an open source Java image processing program

- Results are exported into a excel sheet and a threshold (Triangle) is determined for the analysis of the gray values: Image - Adjust - Threshold - Triangle/Stack histogram.
- Afterwards the histogram data is analysed with the given threshold and the counter sum gives are converted from pixel to μm^2 the damaged area.
- With hight of z-stack the volume can be calculated (V_{tot} [μm^3]).
- For samples that contain linear cracks and also diffuse damage the damaged volume (V_{tot}) had to be assigned to the different types. This is made by segmenting a new ROI for the linear cracks since these are easier to mark out than diffuse damage. Linear cracks are assumed as elliptical. Therefore the ROI is set as an ellipse around the linear crack. Again, the Histogram Marco is executed and the counts for the linear cracks are summarised after thresholding. With this the damaged volume (V_{lin}) which is assigned to linear cracks is known. The diffuse damaged volume (V_{diff}) is gained by subtraction the counts of linear damaged volume of the count of total damaged region.
- Therefore following parameters are known:

Specification	**Name**	**Calculation**
Lin.Cr. [#]	Number of Linear Microcracks	ImageJ
Diff. [#]	Number diffuse damaged areas	ImageJ
V_{trab} [μm^3]	Volume of trabecula	ImageJ
V_{tot} [μm^3]	Volume of total damaged area	ImageJ
V_{lin} [μm^3]	Volume of linear cracks	ImageJ
V_{diff} [μm^3]	Volume of diffuse damage	ImageJ
Dam.Den [%]	Total damaged area density	V_{tot} / V_{trab}
Lin.Cr.Den [%]	Linear Crack Density	V_{lin} / V_{trab}
Diff.Den [%]	Diffuse Damage Density	V_{diff} / V_{trab}

Table 18: Parameters for 3-dimensional analysis

2-Dimensional Analysis

- Two representative images of a sample are taken from the z-stack. Each of this images is analysed separately.
- Analysis is done as for volumetric analysis except ROI only must be defined for one single image (no interpolation necessary).

- Afterwards the linear cracks are measured with the "elliptical selection" tool.
- For purposes of comparison the length was measured from tip to tip and the width with the "straight line" tool. For the elliptical selection the histogram was again executed to gain the counts for the linear cracks. Again, these counts are subtracted from the total amount to gain the area of diffuse damage.
- This procedure was executed for the second image of the z-stack to get more data.
- The following parameter were gained:

Specification	**Name**	**Calculation**
A_{trab} [μm^2]	Area of Trabeculae (ROI)	ImageJ
Lin.Cr. [#]	Number of Linear Microcracks	ImageJ
Diff. [#]	Number diffuse damaged areas	ImageJ
Lin.Cr.X.Length [μm]	Length of linear microcrack Nr.X	ImageJ
Lin.Cr.X.Width [μm]	With of linear microcrack Nr.X	ImageJ
Lin.Cr.X.Area [μm^2]	Area of linear microcrack Nr.X	ImageJ
Lin.Cr.S.Den [$\mu m/\mu m^2$]	Linear Crack Surface Density	Lin.Cr.(Xi).Length / Area
Lin.Cr.Den.2D [%]	Linear Crack Density 2D	Lin.Cr.(Xi).Area / Area
Diff.Den.X.Area [μm^2]	Area of Diffuse Damage	ImageJ
Diff.Den.2D [%]	Diffuse Damage Surface Density 2D	Diff.S.Den / Area
Dam.Den.2D [%]	Total damaged area density 2D	Diff.Den.Area / Area

Table 19: Parameters for 2-dimensional analysis
Xi: Sum over all Linear Cracks if more than more occurs

9.2 Definition of ROI for Linear Cracks and Diffuse Damage

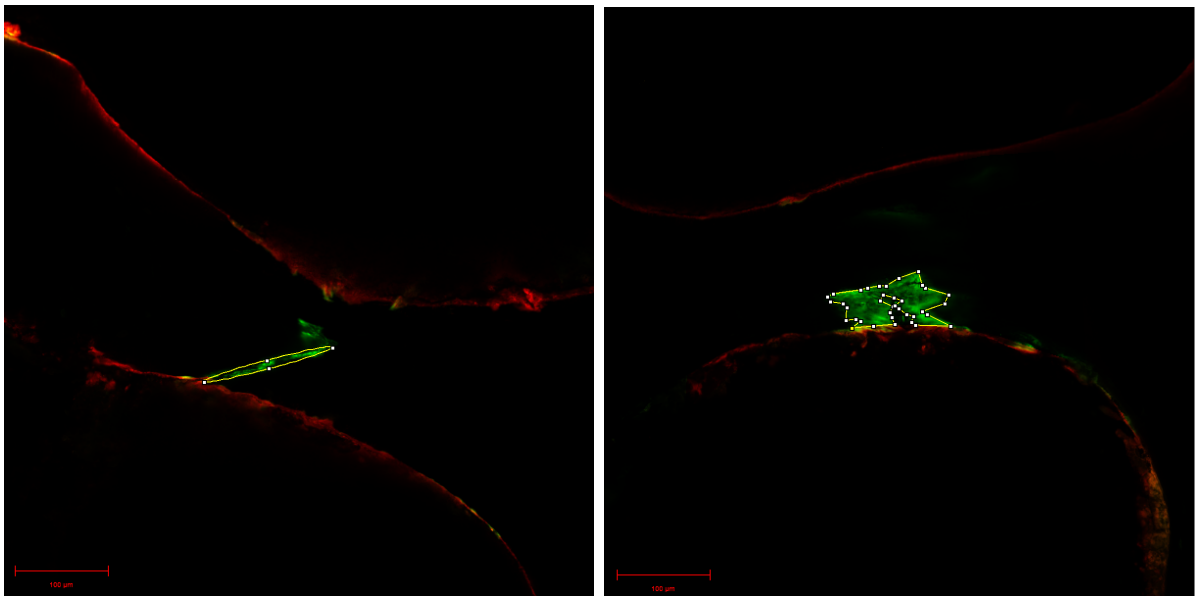

(a) Linear Crack (b) Diffuse Damage

Figure 46: Definition of region of interest for linear crack and diffuse damage in ImageJ for image analysis

9.3 Results in Detail

9.3.1 Elastic Modulus

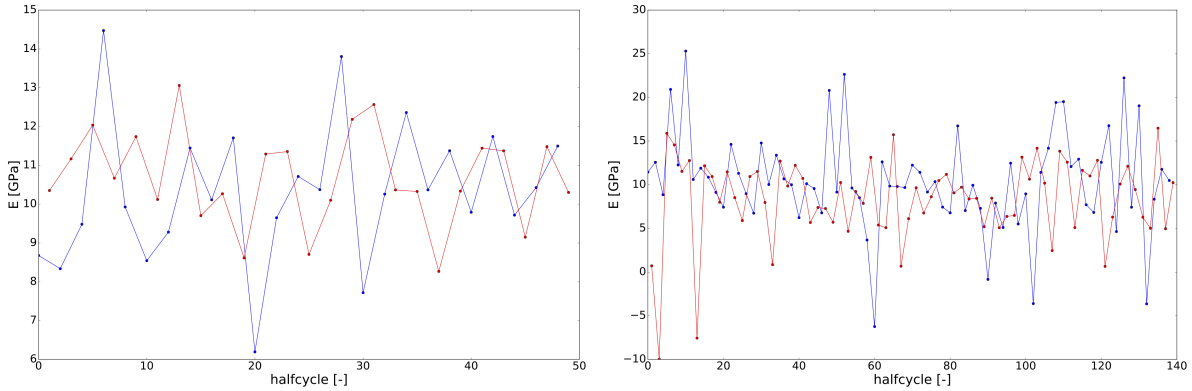

(a) First Set (b) Last Set

Figure 47: Elastic modulus sample B2

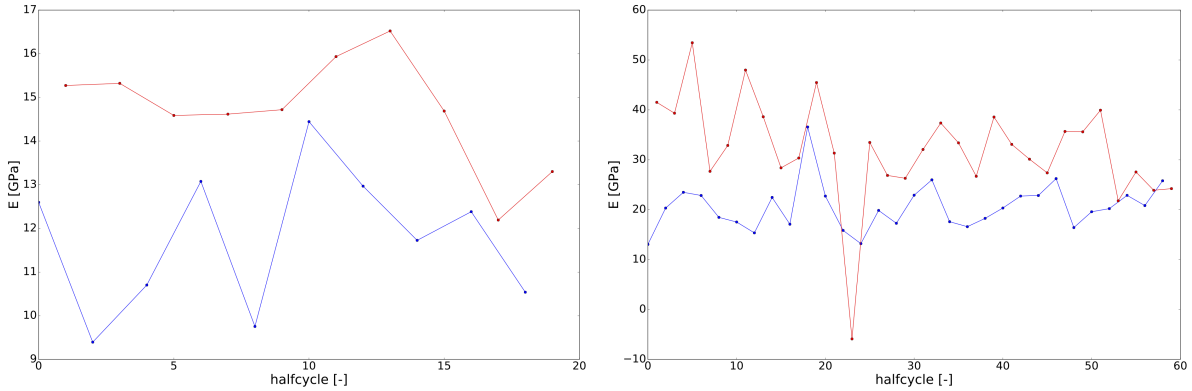

(a) First set (b) Last set

Figure 48: Elastic modulus sample B7

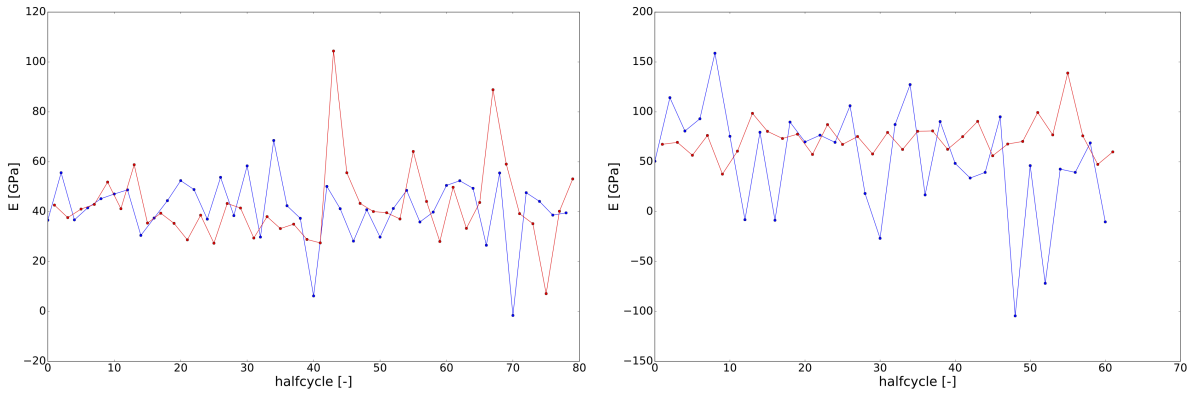

(a) First set (b) Last set

Figure 49: Elastic modulus sample D1

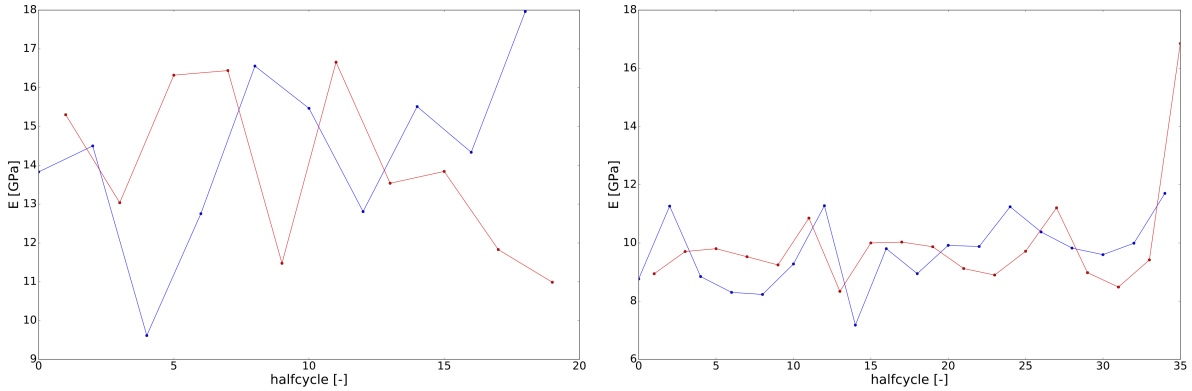

(a) First set (b) Last set

Figure 50: Elastic modulus sample E3

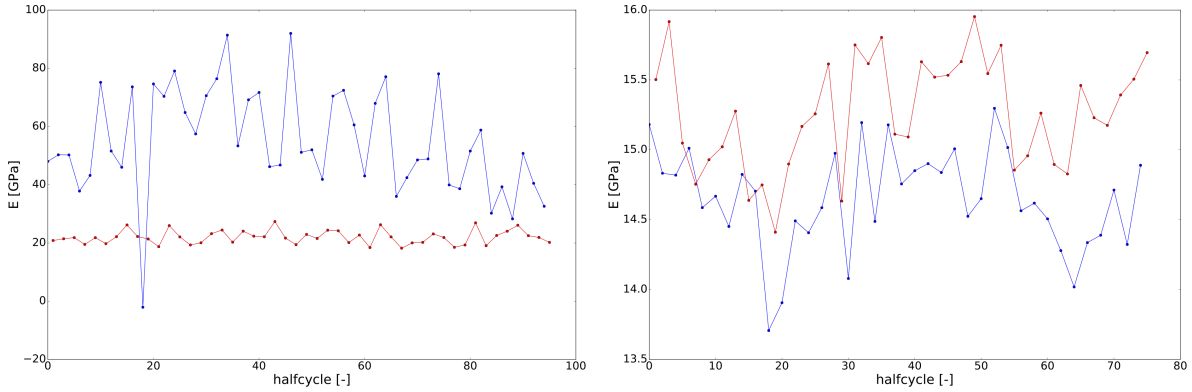

(a) First set (b) Last set

Figure 51: Elastic modulus sample F3

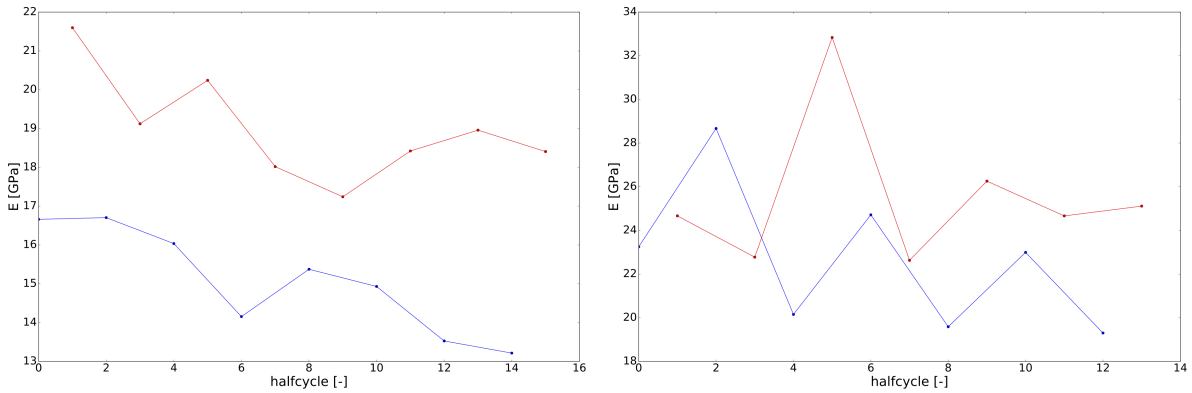

(a) First set (b) Last set

Figure 52: Elastic modulus sample G1

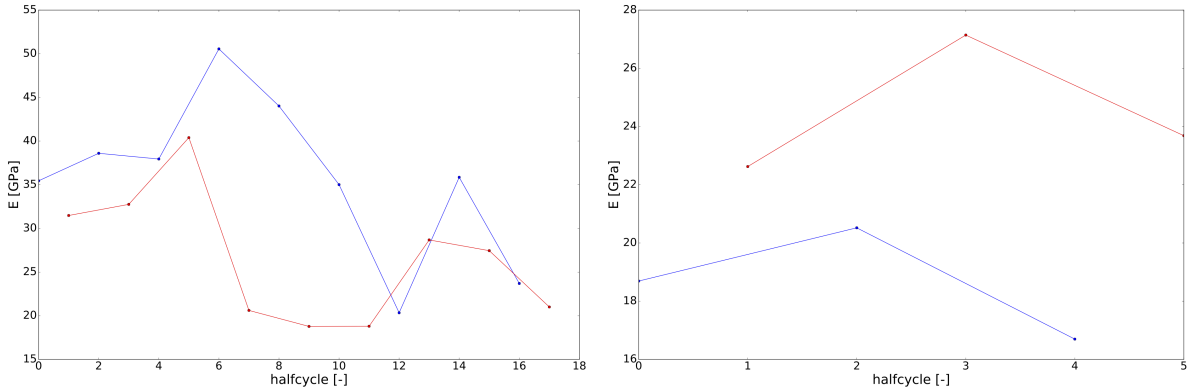

(a) First set (b) Last set

Figure 53: Elastic modulus sample G7

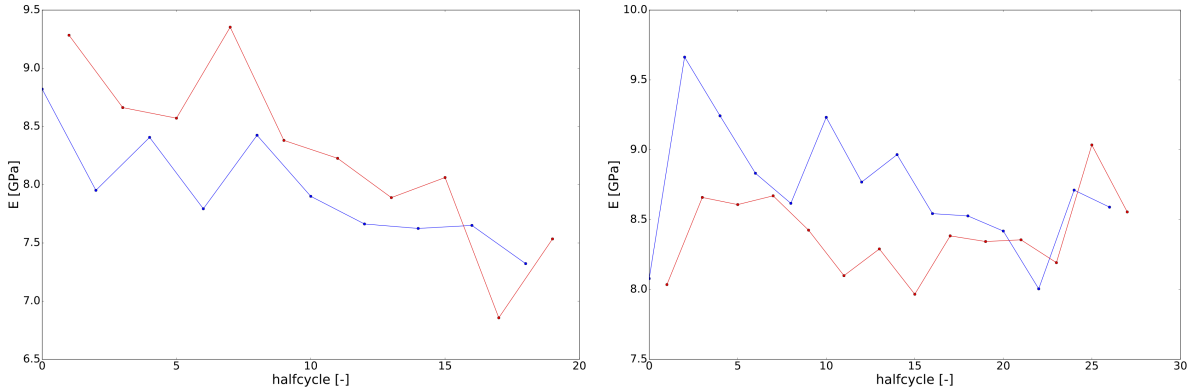

(a) First set (b) Last set

Figure 54: Elastic modulus sample I1

9.3.2 Stress Strain Amplitude

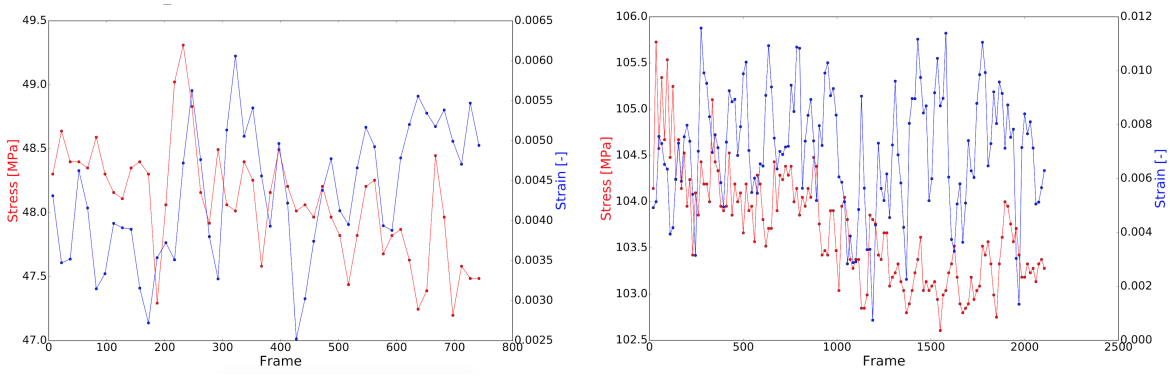

(a) First set (b) Last set

Figure 55: Stress and strain amplitude sample B2

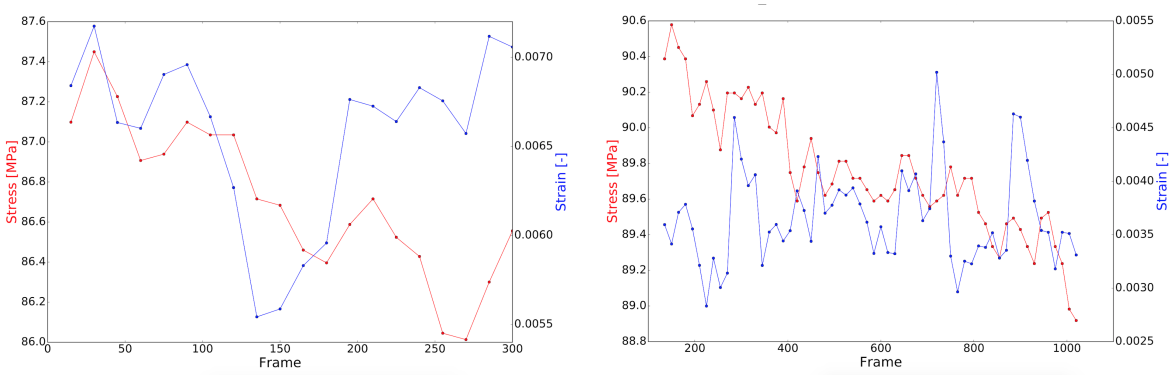

(a) First set (b) Last set

Figure 56: Stress and strain amplitude sample B7

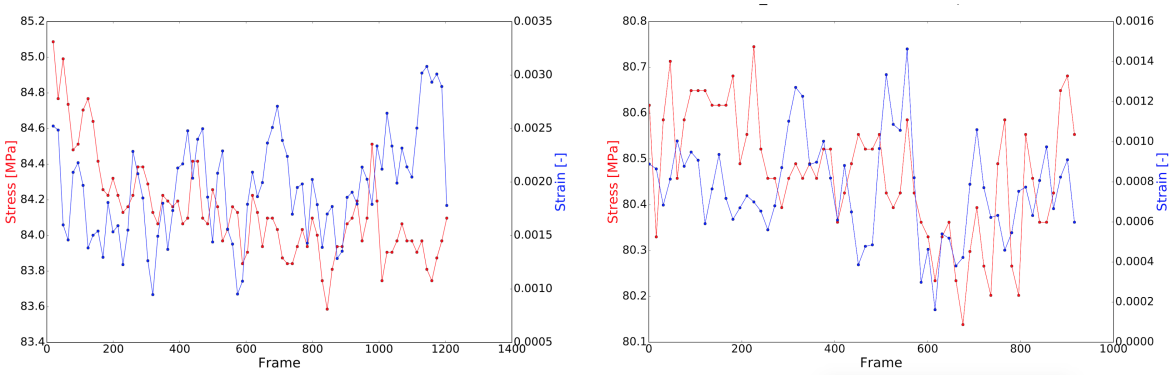

(a) First set (b) Last set

Figure 57: Stress and strain amplitude sample D1

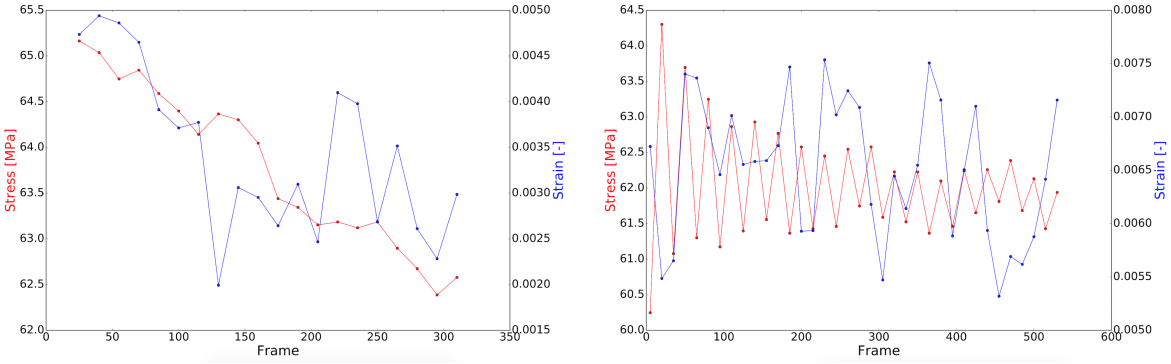

(a) First set (b) Last set

Figure 58: Stress and strain amplitude sample E3

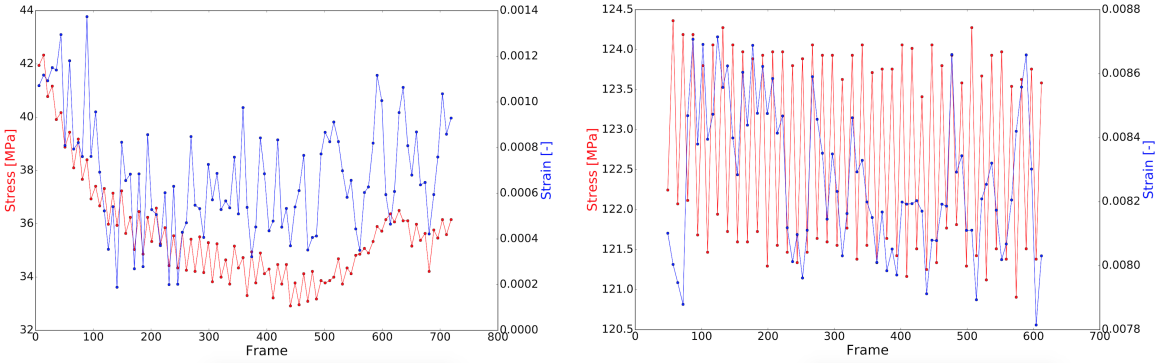

(a) First set (b) Last set

Figure 59: Stress and strain amplitude sample F3

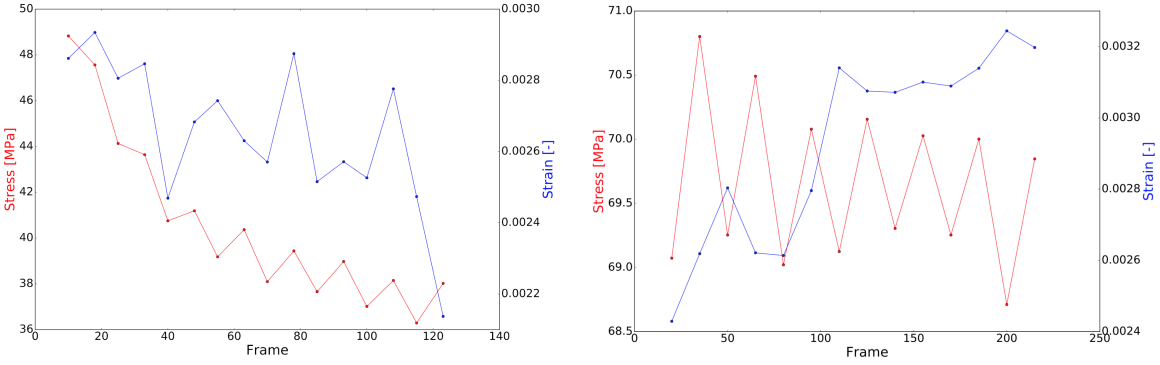

(a) First set (b) Last set

Figure 60: Stress and strain amplitude sample G1

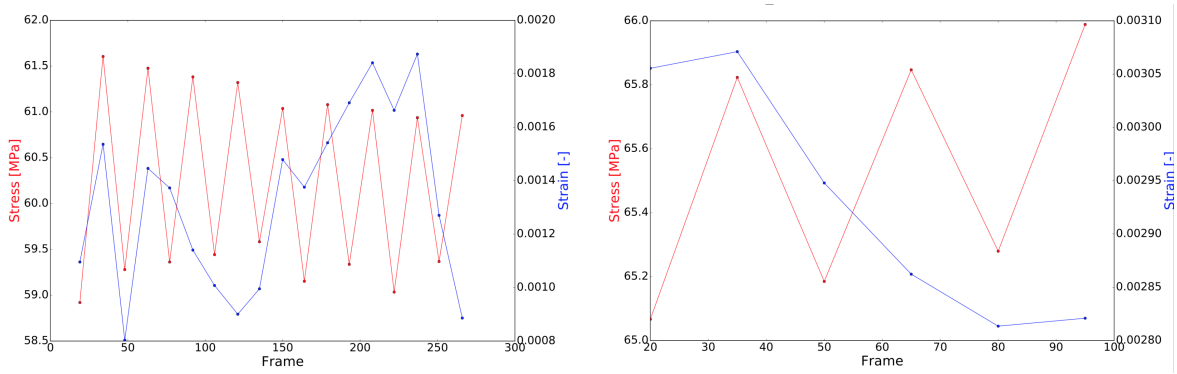

(a) First set (b) Last set

Figure 61: Stress and strain amplitude sample G7

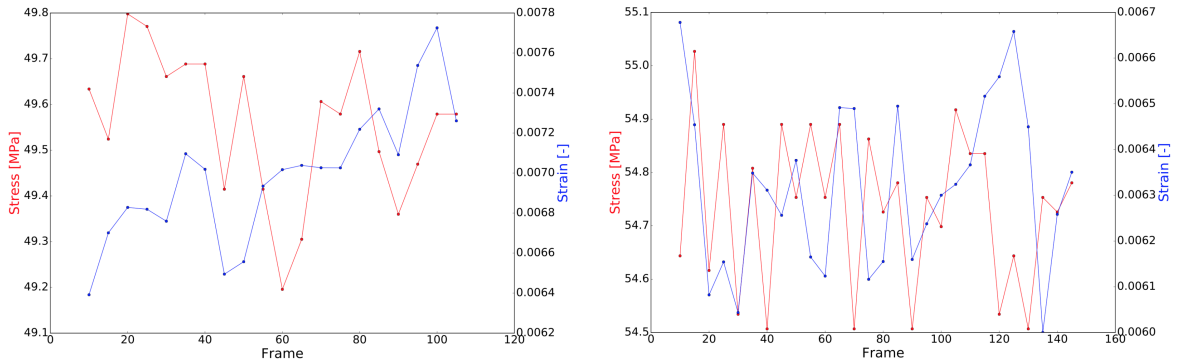

(a) First set (b) Last set

Figure 62: Stress and strain amplitude sample I1

9.3.3 Stress-Strain-Data

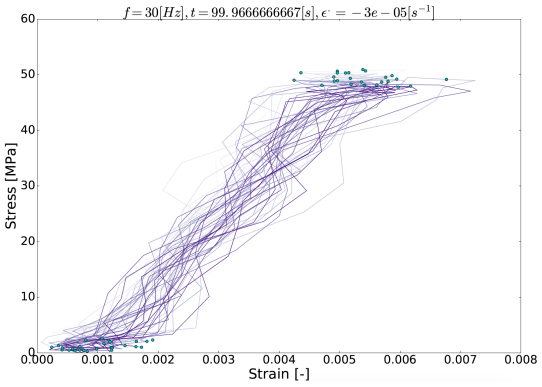

(a) First set

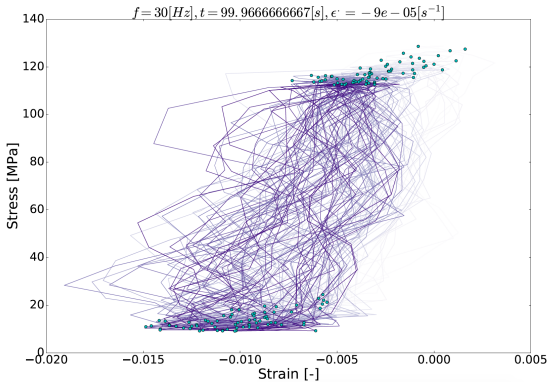

(b) Last set

Figure 63: Stress-Strain-Data for sample B2

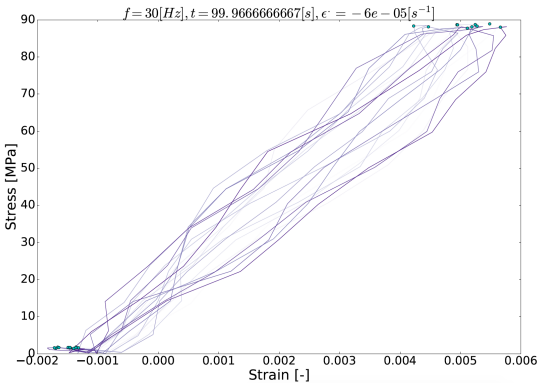

(a) First set

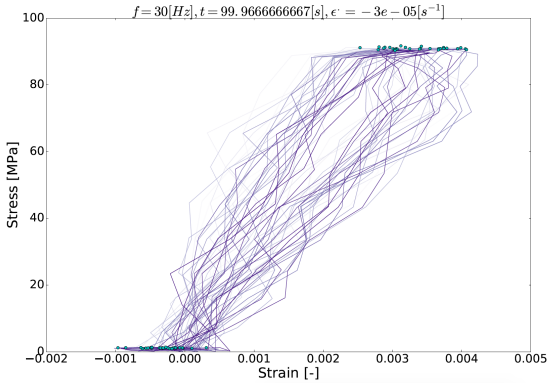

(b) Last set

Figure 64: Stress-Strain-Data for sample B7

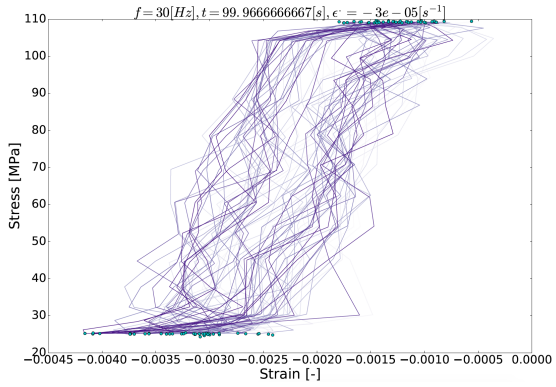

(a) First set

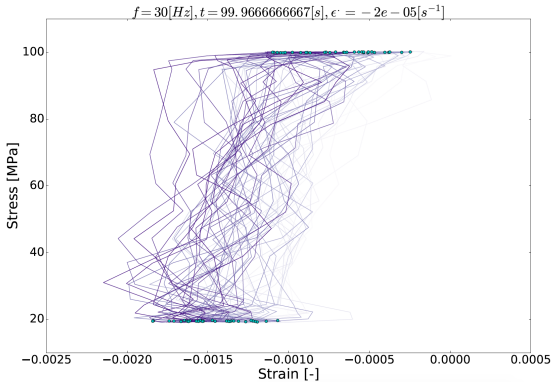

(b) Last set

Figure 65: Stress-Strain-Data for sample D1

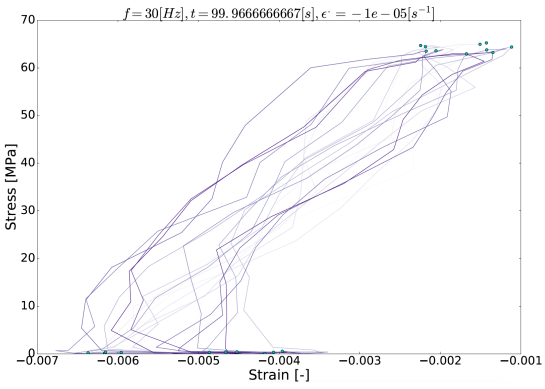

(a) First set

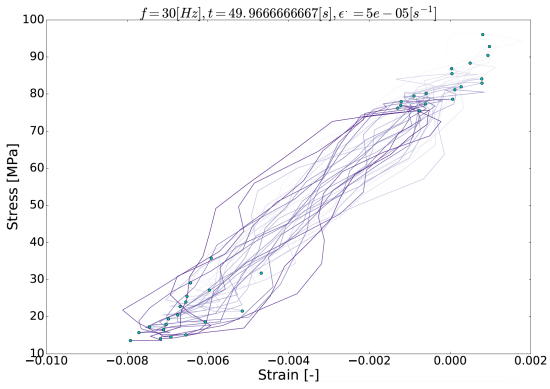

(b) Last set

Figure 66: Stress-Strain-Data for sample E3

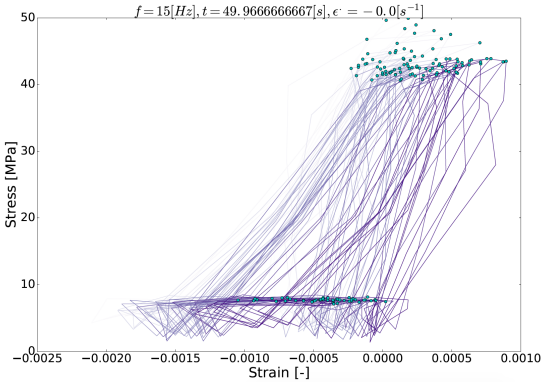

(a) First set

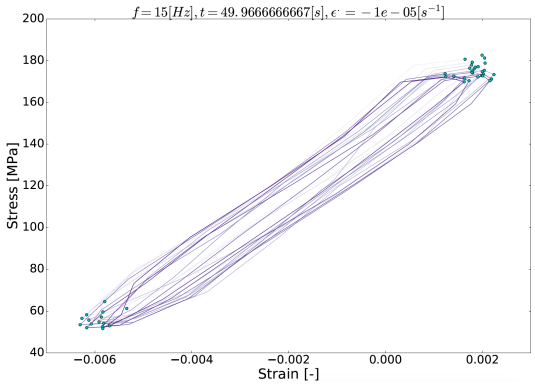

(b) Last set

Figure 67: Stress-Strain-Data for sample F3

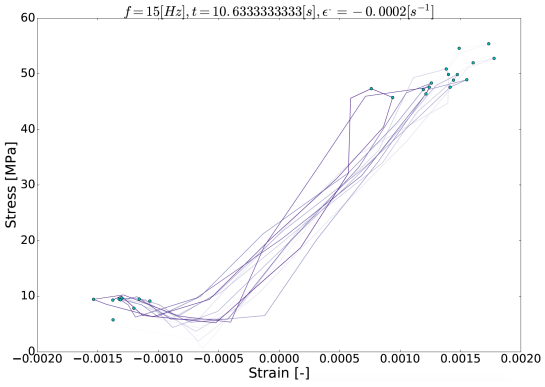

(a) First set

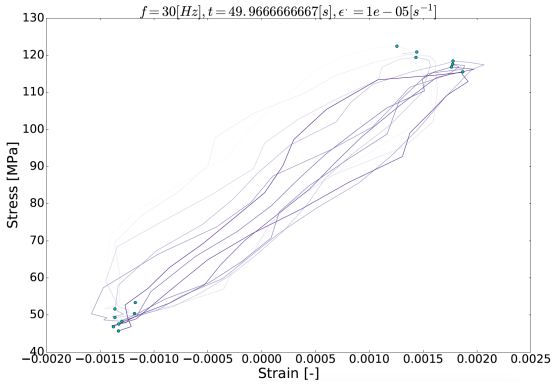

(b) Last set

Figure 68: Stress-Strain-Data for sample G1

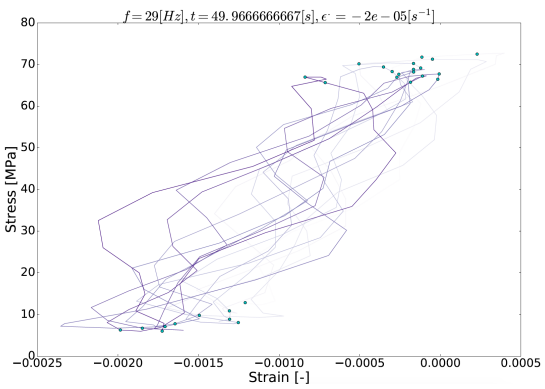

(a) First set

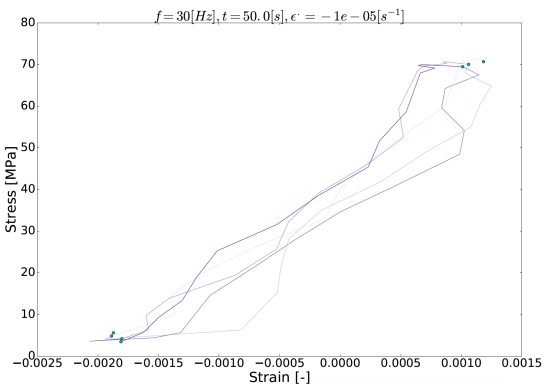

(b) Last set

Figure 69: Stress-Strain-Data for sample G7

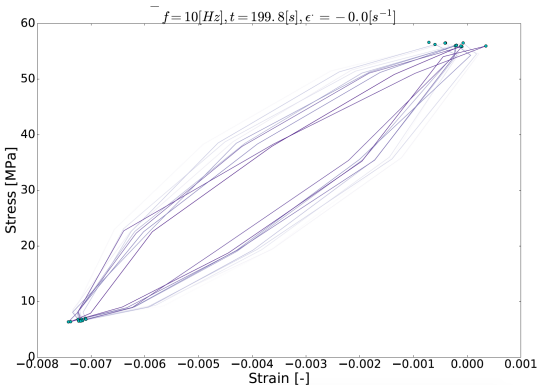

(a) First set

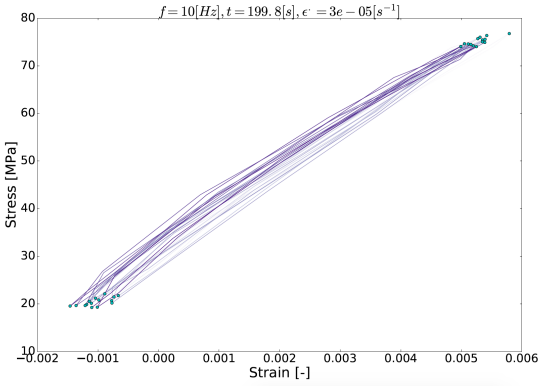

(b) Last set

Figure 70: Stress-Strain-Data for sample I1

9.3.4 CLSM Images

Reference Samples

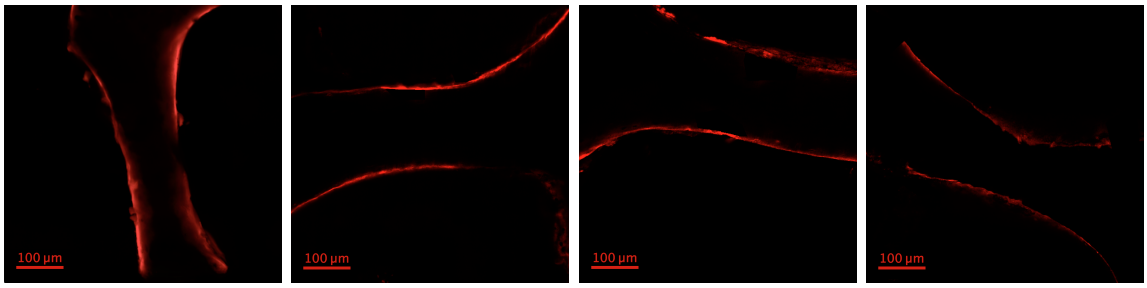

(a) Sample N1 (b) Sample N2 (c) Sample N3 (d) Sample N4

Figure 71: Reference samples N1 N2, N3, N4 with 20x magnification

1500 cycles

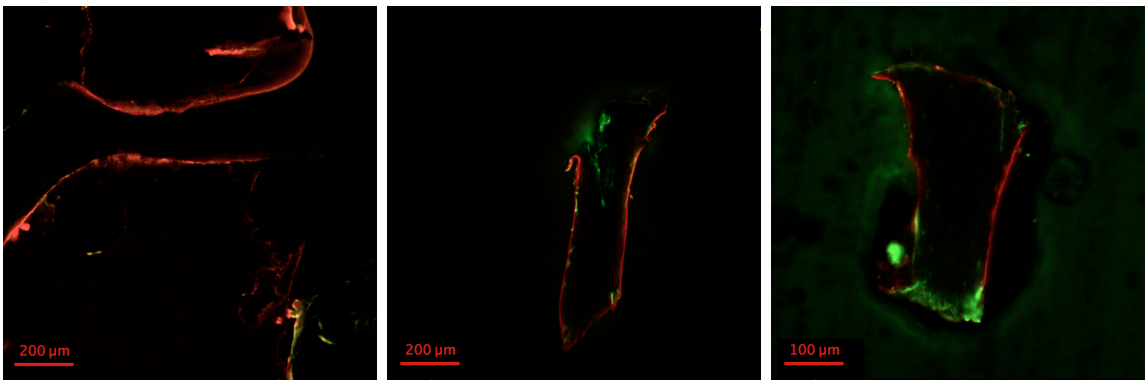

(a) Sample F2 (b) Sample S1 (c) Sample S2

Figure 72: Samples F2, S1, S2 with 20x magnification

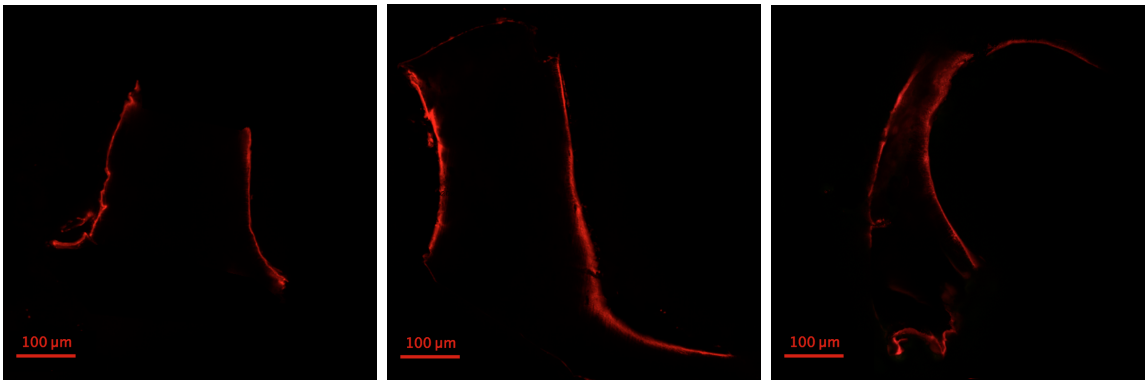

(a) Sample S3 (b) Sample 8a (c) Sample 8b

Figure 73: Samples S3, 8a, 8b with 20x magnification

2100 cycles

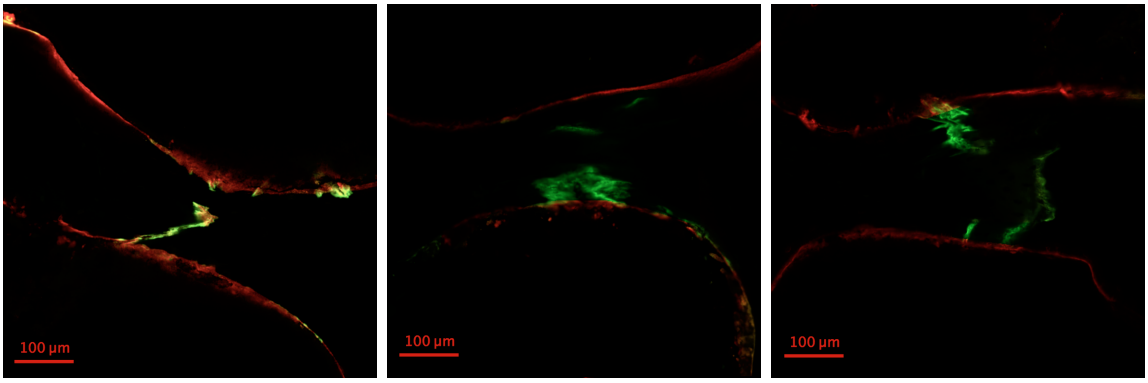

(a) Sample J2 (b) Sample J4 (c) Sample H3

Figure 74: Samples J2, J4 and H3 with 20x magnification

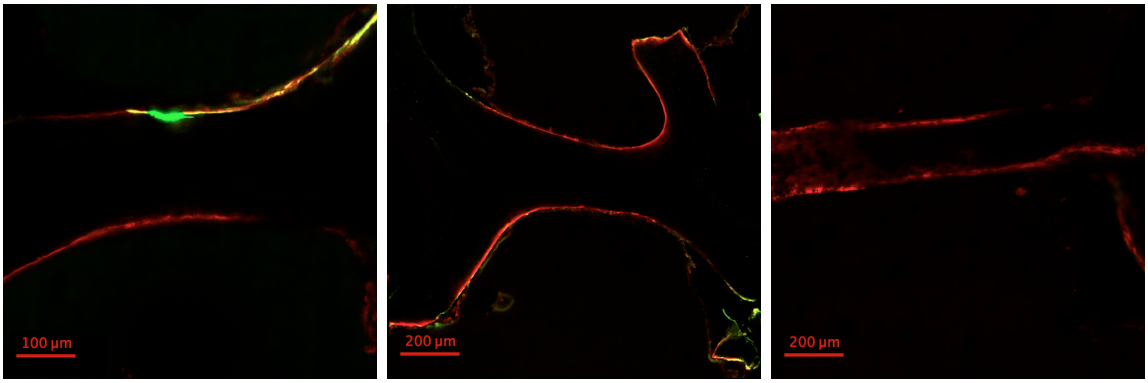

(a) Sample G7 (b) Sample F1 (c) Sample G6

Figure 75: Sample G7 with 20x magnification, Sample F1 and G6 with 10x magnification

3000 cycles

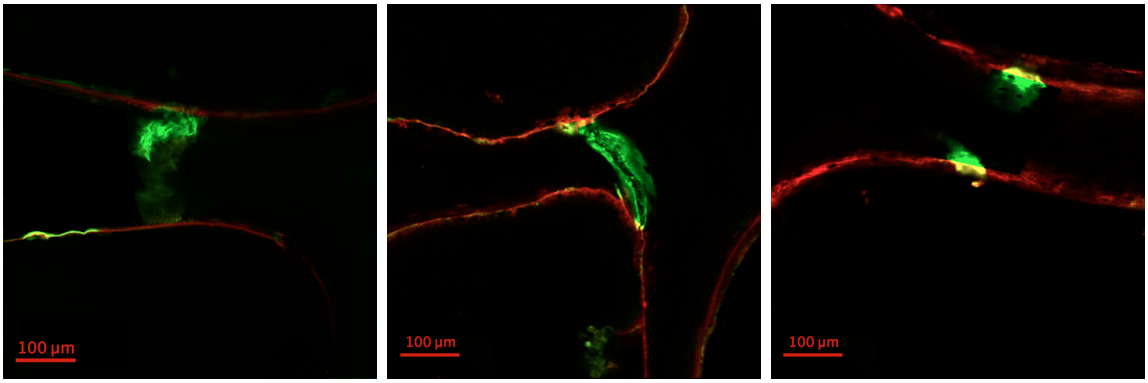

(a) Sample D1 (b) Sample E3 (c) Sample G1

Figure 76: Sample D1 and G1 with 20x magnification, Sample E3 with 10x magnification

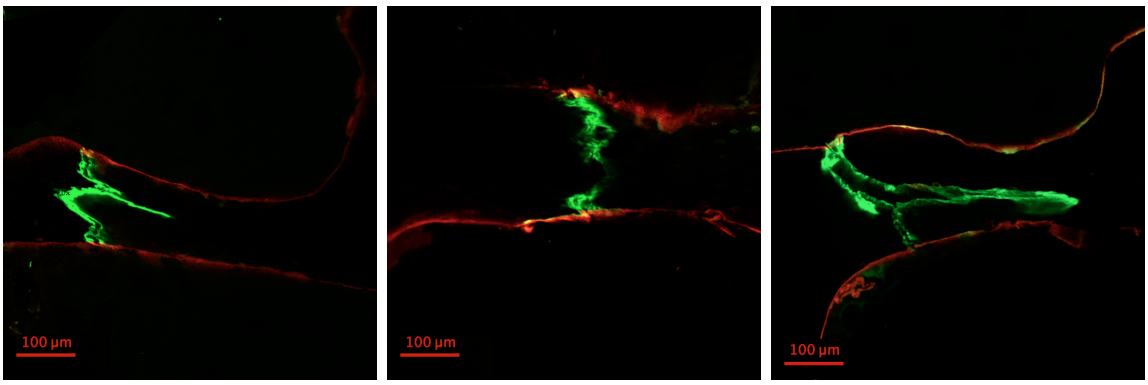

(a) Sample G2 (b) Sample G8 (c) Sample I1

Figure 77: Sample G2, G8 and I1 with 20x magnification

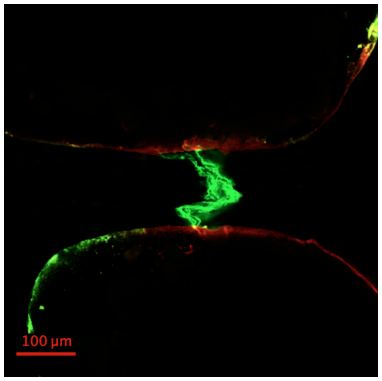

(a) Sample J3

Figure 78: Sample J3 with 20x magnification

9.3.5 Maximum Intensity Projection Images

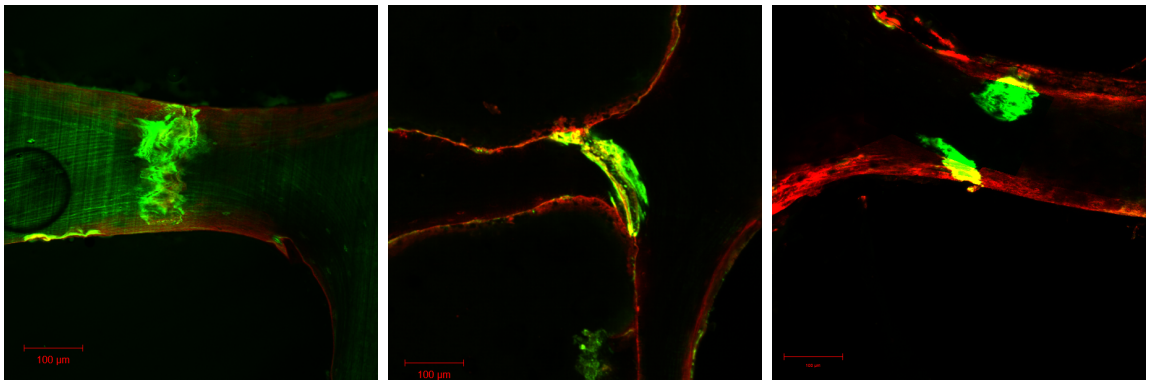

(a) Sample D1 (b) Sample E1 (c) Sample G1

Figure 79: Max. Intensity Projection for Sample D1, E1, G1

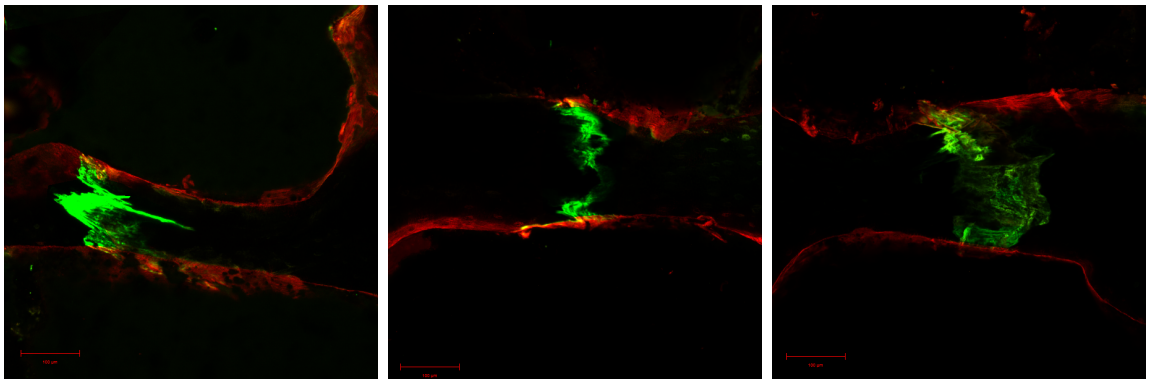

(a) Sample G2 (b) Sample G8 (c) Sample H3

Figure 80: Max. Intensity Projection for Sample G2, G8, H3

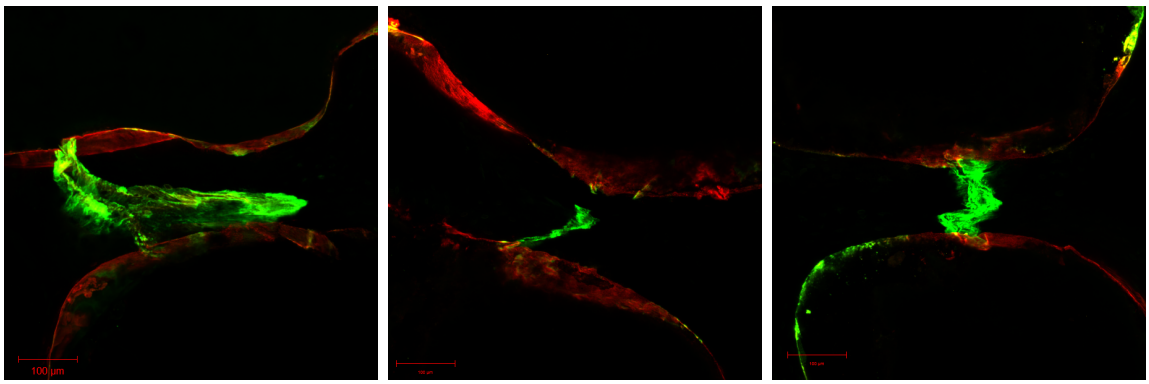

(a) Sample I1 (b) Sample J2 (c) Sample J3

Figure 81: Max. Intensity Projection for Sample I1, J2, J3

(a) Sample J4 (b) Sample S1 (c) Sample S2

Figure 82: Max. Intensity Projection for Sample J4, S1, S2

9.3.6 Additional parameters for 2-dimensional analysis

		Lin.Cr. #	Diff.Dem. #	Lin.Cr.1.Length [μm]	Lin.Cr.1.Width [μm]	Lin.Cr.1.Area [μm^2]	Lin.Cr.2.Length [μm]	Lin.Cr.2.Width [μm]	Lin.Cr.2.Area [μm^2]	Diff.Den.1.Area [μm^2]	Diff.Den.2.Area [μm^2]
1500 cycles	Slice										
S1	1	1	1	180	6	847.80	0	0	0	1000	0
	2	1	1	100	7	549.50	0	0	0	2500	0
S2	1	1	1	93	8	584.04	0	0	0	2103	0
	2	1	1	93	8	584.04	0	0	0	2802.96	0
8a	1	0	0	0	0	0	0	0	0	0	0
	2	0	0	0	0	0	0	0	0	0	0
8b	1	0	0	0	0	0	0	0	0	0	0
	2	0	0	0	0	0	0	0	0	0	0
F2	1	0	0	0	0	0	0	0	0	0	0
	2	0	0	0	0	0	0	0	0	0	0
S3	1	0	0	0	0	0	0	0	0	0	0
	2	0	0	0	0	0	0	0	0	0	0
2100 cycles											
G7	1	1	1	0	0	0	0	0	0	637	0
	2	1	1	0	0	0	0	0	0	1040	0
H3	1	2	0	99	5	388.57	39	8	244.92	0	0
	2	2	0	178	10	1397.30	33	10	259.05	0	0
J2	1	1	1	176	8	1105.28	0	0	0	301	0
	2	1	1	175	12	1648.50	0	0	0	3588.86	0
J4	1	2	1	90	7	494.55	71	11	613.08	2434.30	0
	2	2	1	98	12	923.16	75	16	942	3764	0
F1	1	0	0	0	0	0	0	0	0	0	0
	2	0	0	0	0	0	0	0	0	0	0
G6	1	0	0	0	0	0	0	0	0	0	0
	2	0	0	0	0	0	0	0	0	0	0
3000 cycles											
G2	1	1	1	130	4	408.2	0	0	0	7704	0
	2	2	1	121	6	569.91	30	5	117.75	257.07	0
J3	1	0	1	0	0	0	0	0	0	4301	0
	2	0	1	0	0	0	0	0	0	3700	0
I1	1	0	1	0	0	0	0	0	0	4000	0
	2	0	1	0	0	0	0	0	0	4900	0
G8	1	0	1	0	0	0	0	0	0	2675	0
	2	0	1	0	0	0	0	0	0	2533	0
G1	1	0	2	0	0	0	0	0	0	2826	1497
	2	0	2	0	0	0	0	0	0	1160	3209
E3	1	0	1	0	0	0	0	0	0	2500	0
	2	0	1	0	0	0	0	0	0	2346	0
D1	1	0	1	0	0	0	0	0	0	7661	0
	2	2	1	84	8	527.52	70	6	329.70	1288	0

Table 20: p-values as indicator of significance for Lin.Cr.Den(2D), Diff.Den(2D), Dam.Den(2D) and Lin.Cr.Den.S over all cycle set, between 1500 and 2100 and between 2100 and 3000, significant difference for $p<0.05$

9.3.7 Display of Statistical Analysis

3D		**2D**	
1500:2100:3000		**1500:2100:3000**	
Variable	p-value	Variable	p-value
Lin.Cr.Den	0.507	Lin.Cr.Den.2D	0.092
Diff.Den	0.076	Diff.Den.2D	0.001
Dam.Den	0.090	Dam.Den.2D	0.001
-	-	Lin.Cr.Den.S	0.074
1500:2100		**1500:2100**	
Lin.Cr.Den	0.372	Lin.Cr.Den.2D	0.169
Diff.Den	0.393	Diff.Den.2D	0.449
Dam.Den	0.393	Dam.Den.2D	0.211
-	-	Lin.Cr.Den.S	0.260
2100:3000		**2100:3000**	
Lin.Cr.Den	0.290	Lin.Cr.Den.2D	0.085
Diff.Den	0.045	Diff.Den.2D	0.001
Dam.Den	0.063	Dam.Den.2D	0.005
-	-	Lin.Cr.Den.S	0.058

Table 21: p-values as indicator of significance for Lin.Cr.Den(2D), Diff.Den(2D), Dam.Den(2D) and Lin.Cr.Den.S over all cycle set, between 1500 and 2100 and between 2100 and 3000, significant difference for $p<0.05$

3D			
	p-values		
	1500 cycles	**2100 cycles**	**3000 cycles**
Lin.Cr.Den : Diff.Den	0.818	1	0.001
Lin.Cr.Den : Dam.Den	0.18	0.068	0.018
Diff.Den : Dam.Den	0.18	0.109	0.180
2D			
	p-values		
	1500 cycles	**2100 cycles**	**3000 cycles**
Lin.Cr.Den.2D : Diff.Den.2D	0.671	0.847	0.001
Lin.Cr.Den.2D : Dam.Den.2D	0.068	0.028	0.001
Diff.Den.2D : Dam.Den.2D	0.068	0.028	0.109

Table 22: Comparison of variables (Lin.Cr.Den(2D), Diff.Den(2D), Dam.Den(2D)) to each other for every 1500, 2100 and 3000 cycles, significant difference for $p<0.05$

	p-values		
	1500 cycles	**2100 cycles**	**3000 cycles**
Lin.Cr.Den : Lin.Cr.Den.2D	0.75	0.301	0.971
Diff.Den : Diff.Den.2D	0.892	1	0.003
Dam.Den : Dam.Den.2D	0.892	0.462	0.001

Table 23: Comparison between 2D and 3D data with p-vale as indicator of significance, significant difference for $p<0.05$

9.4 Template for Sample Holder

Technical drawing of the sample holder for reference:

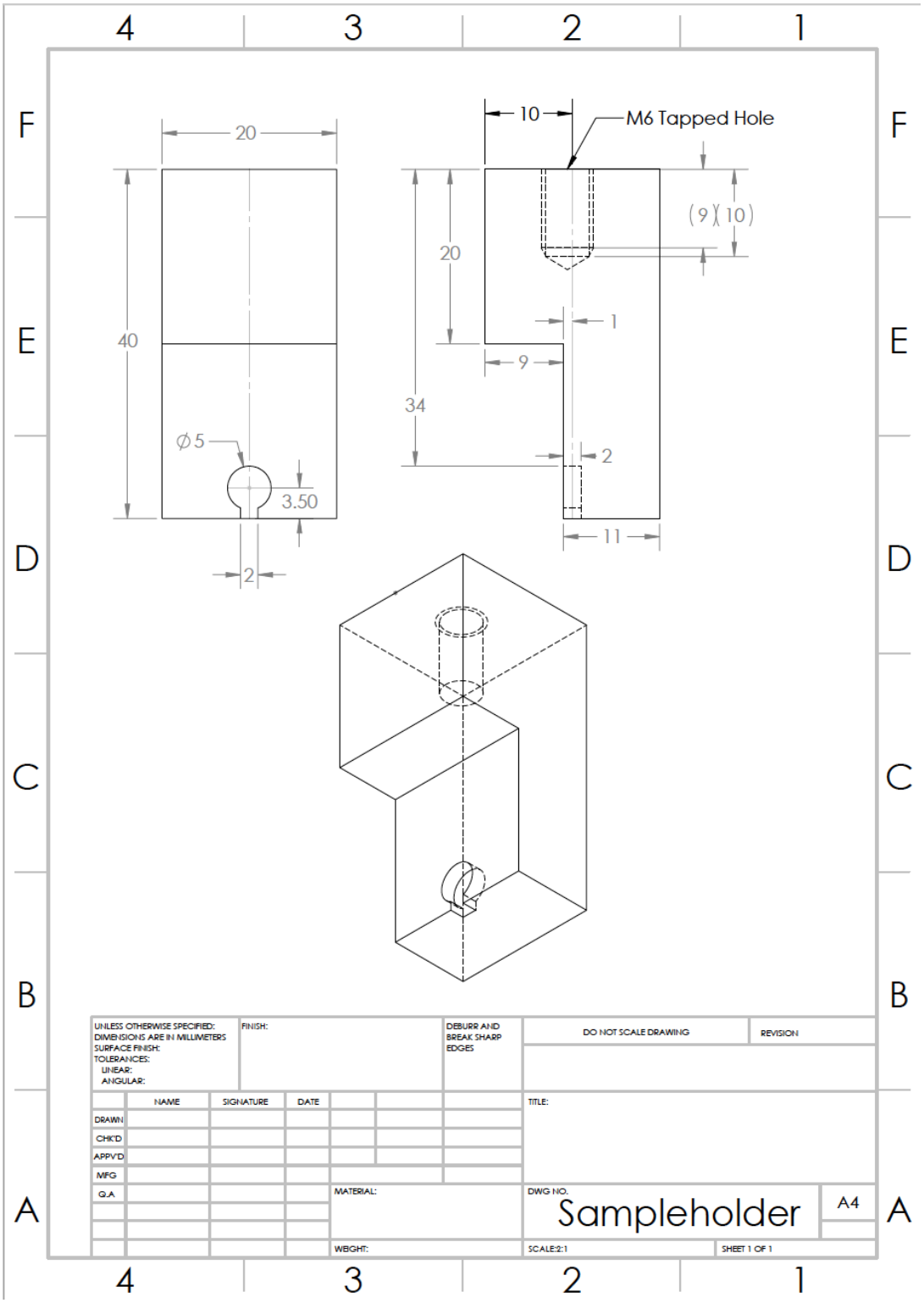

Figure 83: Template for sample holder

9.5 Histogram

```
// This macro prompts for the bin count and histogram
// min and max and then writes the histogram counts of
// the current image or stack to the "Results" window.
  requires("1.34m");
  Dialog.create("Histogram Lister");
  Dialog.addNumber("Number of Bins:", 256);
  Dialog.addNumber("Histogram Min:", 0);
  Dialog.addNumber("Histogram Max:", 256);
  Dialog.show();
  nBins = Dialog.getNumber();
  hMin = Dialog.getNumber();
  hMax = Dialog.getNumber();
  row=0;
  run("Clear Results");
  if (bitDepth==32) {
       for (slice=1; slice<=nSlices; slice++) {
            if (nSlices>1) run("Set Slice...", "slice=" + slice);
            roiManager("Select", slice-1);
            getHistogram(values,counts,nBins,hMin,hMax);
            for (i=0; i<nBins; i++) {
                 if (nSlices>1) setResult("Slice", row, slice);
                 setResult("Value", row, values[i]);
                 setResult("Count", row, counts[i]);
                 row++;
            }}}
 else {
       setBatchMode(true);
       stack = getImageID();
       for (slice=1; slice<=nSlices; slice++) {
            selectImage(stack);
            if (nSlices>1) run("Set Slice...", "slice=" + slice);
            run("Duplicate...", "title=temp");
            run("32-bit");
            roiManager("Select", slice-1);
            getHistogram(values,counts,nBins,hMin,hMax);
            close();
            for (i=0; i<nBins; i++) {
                 if (nSlices>1) setResult("Slice", row, slice);
                 setResult("Value", row, values[i]);
                 setResult("Count", row, counts[i]);
                 row++;
            } } }
  updateResults()
```

List of Figures

1 Hierarchical structure of bone [20] 6
2 Anatomy of a long bone 7
3 Crosssectional view of cortical bone [22] 8
4 Schematic image of trabecular bone [22] 9
5 Examples for microdamage in compact bone 10
6 Stained microdamge by Fazzalari et al. (1998) [33] 11
7 Bone repair mechanism. 12
8 Schematic crack propagation in young and elderly samples. 15
9 Model of elastic modulus loss under fatigue loading. 16
10 Sequence of chelating agents 20
11 Light path of CLSM [61] 21
12 Influence of bone marrow on visibility of trabeculae 24
13 Cutting pattern 25
14 Setup for cutting samples 25
15 Silicone form with adjusted trabeculae 27
16 Embedding of samples 28
17 1 x 10^{-4} M Calcein Blue 31
18 5 x 10^{-4} M Calcein Blue 31
19 Comparison of spray 1 and 2 32
20 Comparison of spray 1 and 4 33
21 Schematic display of speckle pattern application 34
22 SEL mini-001servo-electric load frame with dimensions in mm [75] 35
23 Re-designed sample holders 36
24 Test setup 37
25 Sinusoidal profile for fatigue testing at 1 Hz with an amplitude of 25 μm. 37
26 Original and adapted profile 39
27 Offset at test start 40
28 Samples fixed with epoxy resin to an object slide 42
29 Grooves in sample after ultramilling 43

30 Steps of bone polishing 44
31 Surface quality after polishing with diamond suspensions (20x magnification) 44
32 Sample images with CLSM with 20x magnification before and after polishing 45
33 Determination of deformation with digital image correlation 47
34 Definition of Region Of Interest (ROI) 49
35 Triangle Threshold 50
36 Sample F3 - Loading Check 55
37 Elastic modulus sample B2 56
38 Stress and strain amplitude for sample E3 58
39 Sample N1 61
40 Trend of mircodamage for every testing sets 62
41 Trend of mircodamage 3D 63
42 Damage density - 3D, dependent on number of cycles tested 66
43 Damage density - 2D dependent on number of cycles tested 68
44 Original vs. colour-corrected image 70
45 Issue with Alizarin Red S 71
46 Definition of region of interest for linear crack and diffuse damage in ImageJ for image analysis 86
47 Elastic modulus sample B2 87
48 Elastic modulus sample B7 87
49 Elastic modulus sample D1 88
50 Elastic modulus sample E3 88
51 Elastic modulus sample F3 88
52 Elastic modulus sample G1 89
53 Elastic modulus sample G7 89
54 Elastic modulus sample I1 89
55 Stress and strain amplitude sample B2 90
56 Stress and strain amplitude sample B7 90
57 Stress and strain amplitude sample D1 90
58 Stress and strain amplitude sample E3 91
59 Stress and strain amplitude sample F3 91

60 Stress and strain amplitude sample G1 91
61 Stress and strain amplitude sample G7 92
62 Stress and strain amplitude sample I1 92
63 Stress-Strain-Data for sample B2 93
64 Stress-Strain-Data for sample B7 93
65 Stress-Strain-Data for sample D1 93
66 Stress-Strain-Data for sample E3 94
67 Stress-Strain-Data for sample F3 94
68 Stress-Strain-Data for sample G1 94
69 Stress-Strain-Data for sample G7 95
70 Stress-Strain-Data for sample I1 95
71 Reference samples N1 N2, N3, N4 with 20x magnification 96
72 Samples F2, S1, S2 with 20x magnification 96
73 Samples S3, 8a, 8b with 20x magnification 96
74 Samples J2, J4 and H3 with 20x magnification 97
75 Sample G7 with 20x magnification, Sample F1 and G6 with 10x magnification 97
76 Sample D1 and G1 with 20x magnification, Sample E3 with 10x magnification 97
77 Sample G2, G8 and I1 with 20x magnification 98
78 Sample J3 with 20x magnification 98
79 Max. Intensity Projection for Sample D1, E1, G1 99
80 Max. Intensity Projection for Sample G2, G8, H3 99
81 Max. Intensity Projection for Sample I1, J2, J3 99
82 Max. Intensity Projection for Sample J4, S1, S2 100
83 Template for sample holder 104

List of Tables

1 Comparison of measuring methods of sample geometry 26
2 SEL mini-001 specifications [75] 35
3 Test specifications 38
4 New control engineering settings 38
5 Leica Ultramilling settings 42
6 CLSM Settings 46
7 Parameters for 3-dimensional analysis 51
8 Parameters for 2-dimensional analysis 51
9 Elastic modulus 57
10 Means of stress and strain amplitudes 59
11 Final test parameters 60
12 Damage determination of individual trabeculae - 3D 65
13 Damage determination of individual trabeculae - 2D 67
14 Protocol: Test specifications 81
15 Protocol: Final test parameters 81
16 Protocol: Leica Ultramilling settings 82
17 Protocol: CLSM settings 83
18 Protocol: Parameters for 3-dimensional analysis 84
19 Protocol: Parameters for 2-dimensional analysis 85
20 p-values as indicator of significance between different testing sets 101
21 p-values as indicator of significance between different testing sets 102
22 Comparison of different variables 102
23 Comparison between 2D and 3D data 103

References

[1] Charlotte Wirl Petra Winkler, Elisabeth Pochobradsky. Endreport: Gesundheit und krankheit der alteren generation in osterreich. Im Auftrag des Bundesministeriums für Gesundheit, 2012. `https://goeg.at/sites/default/files/2017-06/seniorenbericht_2012.pdf`.

[2] Who scientific group on the assessment od osteoporosis at primary health care level. Summary Meeting Report, 2004.

[3] Green J. et all. Age-related changes in human trabecular bone: Relationship between microstructural stress and strain and damage morphology. *Journal of Biomechanics*, 44:2279–2285, 2011.

[4] Stefan van der Geest Michael Pazianas and Paul Miller. Bisphosphonates and bone quality. *BoneKEy Reports*, 3, may 2014.

[5] Zysset et al. Elastic modulus and hardness of cortical and trabecular bone lamellae measured by nanoindentation in the human femur. *Journal of Biomechanics*, 32(10):1005–1012, oct 1999.

[6] Seref-Ferlengez et al. Bone microdamage, remodeling and bone fragility: how much damage is too much damage? *BoneKEy Reports*, 4, 2015.

[7] Tamim Diab et al. Age-related change in the damage morphology of human cortical bone and its role in bone fragility. *Bone*, 38(3):427–431, mar 2006.

[8] Milgrom C. Schaffler MB, Choi K. Aging and matrix microdamage accumulation in human compact bone. *Bone*, 17:521–525, 1995.

[9] David B Burr. Repair mechanisms for microdamage in bone. *Journal of Bone and Mineral Research*, 29(12):2534–2536, dec 2014.

[10] Amy H. Warriner, Nivedita M. Patkar, Jeffrey R. Curtis, Elizabeth Delzell, Lisa Gary, Meredith Kilgore, and Ken Saag. Which fractures are most attributable to osteoporosis? *Journal of Clinical Epidemiology*, 64(1):46–53, jan 2011.

[11] O. Johnell and J. A. Kanis. An estimate of the worldwide prevalence and disability associated with osteoporotic fractures. *Osteoporosis International*, 17(12):1726–1733, sep 2006.

[12] M.G. Goff, F.M. Lambers, T.M. Nguyen, J. Sung, C.M. Rimnac, and C.J. Hernandez. Fatigue-induced microdamage in cancellous bone occurs distant from resorption cavities and trabecular surfaces. *Bone*, 79:8–14, oct 2015.

[13] T. L. A. Moore, F. J. O'Brien, and L. J. Gibson. Creep does not contribute to fatigue in bovine trabecular bone. *Journal of Biomechanical Engineering*, 126(3):321, 2004.

[14] Erik I. Waldorff, Steven A. Goldstein, and Barbara R. McCreadie. Age-dependent microdamage removal following mechanically induced microdamage in trabecular bone in vivo. *Bone*, 40(2):425–432, feb 2007.

[15] D VASHISHTH. In vivo diffuse damage in human vertebral trabecular bone. *Bone*, 26:147–152, 2000.

[16] B. Clarke. Normal bone anatomy and physiology. *Clinical Journal of the American Society of Nephrology*, 3:131–S139, nov 2008.

[17] Nanocomposites, 2018-01-04. `https://www.nature.com/subjects/nanocomposites`.

[18] Adele L Boskey. Bone composition: relationship to bone fragility and antiosteoporotic drug effects. *BoneKEy Reports*, 2, dec 2013.

[19] D. J. Hadjidakis and I. I. Androulakis. Bone remodeling. *Annals of the New York Academy of Sciences*, 1092(1):385–396, dec 2006.

[20] Satoshi Yamada. Mechanical properties and hierarchical structure of bone research contributing to the prevention and treatment of osteoporosis. `http://labs.eng.hokudai.ac.jp/office/elo/en/archives/labo/1540/`.

[21] M. Mostakhdemin et al. *Multi-axial Fatigue of Trabecular Bone with Respect to Normal Walking*. Springer, 2016.

[22] *Anatomy and Physiology*, volume Chapter 6. Bone Tissue and the Skeletal System. Open Textbooks Adapted and Created by BC Faculty.

[23] G. Danuser E. Luccinetti, D. Thomann. Review micromechanical testing of bone trabeculae - potentials and limitations. *JOURNAL OF MATERIALS SCIENCE*, 35:6057 – 6064, 2000.

[24] Xiaohan Lai; Christopher Price; Liyun Wang. Osteocyte lacunae and canaliculi in cortical and trabecular bones. ORS 2012Annual Meeting, 2012.

[25] Philipp Thurner. Lecture: Introduction to biomechanics, lecture6: Musculoskeletal anatomy, 2015.

[26] Julius Wolff. *Das Gesetz der Transformation der Knochen*. Hirschwald, 1892.

[27] Ramin Oftadeh, Miguel Perez-Viloria, Juan C. Villa-Camacho, Ashkan Vaziri, and Ara Nazarian. Biomechanics and mechanobiology of trabecular bone: A review. *Journal of Biomechanical Engineering*, 137(1):010802, dec 2014.

[28] D. Taylor, J. G. Hazenberg, and T. C. Lee. Living with cracks: Damage and repair in human bone. *Nature Materials*, 6(4):263–268, apr 2007.

[29] K. Choi and S.A. Goldstein. A comparison of the fatigue behavior of human trabecular and cortical bone tissue. *Journal of Biomechanics*, 25(12):1371–1381, dec 1992.

[30] Hadji P; Klein S; Gothe H; Häussler B; Kless T; Schmidt T; Steinle T; Verheyen F; Linder R. The epidemiology of osteoporosis. *Dtsch Arztebl*, 110(4):52–7, 2013.

[31] Fyhrie DP Wenzel TE, Schaffler MB. In vivo trabecular microcracks in human vertebral bone. *Bone*, 19:89–95, 1996.

[32] N.L. Fazzalari, M.R. Forwood, K. Smith, B.A. Manthey, and P. Herreen. Assessment of cancellous bone quality in severe osteoarthrosis: Bone mineral density, mechanics, and microdamage. *Bone*, 22(4):381–388, apr 1998.

[33] N.L. Fazzalari, M.R. Forwood, B.A. Manthey, K. Smith, and P. Kolesik. Three-dimensional confocal images of microdamage in cancellous bone. *Bone*, 23(4):373–378, oct 1998.

[34] E. M. Aarden, P. J. Nijweide, and E. H. Burger. Function of osteocytes in bone. *Journal of Cellular Biochemistry*, 55(3):287–299, jul 1994.

[35] The Editors of Encyclopædia Britannica. Osteoclasts, 2018-01-09. `https://www.britannica.com/science/osteoclast`.

[36] The Editors of Encyclopædia Britannica. Osteoblast, 2018-01-09. `https://www.britannica.com/science/osteoblast`.

[37] J. Klein-Nulend, R.G. Bacabac, and M.G. Mullender. Mechanobiology of bone tissue. *Pathologie Biologie*, 53(10):576–580, dec 2005.

[38] S.A. Colopy, J. Benz-Dean, J.G. Barrett, S.J. Sample, Y. Lu, N.A. Danova, V.L. Kalscheur, R. Vanderby, M.D. Markel, and P. Muir. Response of the osteocyte syncytium adjacent to and distant from linear microcracks during adaptation to cyclic fatigue loading. *Bone*, 35(4):881–891, oct 2004.

[39] Tasuku Mashiba, Toru Hirano, Charles H. Turner, Mark R. Forwood, C. Conrad Johnston, and David B. Burr. Suppressed bone turnover by bisphosphonates increases microdamage accumulation and reduces some biomechanical properties in dog rib. *Journal of Bone and Mineral Research*, 15(4):613–620, feb 2010.

[40] Matthew R. Allen, Ken Iwata, Roger Phipps, and David B. Burr. Alterations in canine vertebral bone turnover, microdamage accumulation, and biomechanical properties following 1-year treatment with clinical treatment doses of risedronate or alendronate. *Bone*, 39(4):872–879, oct 2006.

[41] Jan J. Stepan, David B. Burr, Imre Pavo, Adrien Sipos, Dana Michalska, Jiliang Li, Astrid Fahrleitner-Pammer, Helmut Petto, Michael Westmore, David Michalsky, Masahiko Sato, and Harald Dobnig. Low bone mineral density is associated with bone microdamage accumulation in postmenopausal women with osteoporosis. *Bone*, 41(3):378–385, sep 2007.

[42] B.C. Herman, L. Cardoso, R.J. Majeska, K.J. Jepsen, and M.B Schaffler. Activation of bone remodeling after fatigue: Differential response to linear microcracks and diffuse damage. *Bone*, 47(4):766–772, oct 2010.

[43] Orestis L. Katsamenis, Thomas Jenkins, and Philipp J. Thurner. Toughness and damage susceptibility in human cortical bone is proportional to mechanical inhomogeneity at the osteonal-level. *Bone*, 76:158–168, jul 2015.

[44] Georg E. Fantner, Tue Hassenkam, Johannes H. Kindt, James C. Weaver, Henrik Birkedal, Leonid Pechenik, Jacqueline A. Cutroni, Geraldo A. G. Cidade, Galen D. Stucky, Daniel E. Morse, and Paul K. Hansma. Sacrificial bonds and hidden length dissipate energy as mineralized fibrils separate during bone fracture. *Nature Materials*, 4(8):612–616, jul 2005.

[45] Stacyann Morgan, Atharva A. Poundarik, and Deepak Vashishth. Do non-collagenous proteins affect skeletal mechanical properties? *Calcified Tissue International*, 97(3):281–291, jun 2015.

[46] A. A. Poundarik, T. Diab, G. E. Sroga, A. Ural, A. L. Boskey, C. M. Gundberg, and D. Vashishth. Dilatational band formation in bone. *Proceedings of the National Academy of Sciences*, 109(47):19178–19183, nov 2012.

[47] M.D. Grynpas, J.H. Tupy, and J. Sodek. The distribution of soluble, mineral-bound, and matrix-bound proteins in osteoporotic and normal bones. *Bone*, 15(5):505–513, sep 1994.

[48] Julie M Hughes, Kristin L Popp, Ran Yanovich, Mary L Bouxsein, and Ronald W Matheny. The role of adaptive bone formation in the etiology of stress fracture. *Experimental Biology and Medicine*, 242(9):897–906, aug 2016.

[49] David B. Burr, Mark R. Forwood, David P. Fyhrie, R. Bruce Martin, Mitchell B. Schaffler, and Charles H. Turner. Bone microdamage and skeletal fragility in osteoporotic and stress fractures. *Journal of Bone and Mineral Research*, 12(1):6–15, jan 1997.

[50] Lee O'Brien, Taylor. Microcrack accumulation at different intervals during fatigue testing of compact bon. *Journal of Biomechanics*, 36(7):973–980, 2003.

[51] Martin Frank, Dorothee Marx, Dieter H. Pahr, and Philipp J. Thurner. Mechanical properties of individual trabeculae in a physiological environment. In *Biomedical Engineering*. ACTAPRESS, 2017.

[52] Robert A. Draughn Yuehuei H. An. *Mechanical Testing of Bone and the Bone-Implant Interface*. CRC Press, 1999.

[53] Bo Wu, Chan Zhang, Bo Chen, Ling Zhang, Ruchun Dai, Xianping Wu, Yebin Jiang, and Eryuan Liao. Self-repair of rat cortical bone microdamage after fatigue loading in vivo. *International Journal of Endocrinology*, 2013:1–8, 2013.

[54] S. M. Bowman, X. E. Guo, D. W. Cheng, T. M. Keaveny, L. J. Gibson, W. C. Hayes, and T. A. McMahon. Creep contributes to the fatigue behavior of bovine trabecular bone. *Journal of Biomechanical Engineering*, 120(5):647, 1998.

[55] Lisbeth Roehl, Ejnar Larsen, Frank Linde, Anders Odgaard, and Jørgen Jørgensen. Tensile and compressive properties of cancellous bone. *Journal of Biomechanics*, 24(12):1143–1149, jan 1991.

[56] R.B. Ashman, J.Y. Rho, and C.H. Turner. Anatomical variation of orthotropic elastic moduli of the proximal human tibia. *Journal of Biomechanics*, 22(8-9):895–900, jan 1989.

[57] Wu et al. In vivo microdamage is an indicator of susceptibility to initiation and propagation of microdamage in human femoral trabecular bone. *Bone*, 55(1):208–215, jul 2013.

[58] T. C. Lee, S. Mohsin, D. Taylor, R. Parkesh, T. Gunnlaugsson, F. J. OBrien, M. Giehl, and W. Gowin. Detecting microdamage in bone. *Journal of Anatomy*, 203(2):161–172, aug 2003.

[59] T. C. Lee, T. L. Arthur, L. J. Gibson, and W. C. Hayes. Sequential labelling of microdamage in bone using chelating agents. *Journal of Orthopaedic Research*, 18(2):322–325, mar 2000.

[60] Fergal J O'Brien, David Taylor, and T.Clive Lee. An improved labelling technique for monitoring microcrack growth in compact bone. *Journal of Biomechanics*, 35(4):523–526, apr 2002.

[61] Stephen W. Paddock. Principles and practices of laser scanning confocal microscopy. *Molecular Biotechnology*, 16(2):127–150, 2000.

[62] MF Dental. Product information mf dental, 2018-04-05. `http://www.mf-dental.de/de/Rotierende-Instrumente/Diamantbohrer/Zylinder-spitz/Diamantbohrer-FG-5-St-Zylinder-spitz-885-010.html?listtype=search&searchparam=885010`.

[63] *Verarbeitungsanleitung picodent twinsil® 22 Additionsvernetzendes Dublier-silikon*, 2018-01-02. `https://www.picodent.de/cms/upload/download/twinsil-verarbeitungsanleitung.pdf`.

[64] UHU GmbH and Co KG. Datenblatt uhu endfest, 2018-02-03. `http://www.uhu-profi.de/uploads/tx_ihtdownloads/UHU_moderne_mat_neu.pdf`.

[65] Sigma-Aldrich. Alizarin rot s sicherheitsdatenblatt, 2018-04-09. `https://www.sigmaaldrich.com/MSDS/MSDS/DisplayMSDSPage.do?country=AT&language=de&productNumber=A5533&brand=SIAL&PageToGoToURL=https%3A%2F%2Fwww.sigmaaldrich.com%2Fcatalog%2Fproduct%2Fsial%2Fa5533%3Flang%3Dde`.

[66] Sigma-Aldrich. Calceine blue product specification, 2018-05-05. `https://www.sigmaaldrich.com/Graphics/COfAInfo/SigmaSAPQM/SPEC/M1/M1255/M1255-BULK_____SIGMA____.pdf`.

[67] Sigma-Aldrich. Xylenol orange sicherheitsdatenblatt, 2018-02-02. `https://www.sigmaaldrich.com/MSDS/MSDS/DisplayMSDSPage.do?country=AT&language=de&productNumber=52097&brand=SIAL&PageToGoToURL=https%3A%2F%2Fwww.sigmaaldrich.com%2Fcatalog%2Fproduct%2Fsial%2F52097%3Flang%3Dde`.

[68] Sigma-Aldrich. Calcein product specification, 2018-05-05. https://www.sigmaaldrich.com/Graphics/COfAInfo/SigmaSAPQM/SPEC/C0/C0875/C0875-BULK_____SIGMA____.pdf.

[69] Jennifer L. W. Carter, Michael D. Uchic, and Michael J. Mills. Impact of speckle pattern parameters on DIC strain resolution calculated from in-situ SEM experiments. In *Fracture, Fatigue, Failure, and Damage Evolution, Volume 5*, pages 119–126. Springer International Publishing, jul 2014.

[70] Technisches merkblatt, 2018-05-18. https://www.motipdupli.com/de/INT/produkte/dupli-color/dekoration/color/ipg-1268/tm-1268.html.

[71] Eg-sicherheitsblatt, 2017-08-09. http://www.crcind.com/csp/web/msds.csp?document=BDS000774_4_T_&idx=356.

[72] Platinum sprühkopf-set, 2018-02-02. https://www.motipdupli.com/de/produkte/dupli-color/dekoration/color/platinum/ipg-1087.html.

[73] Dorothee Marx. Entwicklung eines zugversuchs für die mikromechanische charakterisierung von knochen. Master's thesis, Technische Universität Wien, 2015.

[74] P.J. Thurner, B. Erickson, R. Jungmann, Z. Schriock, J.C. Weaver, G.E. Fantner, G. Schitter, D.E. Morse, and P.K. Hansma. High-speed photography of compressed human trabecular bone correlates whitening to microscopic damage. *Engineering Fracture Mechanics*, 74(12):1928–1941, August 2007.

[75] Thelkin AG. Betriebsanleitung servoelektischer lastrahmen, 2013.

[76] *Bedinungsanleitung Leica SP2600*, 2018-03-03. https://drp8p5tqcb2p5.cloudfront.net/fileadmin/downloads_lbs/Leica%20SP2600%20Ultramiller/User%20Manuals/Leica_SP2600_Manual_DE.pdf.

[77] Imagej informtion site:, 2018-02-02. https://imagej.net/ImageJ.

[78] D. B. Allan. trackpy v.0.3.2, 2016.

[79] Thierry Savin and Patrick S. Doyle. Static and dynamic errors in particle tracking microrheology. *Biophysical Journal*, 88(1):623–638, jan 2005.

[80] D. R. H. Jones and Michael F. Ashby. *Engineering Materials 1: An Introduction to Properties, Applications and Design: v. 1.* Butterworth-Heinemann, 2005.

[81] A. Synek, Y. Chevalier, S.F. Baumbach, and D.H. Pahr. The influence of bone density and anisotropy in finite element models of distal radius fracture osteosynthesis: Evaluations and comparison to experiments. *Journal of Biomechanics*, 48(15):4116–4123, nov 2015.

[82] G W Zack, W E Rogers, and S A Latt. Automatic measurement of sister chromatid exchange frequency. *Journal of Histochemistry & Cytochemistry*, 25(7):741–753, jul 1977.

[83] David Taylor and T. Clive Lee. Measuring the shape and size of microcracks in bone. *Journal of Biomechanics*, 31(12):1177–1180, dec 1998.

[84] Mori et al. Trabecular bone volume and microdamage accumulation inthe femoral heads of women with and without femoral neck fractures. *Bone*, 21(6):521–6, 1997.

[85] T. C. LEE, E. R. MYERS, and W. C. HAYES. Fluorescence-aided detection of microdamage in compact bone. *Journal of Anatomy*, 193(2):179–184, aug 1998.